Mitigating high-temperature, high-pressure hydrogen attack

Mohammed Abdulrahman Alshahrani

Hughes Hall

University of Cambridge

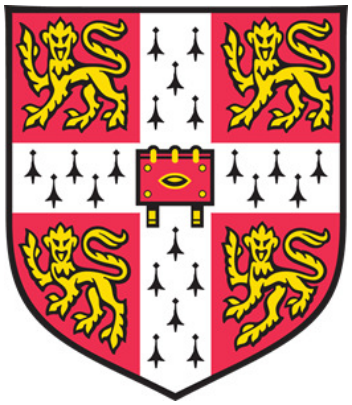

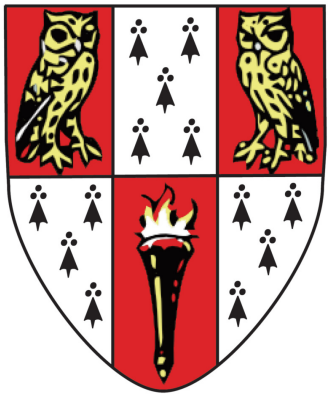

Department of Materials Science and Metallurgy

A dissertation submitted for the degree of

Doctor in Philosophy

September 2021

Abstract

High-temperature, high-pressure hydrogen attack is a degradation mechanism that threatens the integrity of critical components in refineries and petrochemical plants. This phenomenon was discovered in the early twentieth century, however, the experience-based recommended practice used to design for such applications is still being corrected due to ongoing failures in industry. Research on the topic, in the late twentieth century, focused on experimenting with hydrogen attack. Since then, most of the work has been focused on the modelling aspect of the issue.

The aim of the work presented in this thesis was to understand the mechanism of hydrogen attack, using experimental methods, in order to reach a mitigation solution that utilises current literature and improves upon the recommended practice.

Hydrogen attack resistance was examined in the commercially-used steel, $2\frac{1}{4}$Cr-1Mo, revealing the importance of heat treatment conditions to bring the precipitated carbides closer to their equilibrium state, which decreases carbon activity in the steel and consequently increases the resistance to reaction with hydrogen. For the first time, experimental methods, such as quantification of carbide volume fractions using synchrotron X-ray diffraction as well as optical microscopy to measure void volume-fractions, were used in characterising hydrogen-attack resistence. Consistent interpretations of experimental data have been obtained by comparison against equilibrium calculations, microstructure and synchrotron X-ray diffraction.

Some novel approaches were also adopted for the first time. Interphase precipitation in vanadium steel was shown in this work as a solution to mitigate hydrogen attack at the same exposure conditions where some samples of $2\frac{1}{4}$Cr-1Mo steel

failed. The mitigation was explained by the direct precipitation of stable vanadium carbides during the austenite to ferrite transformation, which immediately depletes ferrite of carbon, thus reducing the carbon activity. This is not the case in tempered martensite that contains many lattice defects, where excess carbon may be retained, hence increasing carbon availability for methane formation. Vanadium carbides are found to be more stable than chromium or molybdenum carbides in the alloy systems considered.

The hydrogen attack mechanism leads to bubble formation with these bubbles progressively linking by a creep mechanism, until ultimate failure. Vanadium is generally known to particularly enhance the creep strength, so any voids created would have a difficulty in linking up by creep deformation in the presence of carbides.

Another novel approach was to use the recently invented HT10 steel, that has been shown to outperform $2\frac{1}{4}$Cr-1Mo steel in terms of ambient mechanical properties and low-temperature hydrogen embrittlement. The work in this thesis has shown, for the first time, that HT10 outperforms $2\frac{1}{4}$Cr-1Mo in terms of elevated-temperature hydrogen attack caused by methane formation. Given that HT10 is similar in many aspects to the commercially-used steel in hydrogen-attack applications ($2\frac{1}{4}$Cr-1Mo), HT10 steel can offer a suitable replacement more easily than the vanadium steel studied that still requires further investigations in terms of mechanical properties.

The thesis finishes with the definition of an interesting programme of future work that not only can reveal fundamental knowledge never before attempted, but also may lead to technological exploitation.

Declaration

I hereby declare that all of the enclosed work is the result of my own work and includes nothing which is the outcome of work done in collaboration except as specified in the text. I declare that I have not submitted this thesis, or any part thereof, for any degree, diploma or any other qualification at any other institution.

I declare that this thesis does not exceed the prescribed limit of 60,000 words.

Mohammed Alshahrani

Cambridge, U.K., September 2021

Acknowledgements

I would like to heartily thank my mother, Hanan, and my father, Abdulrahman, for their endless encouragement, ultimate belief in me and all the sacrifices over the years, those that I know and the many I do not know of.
All that I am, I owe to you.
All my successes are attributed to the rational and moral eduction I received from you.
I am forever in your debt.
My love and thanks are extended to my sisters, Bashayer and Esraa, and my brothers, Yazeed and Abdulmajeed. Through the tough times in this project, especially with the pandemic, our calls have always been warm, refreshing and motivating. The strength I receive from my family's love will always be the blessing I am most thankful for.

I express my gratitude and appreciation to Sir Harshad Kumar Dharamshi Hansraj Bhadeshia for all his advice, patience and time. I was always learning in every discussion we had. The knowledge I gained was not only technical, but also on how to critically think of an issue in order to find the answer. I am very lucky to have had the chance to learn from your experience. Sincere thanks also to Dr. Steve Ooi for his tireless help from the first steps in this project until the last.

I must give a special mention to those who helped making this project much easier, Dr. Giorgio Divitini for his continuous help with transmission electron microscopy, Mr. Simon Griggs for his assistance with scanning electron microscopy and his cheerful spirit, Mrs. Sue Gymer for her endless help in the process lab, Gebril El-Fallah, Shaumik Lenka, Nikolaos Panagiotopoulos, Dominik Dziedzic, Shengda Pu and Adriel

Wong for their assistance and for making the laboratory a great place to work. Sincere gratitude to my sponsor who has funded this project, the Saudi Arabian Oil Company (Saudi Aramco).

The journey of a Ph.D. is known to be a roller-coaster full of stressful times, add to that a “pandemic-edition”. They could have been such dreadful times, but to me they were as delightful as they can get because of a great group of friends; Khalid Egal, Ahmed Khan, Saeed Aljabri and Ali Alsulami. I am very grateful to have been accompanied in this journey by such high-quality individuals, with the kindest hearts. Each gathering just had it all, the inspiration, the humour and the support. This journey was made far more special because of your friendship so thank you.

Finally, I would like to thank this fate for offering me this chapter that included working with great minds in a great environment, surrounded by great friends. This chapter was much more than just a scientific project. I will always remember the lessons I was taught here; never to lose curiosity, to be always aware, to appreciate but never to settle for the present.

Contents

Introduction

There are many components in the petrochemical industries that come into contact with gaseous hydrogen at high pressures and temperatures. This is where the problem of a particular mechanism of hydrogen attack in steel becomes important because the consequences of failure can cause large-scale disasters, for example, the fatal catastrophe at the Tesoro Anacortes Refinery [1]. More commonly, the attack results in the costly replacement of components.

High-temperature high-pressure hydrogen attack is a degradation phenomenon where atomic hydrogen diffuses into the steel, accumulating at defects and reacting with the carbon present, mostly, in the carbides leading to the formation of methane-gas bubbles. Bubble nucleation and growth leads to pressure build-up within the steel structure that consequently initiates fissures and cracks [2–5]. Therefore, one can argue that the presence of stable carbides that do not allow the reaction with hydrogen is a necessity in resisting such attack. That stability can be influenced by factors such as the steel composition and the heat treatment that precipitates those carbides.

The current best practice for designing against hydrogen attack uses an experience-based approach, expressed as the *Nelson curves*, in the American Petroleum Institute Recommended Practice 941 (API RP 941), Figure 1 [6]. These curves define the temperature and hydrogen pressure at which established steels can operate without the risk of hydrogen attack. However, these curves have been modified due to problems arising in industry, suggesting that there is a room for improvement in order to ensure safe operating-conditions. Although, heat treatments could

play a major role in precipitating specific carbides that resist hydrogen attack, they are not specified in the best practice. Therefore, it is possible that specific factors have been overlooked, creating room for error that could lead to a dangerous or premature failure mechanism of hydrogen attack.

A literature review on the hydrogen attack mechanism along with a description of possible mitigation methods is first presented in Chapter 1. The experimental methodology used in this project is described in Chapter 2. An examination of a currently-used steel in hydrogen attack applications, $2\frac{1}{4}$Cr-1Mo, is documented in Chapter 3. Chapter 4 reports the results of examining the proposed mitigation methods. Final conclusions along with suggestions for future work are presented in Chapter 5.

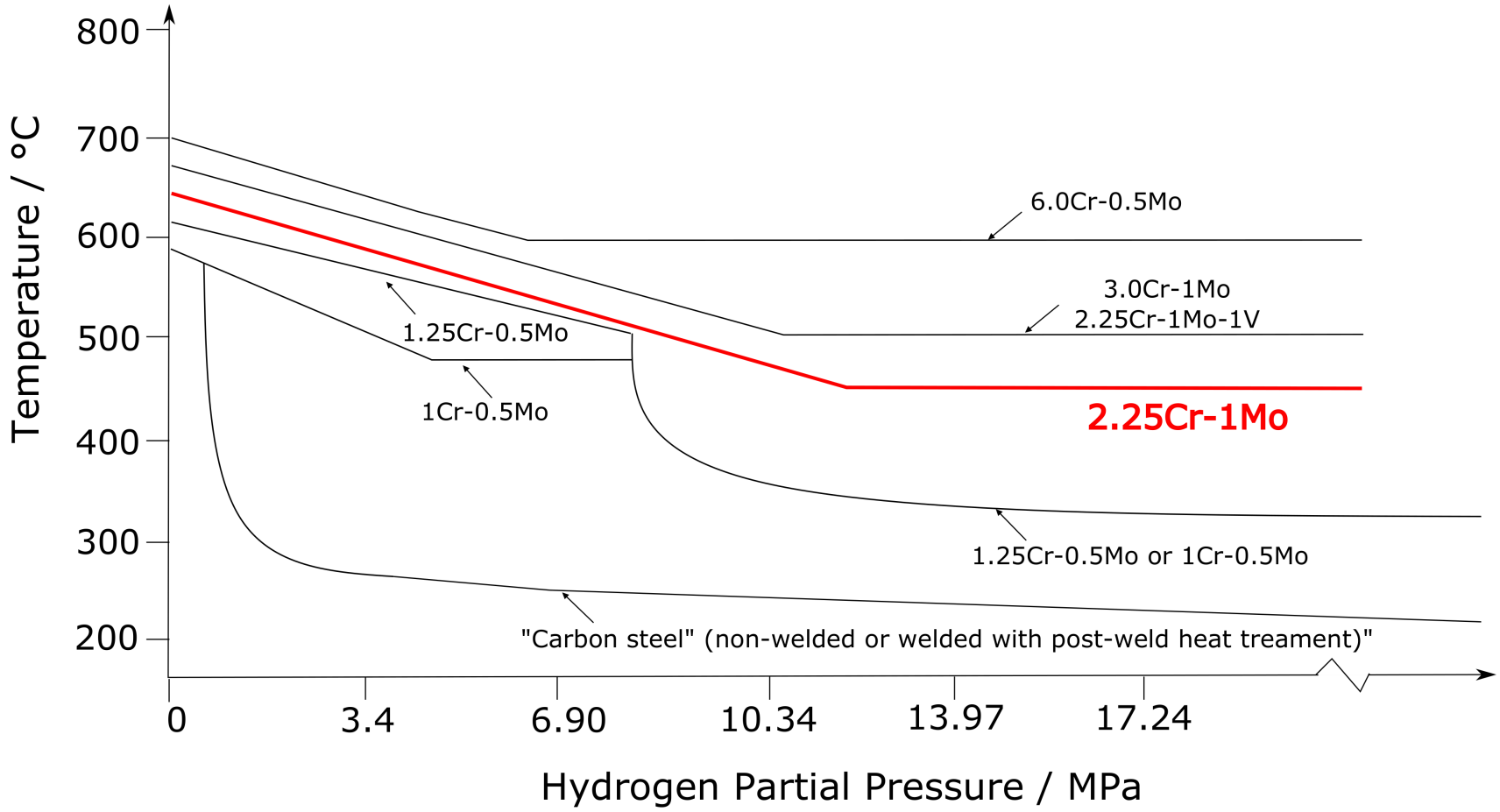

Figure 1: Nelson curves show the temperature and hydrogen pressure in which a specific steel can in principle perform safely, i.e., without significant hydrogen attack. The area below each curve represents the safe operating zone for the corresponding steel. In red is one of the steels used in this work. Adapted from [6].

Chapter 1

Literature review

1.1 Introduction

The aim of the work presented in this chapter was to explore the current literature on hydrogen attack mechanism and how it can be influenced. This research was aimed at identifying factors or techniques in which hydrogen attack can be mitigated, whether that means designing a new steel or utilising an existing mechanism to enhance the attack resistance of current commercial alloys. This literature review consists of two sections:

- the first explores the current knowledge on hydrogen attack, factors influencing the mechanism and some case studies of commercially-used steels. This knowledge is used to guide any mitigation phenomena discussed next.

- The second section elaborates on a possible mitigation method involving steel containing 'interphase precipitation'. Such steels have not been assessed with respect to hydrogen attack.

1.2 Elevated temperature hydrogen attack

Gaseous hydrogen at pressures in excess of about 0.7 MPa and at temperatures exceeding 200°C can attack steel in a manner that dramatically degrades its mechanical properties. The molecular hydrogen then tends to dissociate, with the resulting atoms diffusing into the steel. Apart from accumulating at defects such as inclusions and interfaces in general, the nascent hydrogen reacts chemically with the carbon that is tied up in carbides, to form methane bubbles which become a permanent feature of the steel as they are too large to diffuse out, as seen in the following reaction: $C + 2H_2 \leftrightarrow CH_4$. The methane reaction occurs preferentially at the least stable carbide, which in most cases is cementite, as follows: $Fe_3C + 2H_2 \leftrightarrow CH_4 + 3Fe$. The reaction can still take place to a lesser extent at other substitutionally-alloyed carbides that are typical in creep-resisting steels, for example, M_7C_3, M_2C, $M_{23}C_6$ etc., where 'M' stands for a mixture of metal atoms. [7–12].

The bubbles develop into cavities as the methane accumulates at grain boundaries; the resulting pressure within weakens grain boundaries and can lead eventually to the formation of microcracks and ultimate failure under the influence of the external stresses that the component is designed to support or even by the local creep introduced by the bubble formation [4, 9]. Therefore, hydrogen attack of the type described here is not the same as hydrogen embrittlement (HE) where the *toughness* of the steel is affected by diffusible, nascent hydrogen. HE has been studied for more than a century, leading to the proposal of many mechanisms [13] but the first proposed, still valid, mechanism suggests that atomic hydrogen, i.e. the embrittling agent in HE, is attracted to appropriate stress fields, where it accumulates and alters the fracture mechanism by blocking dislocation emission, thereby introducing hydrogen embrittlement [14–16]. However, in hydrogen attack, carbon depletion to form methane gas has been proven to be the embrittling step in this methane-based mechanism by the work of Weiner [17], in which he compared the behaviour of iron alloys and steels in a variaty of hydrogen attack environments, compositions of iron alloy F-1 and the commercial steel can be found in Table 1.1. The deterioration was

less in the iron alloys than in the steel due to the much smaller carbon content in the iron alloys. Thygson further supported that hypothesis by examining the possibility of reversing hydrogen attack. He concluded that methane is the embrittling agent, not molecular hydrogen, as the change in the volume did not decrease or reverse as the specimens were heated up to 400°C [18], which indicates the permanent damage caused by methane formation at the expense of carbon content as illustrated in Figure 1.1. If hydrogen was responsible for the damage, then the volume change would have decreased upon heating because the hydrogen diffuses out of the steel. Carbon exerts a strengthening influence on the steel, therefore, its depletion threatens the structural integrity of the steel.

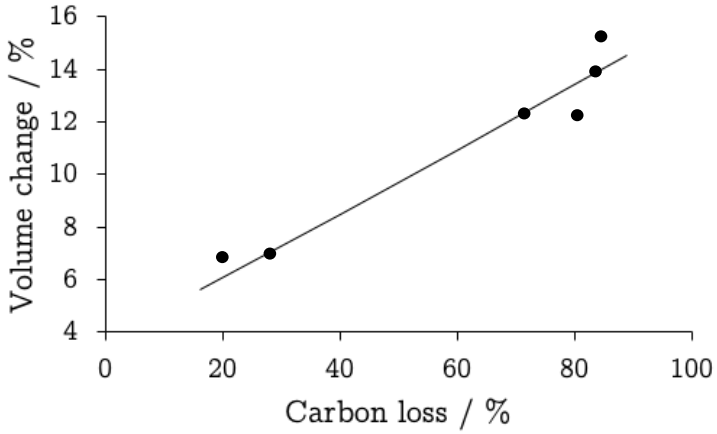

Figure 1.1: Irreversible damage as carbon loss increases in proportion to the volume change in C-1095 steel, composition in Table 1.1. The maximum volume change is quite large ≈ 15%, which could be due to the wire-shaped specimens with 1.5 mm diameter, which consequently represent the entire reaction zone. Adapted from [18] with permission American Chemical Society, copyright 1964.

Table 1.1: Chemical compositions (wt%) of all steels referenced in the literature review.

Material	C	Si	Mn	P	S	Cu	Ni	Cr	Mo	Nb	Al	Co	Ti	V	W	B	N	Sn	As	Reference
Iron alloy F-1	0.0042	–	–	–	–	–	–	–	–	–	–	–	–	–	–	–	–	–	–	[17]
Commercial steel	0.19	0.19	0.7	0.015	0.015	–	–	–	–	–	0.017	–	–	–	–	–	–	–	–	[17]
C-1095	0.95	–	0.4	0.04	0.05	–	–	–	–	–	–	–	–	–	–	–	–	–	–	[18]
Pipe steel	0.3	–	1.2	0.05	0.06	0.4	0.4	0.4	0.15	–	–	–	–	0.08	–	–	–	–	–	[19]
Carbon steel	0.22	0.25	1.22	0.005	0.004	0.14	0.13	0.11	0.041	0.002	0.053	–	0.002	–	–	–	–	0.025	–	[20]
A516	0.29	0.21	1.04	0.14	0.003	0.24	0.18	0.13	0.05	–	0.057	–	–	0.002	–	–	–	–	–	[21]
SAE 1020	0.19	0.25	0.58	0.014	–	0.08	–	0.02	0.02	–	–	0.009	–	–	–	–	–	0.008	–	[3]
$2\frac{1}{4}$Cr-1Mo (1)	0.13	0.23	0.52	0.01	0.01	–	0.18	2.23	0.95	–	0.021	–	–	–	–	–	–	–	–	[22]
A542 C13	0.13	0.25	0.51	0.006	0.008	0.13	–	2.32	0.98	–	0.019	–	–	–	–	–	0.012	–	0.031	[23]
$2\frac{1}{4}$Cr-1Mo (2)	0.12	0.12	0.58	0.008	0.005	0.01	0.03	2.36	0.98	–	0.014	–	–	0.006	–	–	–	–	–	[24]
9%Cr + boron	0.078	0.30	0.51	–	–	–	–	8.99	–	0.05	–	3.01	–	0.19	2.91	0.0139	0.003	–	–	[25]
9%Cr	0.078	0.31	0.50	–	–	–	–	8.94	–	0.05	–	3.03	–	0.19	2.94	<0.0001	0.002	–	–	[25]
SA542, C13	0.12	0.022	0.47	0.01	0.017	0.12	0.22	2.26	0.99	–	–	–	–	–	–	–	–	–	–	[26]
$\frac{1}{2}$Cr-Mo-V	0.10	0.25	0.59	0.015	0.029	0.12	0.11	0.32	0.51	–	–	–	–	0.24	–	–	–	–	–	[27]
Ti-Mo	0.06	0.1	1.5	–	–	–	–	–	0.004	–	–	–	0.2	–	–	–	0.002	–	–	[28]
9Cr-1.5Mo	0.12	–	0.4	–	–	–	–	9	1.5	0.05	–	1.2	–	0.2	–	0.008-0.011	0.015-0.03	–	–	[29]

1.2.1 Mechanism

The attack mechanism can be broken down into two stages:

- **The initial incubation period** of the attack is the tendency for the hydrogen gas to dissociate, penetrate the steel and begin to react with carbides to form methane bubbles at grain boundaries and cavities, which results in an external volume change, but this kind of damage is difficult to detect as it does not noticeably affect the mechanical properties [7, 9]. This incubation stage consists of two equilibrium reactions; carbide dissolution and the formation of methane gas. The former reaction supplies carbon atoms to the latter. The supply of carbon will continue in order to maintain the equilibrium methane pressure, leading eventually to the decarburisation of the steel [30, 31], as can be seen in the example illustrated in Figure 1.2. Once decarburisation starts, then the driving force for the attack becomes the concentration gradient between the carbon reservoirs in the carbides and the cavities or boundaries, where some methane has formed. This suggests that the carbide dissolution and the diffusion of carbon to cavities are controlling. Therefore, if the carbon supply is stopped, the attack is assumed to be mitigated. Factors such as carbon activity and carbide stability will influence the mitigation, as will be discussed later. Decarburisation, i.e. methane formation in this case, has been observed to decrease as the percentage of alloying elements increases in the steel [18, 32]; this is probably due to the precipitation of alloy carbides that are more thermodynamically stable than cementite.

  The incubation stage described earlier, exists even if the specimen contains cracks. This was shown by the work of Shewmon et al. in which they introduced a pre-cracked carbon steel specimen in a hydrogen-attack environment, the composition of which is listed as "carbon steel" in Table 1.1. It was nevertheless found that there was an incubation time prior to crack propagation [20]. This suggests that the incubation time is associated with an accumulation of methane pressure at grain boundaries and cavities before any damage or

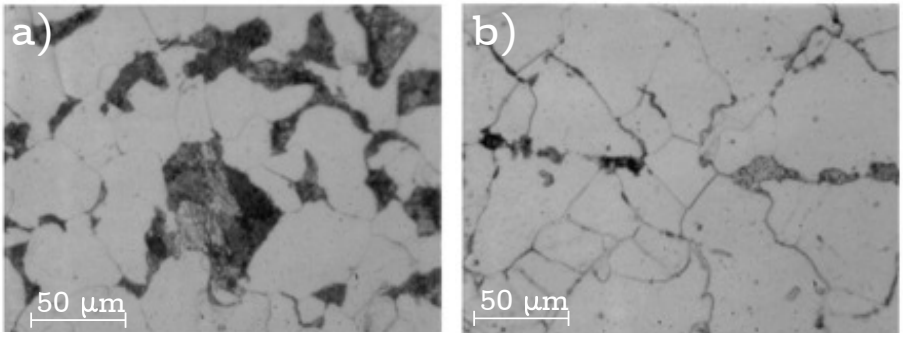

Figure 1.2: a) The normal microstructure of the pipe steel prior to failure in unaffected regions. b) Decarburisation shown as pearlite dissolution. The standard composition of the pipe steel can be found in Table 1.1. Adapted from [19] with permission from Elsevier.

cracking can happen. An increase in temperature or hydrogen pressure reduced the incubation time as shown in Figures 1.3 and 1.4. The attack seems to slow down eventually, which can be explained by the reduction of carbon available to react, represented by the least stable carbides.

The grain boundaries aid bubble nucleation as they are the favoured sites for carbide precipitation; therefore, grain boundaries define the surface along which bubbles nucleate and grow [2, 26]. Methane bubbles have been observed at grain boundaries as can be seen in Figure 1.5, which has been taken to suggest that grain boundary diffusion is the predominant mechanism by which bubbles nucleate and grow during the incubation stage [21]. However, the reason is likely to be much simpler, that carbides, presumably, the largest ones, exist at grain boundaries, which are favoured nucleation sites.

Bubbles have been seen to form in clusters during hydrogen attack; this could be due to a presence of a vacancy chemical potenital gradient between growing bubbles, which results in a stress distribution that aids the nucleation of new bubbles near that area [9]. These bubbles transform the ductile steel into one that pulls apart at the weakened grain boundaries and interfaces [33], a process associated with the second stage of the attack.

- The second, more pernicious, stage involves **the growth of the resulting cavities**, driven by methane pressure due to the continual reaction of carbon

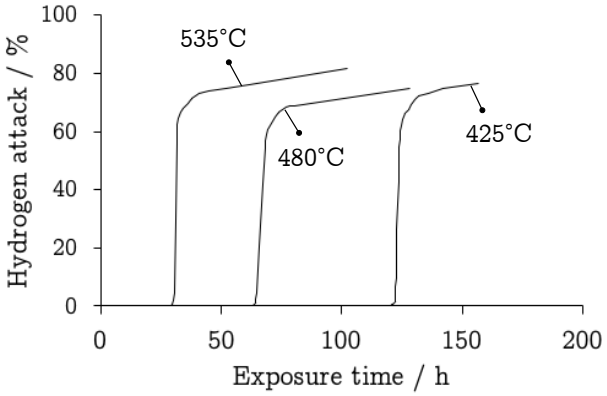

Figure 1.3: Hydrogen attack of a commercial steel as a function of increasing temperature at a constant hydrogen pressure of 4.8 MPa, composition listed as "commercial steel" in Table 1.1. Hydrogen attack percentage here is defined as the loss in reduction of area. Adapted from [17] with permission from CCC on behalf of AMPP Global Center, Inc.

Figure 1.4: Hydrogen attack of a commercial steel as a function of increasing hydrogen pressure at a constant temperature of 480°C, composition listed as "commercial steel" in Table 1.1. Hydrogen attack percentage here is defined as the loss in reduction of area. Adapted from [17] with permission from CCC on behalf of AMPP Global Center, Inc.

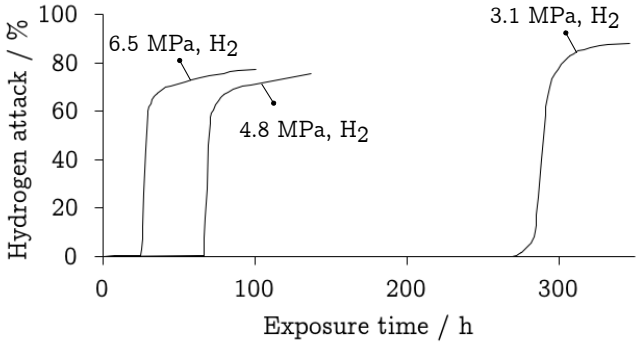

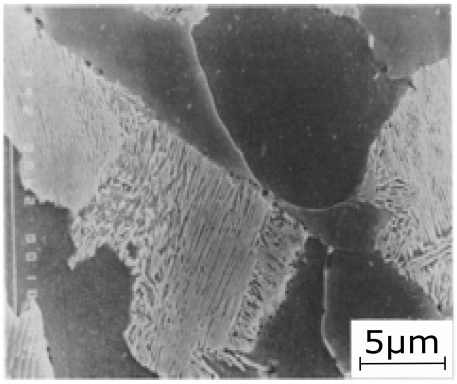

Figure 1.5: Bubbles can be seen at grain boundaries when A516 steel was exposed to hydrogen pressure of 17.2 MPa at 400°C for 99 h. Steel composition in Table 1.1. Reprinted from [21] with permission from Springer Nature.

and hydrogen at the void surface. This leads ultimately to microscopic cracking which in turn evolves by the linking of adjacent cavities, i.e., the growth of larger

cracks [26]. A variety of models have been formulated to estimate the growth of methane bubbles, based on two separate mechanisms; by grain boundary diffusion in which it is assumed that the material between bubbles remains elastic and growth takes place by iron diffusing away and carbon diffusing in to react with the hydrogen [2, 9]. This model is based on a constraint-free growth of methane, and it predicts a linear relationship between bubble growth rate and methane pressure and normal stress on the boundary, but it neglects any influence of the creep resistance of the material. The model by Parthasarathy [9] utilises the following procedure, considering that grain boundary diffusion would most likely occur by vacancy emission, then the vacancy emission rate (β) can be the starting point to estimate the strain rate of grain boundary diffusion ($\dot{\varepsilon}_{\mathrm{GD}}$) as follows:

$$\beta = \frac{2D_{\mathrm{b}}}{kT}\left[\frac{P_{\mathrm{CH_4}} - 2\gamma/r_{\mathrm{b}}}{\lambda^2\{d^2(1-d^2/4) - \ln(d) - 3/4\}}\right] \tag{1.1}$$

where D_{b} is the grain boundary self diffusivity of α-iron, k is Boltzmann's constant, T is the temperature, $P_{\mathrm{CH_4}}$ is the methane pressure, γ is the surface free energy of iron, r_{b} is the average bubble radius, λ is the half bubble spacing and d is r_{b}/λ. All parameters used in Equation 1.1 and the following equations are described in Table 1.2.

The vacancy emission rate can be related to the externally measurable strain rate by using the following equation for the grain boundary thickening rate ($\dot{\delta}_{\mathrm{b}}$):

$$\dot{\delta}_{\mathrm{b}} = \beta\,\delta_{\mathrm{b}}\,\Omega \qquad\qquad \mathrm{m\,s^{-1}} \tag{1.2}$$

where δ_{b} is the grain boundary thickness and Ω is the atomic volume. The volumetric strain rate of the steel is given by:

$$\frac{\dot{V}}{V} = N_{\mathrm{v}}(\pi\,\lambda^2\,\dot{\delta}_{\mathrm{b}}) \tag{1.3}$$

where N_{v} is the number of bubbles per unit volume and $(\pi\,\lambda^2\,\dot{\delta}_{\mathrm{b}})$ represents the volume change associated with each bubble. N_{v} can be also represented by the following equation:

$$N_{\mathrm{v}} = \frac{3.6}{g}\frac{f_{\mathrm{b}}}{\pi\,\lambda^2} \tag{1.4}$$

where g is the grain size and f_{b} is the cavitation fraction of the grain boundary. By combining all the previous four equations while considering that the linear strain rate is a third of the volumetric strain rate, the strain rate of grain boundary diffusion is given by the following:

$$\dot{\varepsilon}_{\mathrm{GD}} = \frac{7.2}{3}\left(\frac{f_{\mathrm{b}}}{g}\right)\frac{D_{\mathrm{b}}\delta_{\mathrm{b}}\Omega}{kT} \times \left[\frac{P_{\mathrm{CH_4}} - 2\gamma/r_{\mathrm{b}}}{\lambda^2\{d^2(1-d^2/4) - \ln(d) - 3/4\}}\right] \tag{1.5}$$

This model by Parthasarathy [9] is rather strange, in the sense that it treats the issue of bubbles forming on the boundary as uniform thickening of the boundary, given by Equation 1.2. Whereas in practice, bubbles and cavitated gaps do not form uniformly along the boundary because that would lead to immediate fracture. Parthasarathy then goes on in Equation 1.3 to express the volumetric strain rate in terms of the number of bubbles per unit volume, which gives quite a different expression than the one given by Equation 1.2. Therefore, it will be assumed that the grain boundary thickening rate ($\dot{\delta}_{\mathrm{b}}$) actually refers to the growth of the bubbles. This model is quite approximate, it is nevertheless a useful indication of grain-boundary diffusion in hydrogen attack. It quantitatively, although not accurately, expresses the relationship between the strain rate caused by grain-boundary diffusion with the atomic volume, the fraction of cavitated boundaries, the partial pressure of methane and spacing between bubbles. This model is not used further in this thesis.

The second growth mechanism, which is the power-law creep, allows the creep between bubbles to influence the growth as an additional factor [21, 30, 34]. These two models can go hand-in-hand during different stages of the hydrogen attack, as will be discussed later. Furthermore, stress cannot be ignored as an influencing factor as most of the equipment that undergoes hydrogen attack in refineries and petrochemical plants is subjected to external applied stresses which must be supported. Such stresses would be pivotal at this stage of attack when the grain boundaries have been weakened by the methane bubbles, which

Table 1.2: Descriptions of the parameters used in the grain boundary diffusion model.

Symbol	Description	Symbol	Description
D_{b}	Grain boundary self diffusivity of α-iron	d	r_{b}/λ
$P_{\mathrm{CH_4}}$	Equilibrium methane partial pressure	T	Temperature
r_{b}	Average bubble radius	k	Boltzmann's constant
δ_{b}	Grain boundary thickness	Ω	Atomic volume
f_{b}	Cavitated fraction of the grain boundary	g	Grain size
λ	Half bubble spacing	V	Crack extension rate
γ	Surface free energy of iron		

eventually do not allow them to withstand the applied stress, leading to the growth of cracks followed by a sudden loss of structural integrity, and ultimately catastrophic failures.

As well as cracks and fissures being accumulation sites for methane, they also introduce plastically deformed regions at the crack tips, which become favourable sites for the nucleation of microvoids and hence hydrogen accumulation and methane bubble formation, as seen in several case studies [4, 20]. Due to the intergranular nature of the cracking in this attack, the crack tips would lie on the grain boundary plane creating the stress field between the crack tip and nearest carbide/matrix interface, which in turn facilitates the propagation of the crack. This stress contribution to crack growth supports the validity of the previously mentioned power-law creep model, where creep influences bubbles and crack growth.

The hydrogen attack cracks have been characterised with tips that are not sharp, but discontinuous as can be seen in Figure 1.6 [20]. This can be due to the simultaneous nucleation of methane bubbles, formation of fissures and propagation of cracks. Methane bubbles form first followed by fissures followed by intergranular cracks, but these occur at different rates in different parts of the steel depending on factors such as distance from the surface, methane pressure

and carbide stability.

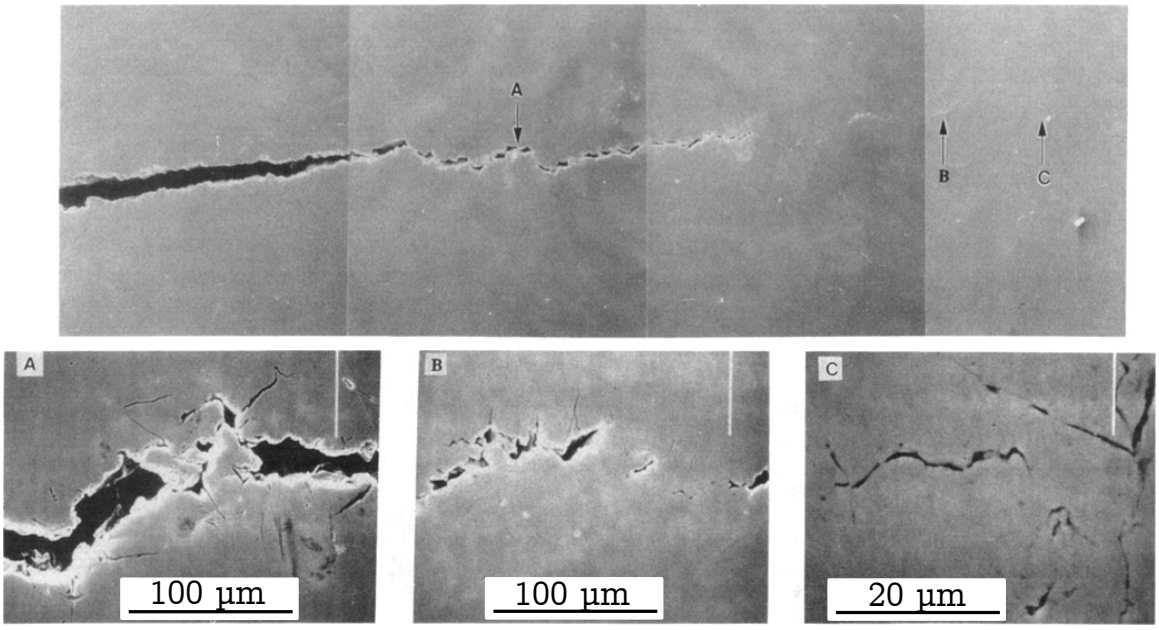

Figure 1.6: Left side of the top image shows an introduced fatigue-crack. a) Crack growth under the influence of hydrogen. b) and c) show discontinous cracks. Reprinted from [20] with permission from Springer Nature. Image (a) can be considered at a more advanced attack stage then image (c). Steel composition listed as "carbon steel" in Table 1.1. No scale bar was included in the source for the top image.

In advanced cases, tears can occur at weakened interfaces due to the extent of methane accumulation. If the tear is close to the surface, then a bulge or a blister can form, accelerating the catastrophic failure as can be seen in Figure 1.7 [3]. Hydrogen attack, at advanced stages, can deteriorate the mechanical properties of steel [3, 17, 18, 35]. Yield and ultimate strength of SAE 1020 steel were seen to decrease by 58% and 40% respectively after 360 h of hydrogen exposure at 525°C, Figure 1.8 [3]. SAE 1020 steel composition can be found in Table 1.1.

High temperature hydrogen attack can be considered to be a complex chemical-mechanical phenomenon, involving a number of processes. The mechanism following hydrogen diffusion into the steel, can be summarised as the following [4, 11, 31]

- Methane forms at carbide/matrix interfaces at grain boundaries.

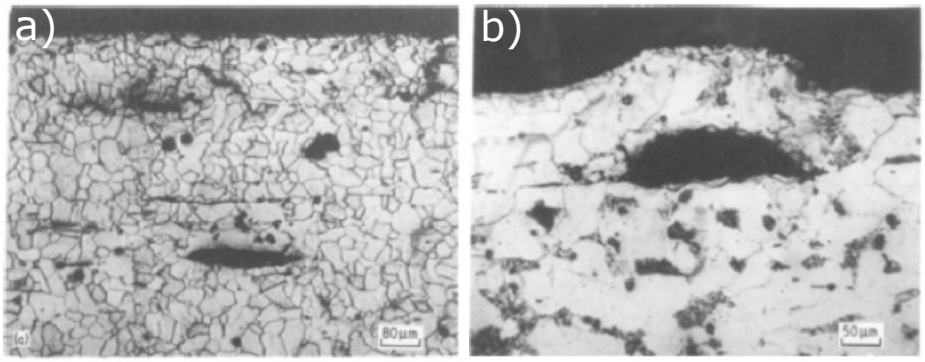

Figure 1.7: a) A tear forming far from the surface in SAE 1020 steel. b) A blister formed at the surface due to a nearby tear. Steel composition can be found in Table 1.1. Reprinted from [3] with permission from Springer Nature.

- Methane pressure builds up, new bubbles form on grain boundaries. Local creep caused by the bubbles contribute to their growth.
- Bubbles grow in size, weakening the grain boundaries, which leads to crack formation.
- Methane pressure builds up in the crack resulting in crack propagation, while stress fields are created around crack tips where further bubble nucleation occurs.
- Crack grows further by bubbles linking up to its tips, leading to failure by intergranular cracking.

1.2.2 Current best practice for designing against hydrogen attack

The industry has coped with hydrogen attack issues using an experience-based approach, expressed in the form of the so-called *Nelson curves* that define the combinations of temperature and pressure at which particular established steels can be used, although they do not include any externally imposed stresses. Figure 1 illustrates such curves, with the data points removed from the original diagram issued by the American Petroleum Institute, for the sake of clarity. The curves are not sacrosanct,

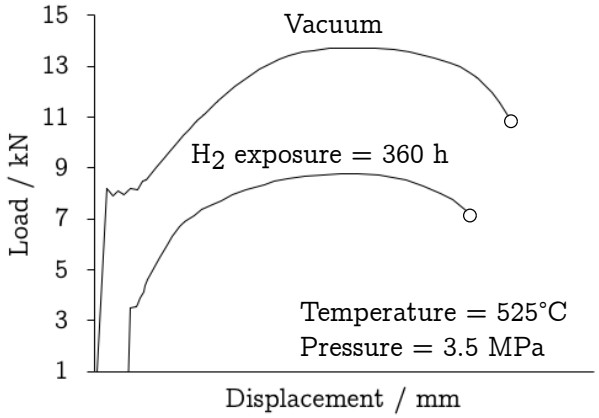

Figure 1.8: A comparison between the tensile curves for SAE 1020 steel at room temperature for a hydrogen-exposed specimen and an unexposed specimen. Composition of SAE 1020 steel can be found in Table 1.1. Reprinted from [3] with permission from Springer Nature.

but are modified on each occasion that a problem is discovered, For example, the curve for the C-0.5Mo steel was at one point removed with a recommendation to use instead the one for "carbon steel", in effect a downgrading of the ability of C-0.5Mo to cope with hydrogen attack [6, 7]. Nevertheless, the curves go some way in helping engineers ensure a best practice with respect to safe operating conditions in the environments of interest.

In *Nelson curves*, each curve has a vertical and a horizontal region, by which the previously mentioned growth mechanisms, on page 13, can be affected. The vertical section is associated with high temperature and hydrogen pressures lower than 6.90 MPa. Bubble growth is proportional to hydrogen pressure due to the increase of hydrogen availability for methane formation. Therefore, the bubble growth in the vertical region is limited by the hydrogen availability for the reaction and the iron diffusing away from the bubbles. The horizontal region is associated with low temperature and high hydrogen pressure, where bubble growth rate is determined by carbon availability and arrival at the bubbles. Cavities grow in this region by grain-boundary diffusion and the rate-controlling mechanism is the methane production at the cavity surfaces. In a case of rising temperature, the attack is expected to increase rapidly since a temperature increase facilitates more carbide dissolution,

carbon diffusivity and iron atoms movement away from growing bubbles [2, 36]. At a later stage, when bubbles coalesce and cracks propagate, the attack is controlled by creep as the amount of available carbon is depleted while methane formation rate and pressure are reduced [37, 38]. The earlier stage could be liable for the incubation period, while the latter stage corresponds to the fast attack period as illustrated in Figure 1.9.

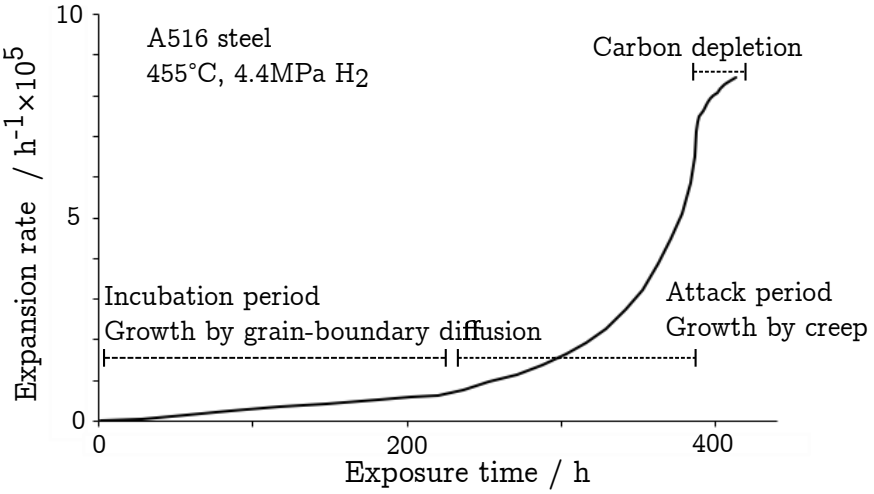

Figure 1.9: Expansion rate of a A516-steel specimen in hydrogen attack environment. The curve is adapted from [21], with further information added for illustration purposes. A516 steel composition can be found in Table 1.1. Adapted with permission from Springer Nature. Again, these two nucleation and growth mechanisms can be assumed to go hand in hand in most attack periods but each one can be more dominant at either the beginning or end periods of the attack.

Nelson curves can be used to select a steel grade for a given combination of hydrogen pressure and temperature, in order to avoid the risk of hydrogen attack over the intended service life of the component. Since they are entirely experience-based and do not contain information regarding the properties of a particular steel grade, it has to be assumed that the steels correspond to some standard set of industry-specified heat treatments and processing prior to hydrogen-exposure. Information such as microstructure, types of carbides precipitated, the degree of tempering and applied stess levels are factors that should play a vital role in the kinetics of hydrogen attack. There is a general feeling that design based on a better understanding of the

mechanism and kinetics of attack may lead to better utilisation of existing steels or the development of new ones that better resist the attack; for example, Martin et al. and Van der Burg et al. [4, 39].

1.2.3 Effect of stress

Grain-boundary diffusion and power-law creep are the dominating mechanisms for bubble nucelation and growth. With the introduction of stress, power-law creep becomes more dominant in advancing the attack along with stress-induced cavity growth [22, 40]. But how does stress facilitate faster hydrogen attack? Bubble nucleation in solids is associated with a volume increase, a tensile stress in the region of crack tips accelerates the rate of bubble nucleation at grain boundaries, therefore, stress decreases the work required for nucleation to occur [34]. A more detailed explanation of stress-induced cavity growth was given by Wanagel et al. [22], cavitation due to bubble nucleation in hydrogen attack occurs at grain boundaries. Creep deformation at low stresses and elevated temperatures is also known to introduce grain boundary cavitation, which can be explained by the tensile stress concentration at the boundaries and second-phase particles. Therefore, a hydrogen attack environment accompanied by stress means the co-existence of tensile stress concentration and methane pressure, which leads to an accelerated nucleation of bubbles and propagation of cracks.

Hydrogen exposure followed by creep testing was shown to reduce the creep-to-rupture life of steels that are relatively resistant to hydrogen attack, i.e. $2\frac{1}{4}$Cr-1Mo steel. The comparison was made between three hydrogen-exposed specimens subjected to three different stresses and another untreated specimen. The hydrogen-exposed specimens ruptured at lower durations and strains than the unexposed specimen, Figure 1.10 [22]. The faster rupture is due to the presence of grain-boundary cavities introduced by hydrogen exposure.

The simultanoues effect of hydrogen exposure and creep has also been investigated. Three $2\frac{1}{4}$Cr-1Mo steel specimens were subjected to different conditions. Scanning electron microscopy micrographs are shown in Figure 1.11. The microstructure in

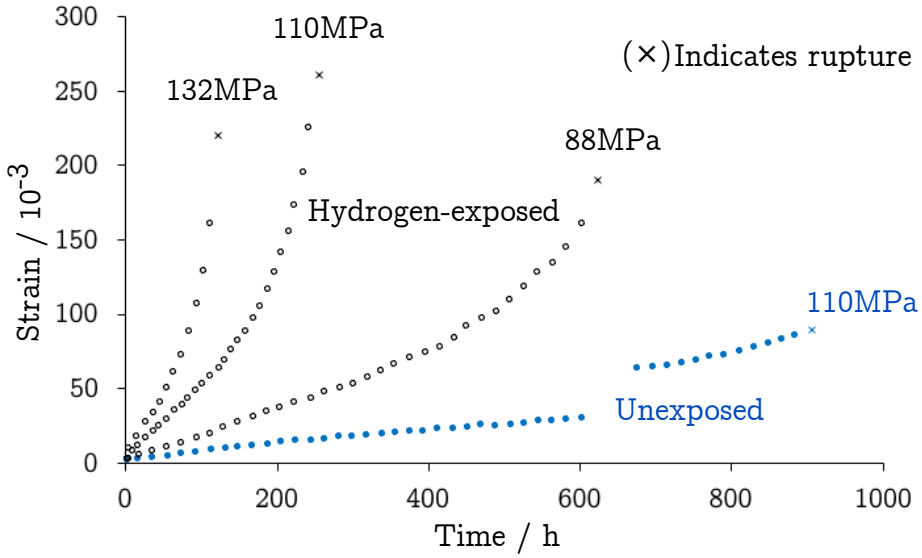

Figure 1.10: Comparison of creep curves of normalised and tempered $2\frac{1}{4}$Cr-1Mo steel between hydrogen-exposed and unexposed specimens. Hydrogen treatment conditions were 20 days at 600°C under a pressure of 13.8 MPa then the specimens were creep tested at three different stresses. Adapted from [22] with permission from ASTM International. Composition of $2\frac{1}{4}$Cr-1Mo (1) steel can be found in Table 1.1.

Figure 1.11a was creep-tested in air only, while specimen 1.11b was exposed to hydrogen followed by creep-testing. The specimen in Figure 1.11c was creep tested in a hydrogen environment. The density of the grain-boundary cavities was measured to be the highest under the combined effect of hydrogen exposure and applied stress in Figure 1.11c. Therefore, applied stress increases the cavity nucleation rate significantly, thermal and residual stresses can have a similar effect [22].

Cold work has been seen to enhance the rate of bubbles and fissures formation on the grain boundaries due to the increased local stresses along grain boundaries, which facilitate hydrogen attack by decreasing the work required for bubbles or fissures nucleation, as explained before [41]. Cold work appears to create stress-fields around cementite precipitates [42].

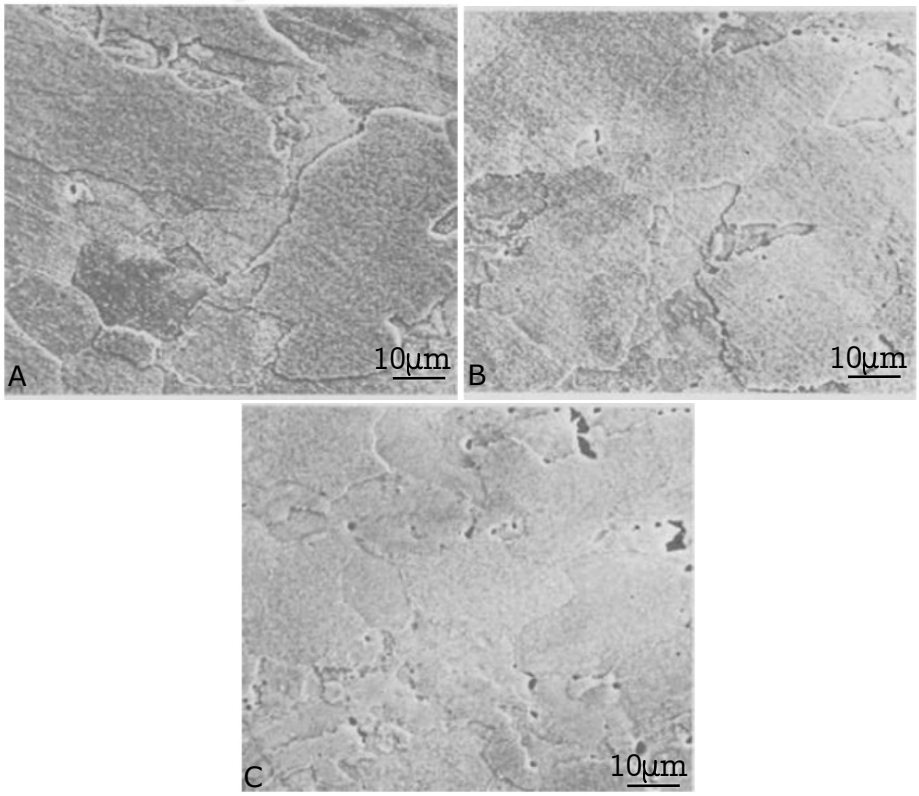

Figure 1.11: A) $2\frac{1}{4}$Cr-1Mo specimen creep tested in air at 600°C, 110 MPa for 38 days (cavity density of $5 \times 10^{-3}\mu m^2$), B) Specimen with a prior hydrogen exposure (600°C, 13.8 MPa, 20 days), and then creep tested at 600°C, 110 MPa stress for 7 days (cavity density of $16 \times 10^{-3}\mu m^2$), C) Specimen creep-tested in a hydrogen environment (13.8 MPa H_2, 600°C, 110 MPa stress for 10 days (cavity density of $38 \times 10^{-3}\mu m^2$). Adapted from [22] with permission from ASTM International. Composition of $2\frac{1}{4}$Cr-1Mo (1) steel can be found in Table 1.1.

1.2.4 Effect of carbide-forming elements on carbon activity

The presence of carbon in the steel is essential for hydrogen attack to occur. Carbon content and its stability in the carbides are factors that influence the attack [43, 44]. Previous research has shown that lowering the carbon content in the steel increases the incubation period as well as leading to less volume expansions when attack occurs, which can be explained by the availability of less carbon to form a substantial amount of methane gas to cause any noticeable damage [18]. The carbon stability in carbides can be defined as the tendency to be involved in a reaction, expressed as "carbon

activity (a_c)". Reducing carbon activity indirectly lowers methane bubble nucleation rate, hence the bubble number-density, which is an important factor in hydrogen attack [9]. Carbon activity also indirectly influences the growth rate of bubbles due to its linear relationship with methane pressure [23, 26]. Therefore, minimising carbon activity is crucial to mitigating hydrogen attack.

Carbon activity depends on the stability of the least stable carbide, and this is why sufficient tempering is seen to reduce both carbon activity and hydrogen attack rates as it precipitates more stable carbides. A tempering parameter can be used to quantify the extent of tempering. Equation 1.6 below was used by Parathasarathy and Shewmon [23] to calculate the tempering parameter:

$$\text{Tempering parameter} = T(20 + \log(t)) \tag{1.6}$$

where T is the temperature in Kelvin and t is the time in hours. Figure 1.12 shows that carbon activity accounts for most of the tempering effect as both carbon activity and hydrogen attack rates decrease monotonically with the extent of tempering.

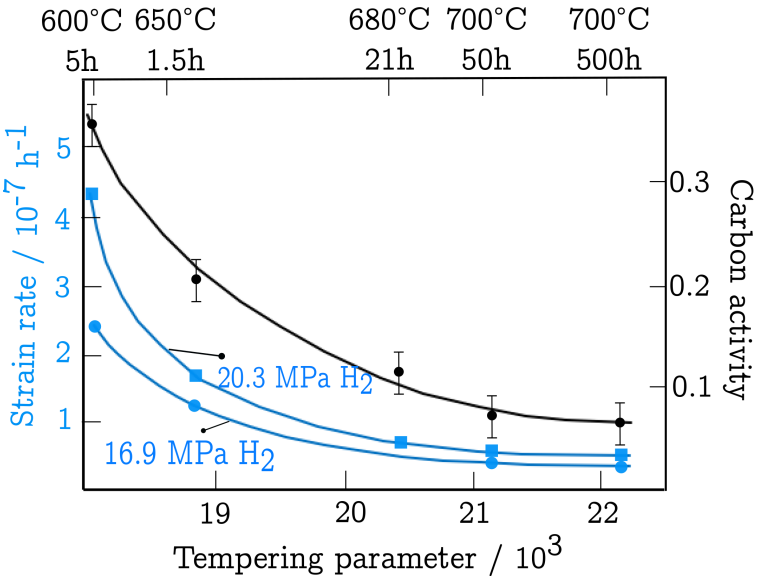

Figure 1.12: Effect of tempering on carbon activity and hydrogen attack rates in $2\frac{1}{4}$Cr-1Mo steel, composition listed as "A542 C13" in Table 1.1. Steels are exposed to hydrogen pressures of 16.9 and 20.3 MPa. Adapted from [23] with permission from Springer Nature.

The addition of alloying elements such as, Cr, Mo and V indirectly reduces carbon activity as they precipitate stable alloying-element carbides that are more dif-

ficult to break down for methane formation [30, 32, 45]. Parthasarathy and Shewmon [23] investigated the correlation between hydrogen attack rates and carbon activity for $M_{23}C_6$ carbide. The carbide is considered more likely to react with hydrogen when the carbon activity is high. They found a correlation between Cr/Fe ratio and carbon activity. Figure 1.13 illustrates that the greater the Cr concentration in the matrix, the smaller the carbon activity of $M_{23}C_6$, and the opposite for larger Fe concentrations in the carbide. It should be noted that the metal content of iron and chromium in the matrix and carbide are inversely proportional to each other. Therefore, a high chromium content indicates a low iron content, hence a reduced carbon activity, which leads to a higher hydrogen attack resistance. Sahara et al. calculated the formation energy of $M_{23}C_6$ for various Fe and Cr concentrations in "M" and concluded that the formation energy is reduced as the Cr content replaces the one of Fe in $M_{23}C_6$, which indicates an increase in the stability as the carbide is enriched with Cr [46].

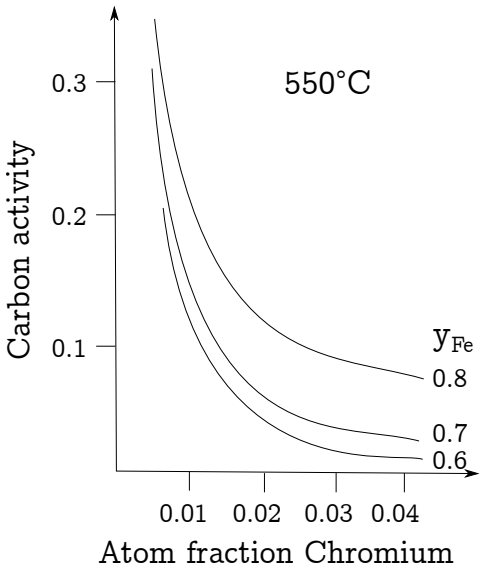

Figure 1.13: The relationship of carbon activity of $M_{23}C_6$ with atom fraction chromium in the matrix for various atom fractions of iron in the carbide metal content in $2\frac{1}{4}$Cr-1Mo steel, composition listed as "A542 C13" in Table 1.1 Adapted from Parthasarathy and Shewmon [23] with permission from Springer Nature.

The effect of Mo in ferrite on the equilibrium methane-pressure was investigated. If M_6C and M_2C dissolve due to hydrogen exposure, then Mo content is expected to increase in the ferrite matrix, and that was seen to reduce the equilibrium methane pressure, Figure 1.14 [30]. Wada measured the Mo and Cr content in ferrite and analysed their impact on carbon activity in $2\frac{1}{4}$Cr-1Mo steel, Figure 1.15. The steel composition is listed as "$2\frac{1}{4}$Cr-1Mo (2)" in Table 1.1. The Cr content was higher than the Mo content in ferrite, however, both decrease as the carbon activity in-

creases, which supports the findings by Parthasarathy and Shewmon [23], regarding the Cr content, Figure 1.13. The low carbon activity was associated with more M_6C precipitation [24].

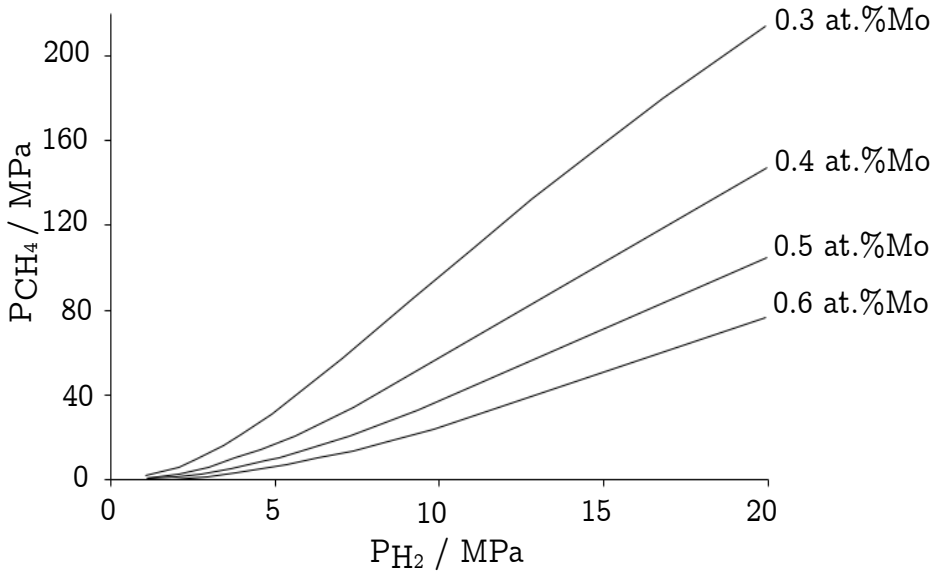

Figure 1.14: Computed equilirbium methane pressure for M_6C found in $2\frac{1}{4}$Cr-1Mo steel at 600°C in dependence of molybdenum conent in the matrix. Cr content in matrix is fixed at 0.17 at.%. Adapted from [30] with permission from Springer Nature.

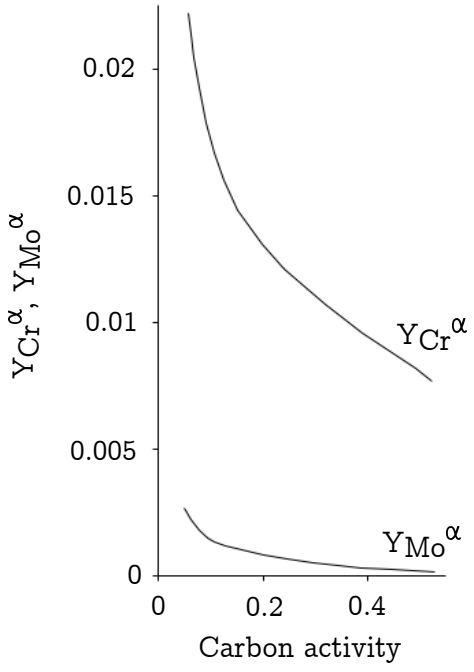

Figure 1.15: The relationship between carbon activity and equilibrium concentrations of Cr and Mo in ferrite phase, $Y_{\mathrm{Cr}}{}^{\alpha}$ and $Y_{\mathrm{Mo}}{}^{\alpha}$. Adapted from [24] with permission from Springer Nature.

The addition of vanadium is known to increase the resistance to hydrogen

attack as can be seen in Figure 1. Vanadium enhances creep rupture strength at elevated temperatures as well as tensile strength [45], which limits the attack mechanism of power-law creep. Vanadium also precipitates finer and higher-stability carbides than the aforementioned elements, which limits the other attack mechanism of grain-boundary diffusion. The effect of vanadium on the methane pressure was studied and found to decrease the carbon activity in M_7C_3 from 0.026 to 0.017, and in M_2C from 0.003 to 0.001, which confirms the positive impact of vanadium addition on hydrogen attack resistance [30]. Imanaka et al. examined the effect of vanadium content on attack rates in $2\frac{1}{4}$Cr-1Mo steel, and concluded that any vanadium additions below 0.1 wt% does not influence the resistance, however, the resistance increases dramatically with the addition of vanadium at concentrations greater than 0.1 wt% [47].

The addition of boron was found to decrease the formation energy of $M_{23}C_6$, which means increasing the stability of the carbide [46]. This was explained by the work of Abe [25], in which he explained that the addition of boron to 9%Cr steel delays the onset of creep acceleration. Creep occurs in two stages; transient creep involving the movement and annihilation of high-density dislocations and the acceleration creep, which is a result of the gradual loss of creep strength. In a steel, without boron, such as 9%Cr steel, where there is fine distribution of $M_{23}C_6$, the carbides are seen to coarsen in the vicinity of prior austenite grain boundaries during creep. The addition of boron reduces the rate of Ostwald ripening of those carbides, i.e. reducing their coarsening rate. The Ostwald ripening requires a local volume change around the growing carbide, which is accommodated by generation and migration of vacancies, as can be seen in Figure 1.16. If vacancies around the growing carbide are occupied by boron atoms, then the local volume change accompanying Ostwald ripening cannot be accommodated, hence reducing the coarsening rate of the carbides, which also delays the creep acceleration onset [25, 48]. The composition of 9%Cr steel with and without boron can be found in Table 1.1. As mentioned on page 15, creep plays a major role in the growth of bubbles and cracks in hydrogen attack, therefore the addition of boron could prove vital in mitigating the attack, by stabilising the carbides and delaying creep onsets.

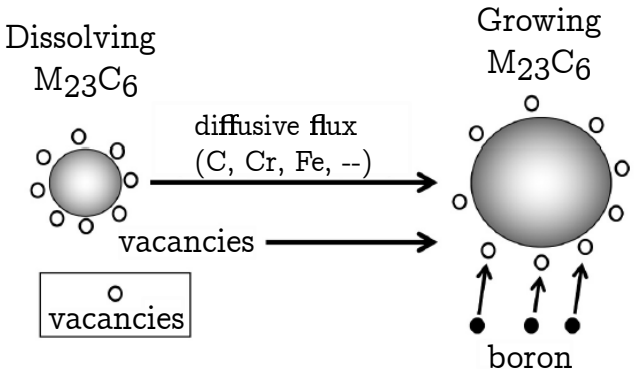

Figure 1.16: Accommodation of local volume change around a growing $M_{23}C_6$ carbide. Adapted from [48] with permission from Taylor & Francis.

1.2.5 Case studies of hydrogen attack

As mentioned previously on page 16, hydrogen attack is a complex chemical-mechanical phenomenon that involves a number of processes and depends on many factors that have been discussed. However, the combination of these factors is what can be used to try and improve steel resistance to the attack. Therefore, this section elaborates on different research cases that studied a combination of the influencing factors.

$2\frac{1}{4}$Cr-1Mo steel is used commonly for its hydrogen attack resistance at appropriately high temperatures and hydrogen pressures for refineries or petrochemical plants, Figure 1. Multiple researchers have developed models to calculate factors that influence the attack resistance of this steel, such as methane pressure, carbon activity and hence carbide stability. Reasons given for $2\frac{1}{4}$Cr-1Mo steel resistance include the precipitation of stable Cr- and Mo-rich carbides instead of cementite, which leads to a lower carbon activity, hence lower nucleation and growth rates of methane bubbles [9, 49].

Methane pressure varies with the type of carbide, Van der Burg et al. calculated the methane pressure, using a model they developed, for M_7C_3, $M_{23}C_6$ and M_3C, they did not include Mo-rich carbides due to the lack of information, at that time, on their thermodynamics data. As expected, cementite was associated with the

highest methane pressure followed by M_7C_3 and then $M_{23}C_6$. Times to failure were found to be one order of magnitude higher in M_7C_3 and $M_{23}C_6$ than M_3C [7]. This is an indication that $2\frac{1}{4}$Cr-1Mo steel is not always resistant to hydrogen attack, but its resistance is very dependent on the type of carbide precipitated, which highlights again the importance of examining and including such information in the current practice used, i.e. *Nelson curves*.

Schlogl et al. calculated the effect of the rest of alloy carbides on methane pressure in $2\frac{1}{4}$Cr-1Mo steel. Cementite, which is known to be the least stable carbide was not involved in these calculations, the carbides involved are; M_7C_3, $M_{23}C_6$, M_6C and M_2C. They calculated the Cr and Mo content in ferrite to be 1.7 at% and 0.3 at% respectively. It was found that at 600°C, the least stable carbide was M_6C with a_c = 0.33, followed by M_2C (a_c = 0.10) and M_7C_3 (a_c = 0.09), while the least methane pressure was associated with $M_{23}C_6$ (a_c = 0.06) [30]. The computed equilibrium methane pressures can be seen in Figure 1.17. M_2C and M_6C are Mo-rich carbides while M_7C_3 and $M_{23}C_6$ are Cr-rich carbides, hence it can be said that Cr-rich carbides can increase the attack resistance more than Mo-rich carbides, nonetheless, all these carbides would have lower carbon activity than iron carbide, i.e. cementite.

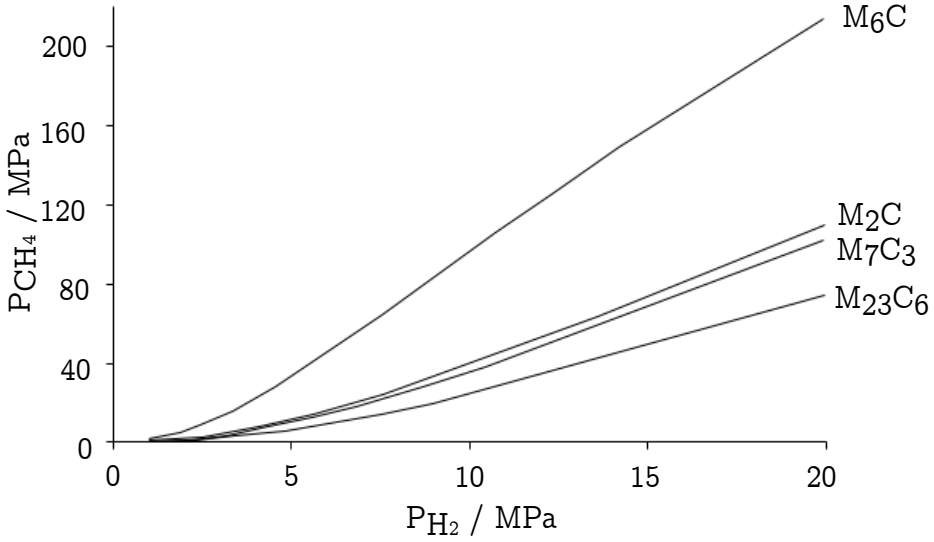

Figure 1.17: Computed equilibrium methane pressure for carbides found in $2\frac{1}{4}$Cr-1Mo steel at 600°C. Adapted from [30] with permission from Springer Nature.

Multiple researchers have compared the attack resistance of $2\frac{1}{4}$Cr-1Mo steel

with different steels. McKimpson et al. and Sundarajan et al. carried out dilatometric experiments to compare the behaviour of $2\frac{1}{4}$Cr-1Mo steel and "carbon steel", and found that the latter suffers attack rates of 3 to 4 magnitudes higher than $2\frac{1}{4}$Cr-1Mo steel [21, 26]. The addition of carbide-forming elements is the difference between the two steels, which consequently precipitate more stable carbides, hence lower carbon activity. Compositions of carbon steel and $2\frac{1}{4}$Cr-1Mo steel are listed in Table 1.1 as "A516" and "SA542, C13" respectively. Carbon activity can also be reduced by tempering the steel, which brings the carbides closer to their equilibrium states. However, extensive tempering could lead to the coarsening of carbides, which could impact the creep resistance of the steel, as discussed before. Thus, there is an interplay between creep effects and carbon activity that should be considered when choosing the optimal heat treatment for $2\frac{1}{4}$Cr-1Mo steel used in hydrogen attack environments.

Inclusions can have high stress-fields around them, which make them ideal locations for methane accumulation, explaining why different case studies have found inclusions within cracks or surrounded by bubbles [3, 4, 50]. The inclusions act as accumulation sites whether they are on grain boundaries or within grains, Figure 1.18 [40]. Cementite is also associated with methane bubbles, Figure 1.19.

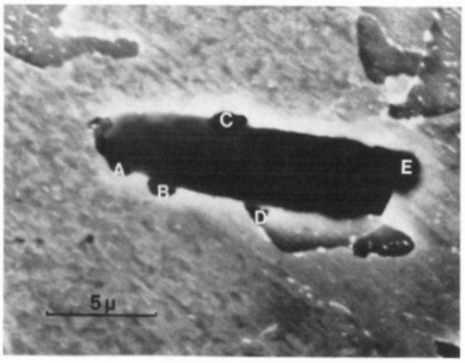

Figure 1.18: Cavities (A,B,C,D,E) around a MnS inclusion after hydrogen exposure in $2\frac{1}{4}$Cr-1Mo, composition was not included in the source. Reprinted from [40] with permission from Springer Nature.

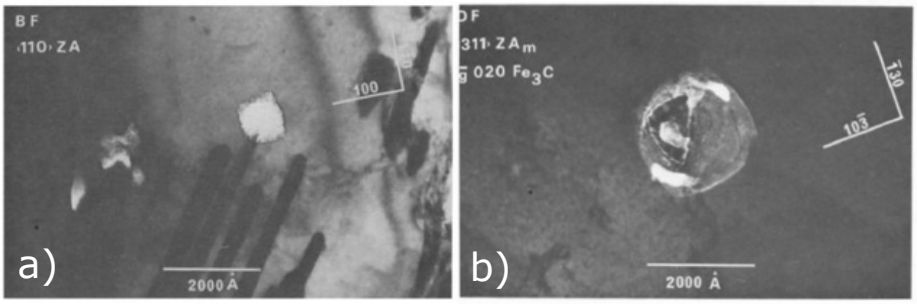

Figure 1.19: TEM micrographs of bubbles in 1020 steel a) bubbles associated with cementite plates. b) Small carbide inside the bubble being "digested". Steel composition was not included in the source. Reprinted from [51] with permission of Elsevier.

1.3 Interphase precipitation

The precipitation of stable carbides is vital in mitigating hydrogen attack. Conventionally, steels can be age-hardened by quenching followed by tempering normally in the range of 500-600°C. However, the stability of carbides can vary depending on steel composition and tempering conditions. These steels also can be transformed isothermally allowing interphase precipitation of stable carbides to precipitate instead of less-stable ones, if the steel contains strong carbide-forming elements such as vanadium, niobium, titanium or chromium. Interphase precipitation consists of periodic rows or sheets of precipitates that form simultaneously with the transformation from austenite to ferrite (γ to α) and follows the direction of the γ/α interface. The periodicity of the rows and spacing of precipitates within each row are factors that influence the mechanical properties of the steel. These factors are dependent on transformation conditions and composition [16, 52–56]. Different interphase precipitation mechanisms have been proposed by Davenport and Honeycombe [52], Honeycombe [57] and Ricks and Howell [58]. Interphase precipitation has been mainly utilised for its contribution to the steel strength, as shown by the recent success of *Nanohiten* steel [59]. However it has not been tested for its possible resistance of hydrogen attack. This section aims to explore the current literature on factors that should influence the carbides stability in interphase precipitation, hence hydrogen attack resistance.

1.3.1 Factors influencing interphase precipitation

Interphase precipitation can be achieved by austenitising the steel at a high temperature to ensure the solution of all carbides, followed by cooling to a temperature where the transformation to ferrite is expected with substitutional carbides precipitating at the advancing γ/α interface [28, 53]. Therefore, it can be expected that the precipitation of these carbides, that are of interest in hydrogen attack mitigation, is affected by the transformation temperature and the composition of the steel.

Transformation temperature: extensive research has been carried out to analyse interphase precipitation characteristics in various steels. To reiterate, the carbide sheets form with the movement of the γ/α interface by a step mechanism, thus the step height determines the sheet spacing. The smaller the height, the closer the precipitated sheets are to each other. The step height should decrease as the transformation temperature is decreased, due to greater driving forces at larger undercoolings, which permit a parallel step to be nucleated [60]. This is why various researchers have found that lowering the transformation temperature decreases the sheets spacing, i.e., produces a finer scale of carbides. The driving force for step nucleation will be smaller at high temperatures, therefore sheet spacing is seen to increase, Figure 1.20 [16, 28, 54, 56, 61].

The transformation rate can be slowed down depending on the alloying-elements present, e.g. a finer scale of precipitation is seen in Ti, Nb and V steels than in Cr, W and Mo steels due to slower transformation in the latter [16, 54]. Campbell and Honeycombe reached the same conclusion in relating the transformation temperature to sheet spacing in Cr-steels, the spacing was coarser than that of V and Ti steels, which is thought to be due to the slower transformation in Cr-steels. They also noticed irregular spacing within the same specimen, which can occur due to extensive nucleation when the transformation starts, leading to a carbon depletion in other parts of the specimen of Cr-steel, which was proven by the witnessed carbide-free regions around areas with dense precipitation [62]. Transformation temperature also influences precipitate size, ferrite volume fraction and grain size. Both the particle size

and grain size are reduced as the transformation temperature is lowered, Figure 1.21, while the opposite occurs for ferrite volume fraction, Figure 1.22. Hardness increased at lower transformation temperatures due to the precipiation of a greater number-density of carbides [27, 28, 61].

Transformation temperature clearly influences the precipitation characteristics, however, its effect on hydrogen attack resistance is unknown, although one could argue that the resistance should be higher at lower transformation temperatures due to the increased carbide number-density; nonetheless, stable carbides are expected to precipitate at all temperatures.

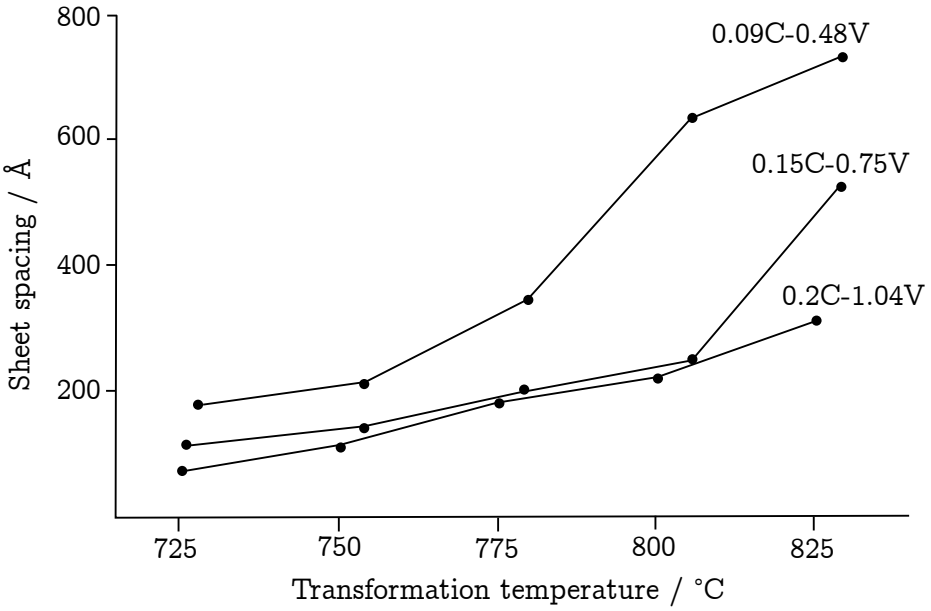

Figure 1.20: Effect of transformation temperature on the sheet spacing of vanadium carbides in different vanadium steels. Adapted from [53] with permission of Taylor & Francis.

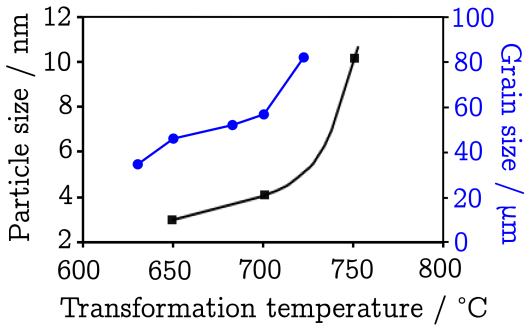

Figure 1.21: Grain size and particle size as functions of trasnformation temperature in Ti-Mo bearing steel and $\frac{1}{2}$Cr-Mo-V respectively. The relationship has been agreed-upon by most researchers on interphase precipitation steels. Adapted from [27, 28] with permission from Elsevier and Taylor & Francis. Compositions of steels can be found in Table 1.1.

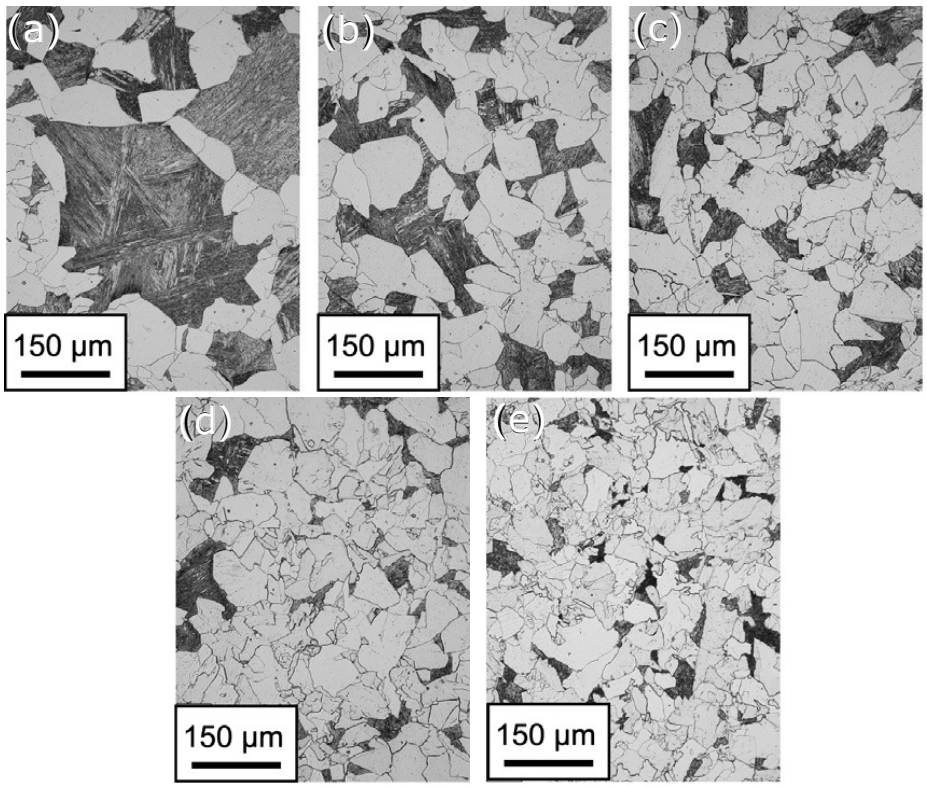

Figure 1.22: Optical micrographs for Ti-Mo bearing steel transformed isothermally for 30 min at (a) 720°C, (b) 700°C, (c) 680°C, (d) 650°C, (e) 630°C. Ferrite fraction is higher at lower transformation temperatures. Reprinted from [28] with permission from Elsevier. Steel composition can be found in Table 1.1.

Stoichiometric composition: it is not only by increasing the content of alloying-elements that the attack resistance can be increased, but the proportions of which alloying-elements are to carbon that matter. If the composition is stoichiometric, then all of the carbon will be tied up with stable carbides upon the completion of transformation. That would ensure the minimum possible carbon activity, which would lead to higher attack resistance. If carbon content is more than necessary to tie up the alloying-elements in carbides, then it will tend to concentrate in untransformed austenite, which transforms to martensite upon quenching, as seen by Dunlop and Honeycombe [27]. The presence of "free" carbon in the steel would deteriorate the hydrogen attack resistance.

Prior austenite grain boundaries (PAGB): Moon et al. investigated PAGB size effect during the γ to α transformation in a high-hardenability steel, they found out that smaller PAGB size lead to a faster completion of the γ to α transformation, i.e. transformation was completed after 48 h and 120 h when the PAGBs size was 49 µm and 1083 µm, respectively, Figure 1.23. The PAGBs act as nucleation sites for the ferrite, therefore finer PAGB size means more nucleation sites, which explains the transformation completion dependence on PAGBs [29, 63]. As mentioned before, that the completion of the γ to α transformation is important in lowering the carbon activity, therefore, decreasing the PAGBs size can help in achieving that.

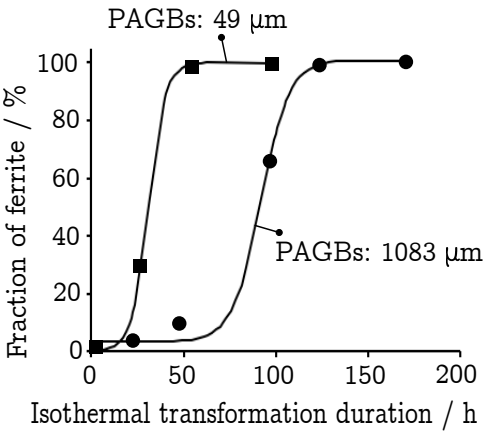

Figure 1.23: Completion of ferrite transformation as a function of prior austenite grain boundary sizes in 9Cr-1.5Mo steel, composition listed in Table 1.1. Adapted from [29] with permission from Elsevier.

Alloying elements: as mentioned on page 31, the dispersion scale is different between carbide-forming elements. It can be altered further by the addition of other elements, such as Mo. The addition of Mo in Ti-Nb bearing steel was seen to refine

the size of carbides as well as the spacing between the rows while retarding their coarsening behaviour. While the precipitation of Mo as a carbide constituent only occured during the early stages of precipitation, as Mo is not thermodynamically favoured as a solute in (Ti,Nb)C, however, it reduces the misfit between the ferrite and the carbide, which leads to easier nucleation and explains the finer scale of precipitation [59, 64]. The coarsening retardation is also important, especially on a large-scale steel production [65]. The addition of "ferrite formers" such as Al or Si accelerates the γ to α transformation, allowing it to occur at higher temperatures while decreasing the spacing between sheets. The addition of "austenite formers" such as Ni or Mn has the opposite effect on the transformation [53, 66]. Therefore, the use of ferrite formers could be more useful in mitigating hydrogen attack as they would increase the chance of ferrite formation where stable carbides can precipitate.

1.4 Summary of literature review

The review has described the phenomenon of hydrogen attack in steel and its determining factors; environmental parameters such as pressure, temperature and stress or metallurgical such as carbon activity and carbide stability all are influential. Hydrogen attack is a complex phenomenon that is dependent on methane formation, which can be said to be mainly determined by the carbon activity in the steel. Therefore, by minimising carbon activity, hydrogen attack can be mitigated. Current practices do not specify vital information about the steel grade such as carbides precipitated or degree of tempering. These parameters were to be investigated in this project, building upon current knowledge. The review finished with a discussion on the interphase precipitation mechanism, which can produce steels with a fine-scale of very stable carbides that leave a minimal carbon activity in the matrix. This mechanism will be tested for the first time in terms of its hydrogen attack susceptibility in this project.

Chapter 2

Experimental methodology

The first stage in this project was focused on examining a commercially-used steel before and after hydrogen exposure at elevated temperatures in order to explore the vulnerabilities in the current designing standard. The second stage was to utilise the analysis findings to introduce possible mitigation methods to hydrogen attack. These steels were examined in a hydrogen-attack inducing environment to validate if the mitigation was successful or not. This section elaborates on the experimental methods used for both stages.

2.1 Materials

Three steels were examined in this project; a commercial steel, $2\frac{1}{4}$Cr-1Mo (F22), that currently is used in hydrogen-attack applications. The other two steels are HT10 and vanadium steels, which are proposed for mitigation purposes. The compositions of F22 and a vanadium steel were analysed at Inspiratech using inductively coupled plasma for all elements except carbon and sulphur, which were analysed by combustion. The composition of HT10 was taken from previous work at the University of Cambridge [67]. All compositions are listed in Table 2.1.

Table 2.1: Chemical compositions (wt%) of all steels used in the present work.

	C	Cr	Mo	Ni	V	Mn	Si	P	S	Cu	Al
F22	0.14	2.24	0.97	0.37	0.005	0.42	0.1	0.007	0.001	0.04	0.043
HT10	0.12	2.5	1.52	3.2	0.46	0.57	–	–	–	–	–
V-steel	0.17	–	–	–	1.04	–	–	0.006	0.005	–	–

Sample preparation

Specimens were cut in different sizes using an ATM Brilliant 220 cutting machine. For hardness testing, optical microscopy, scanning-electron microscopy and electron back-scatter diffraction, specimens were hot mounted in conductive bakelite, ground gradually using silicon carbide (SiC) paper up to P2500, then polished with 6 µm and 1 µm diamond paste. An extra step of polishing with colloidal silica on a polishing cloth was needed for specimens analysed using electron back-scatter diffraction. Etching is needed to reveal the microstructure and it was performed using a nital etchant with nitric acid concentrations varying from 2% to 5% depending on the steel. Etching was not needed for observing voids and cracks.

For transmission electron microscopy, sample were cut as 200-300 µm sheets, which were thinned down to around 100 µm using SiC paper. 3 mm disc samples were punched out of the sheets, which were then thinned further to around 50 µm. Samples were then electropolished in a Struers TenuPol-5 machine at a temperature of 10°C using a solution of 5% perchloric acid, 25% glycerol and 70% ethanol solution. The optimal flow rate and operating voltage were determined separately for each specimen.

2.2 Elevated temperature, pressurised hydrogen testing

The elevated temperature, pressurised hydrogen testing was carried out at at The Welding Institute (TWI); the autoclave there can achieve up to 525 °C and a hydrogen

pressure of 10 MPa.

The specimens are placed within three cylinders of 316L austenitic stainless steel (Figure 2.1) with each cylinder placed at the centre of a tube furnace (Figure 2.2), i.e. the position of peak temperature. The specimens were placed with identification letters facing upwards as shown in Figure 2.1. The small hole in the middle of the cylinder is where a thermocouple was located. The screws at the end of the specimens are only space savers to limit the volume of hydrogen needed but they do not seal the holes; they also are made of 316L stainless steel. Therefore, when hydrogen is supplied, it fills all the gaps around the specimens that are not occupied by space savers.

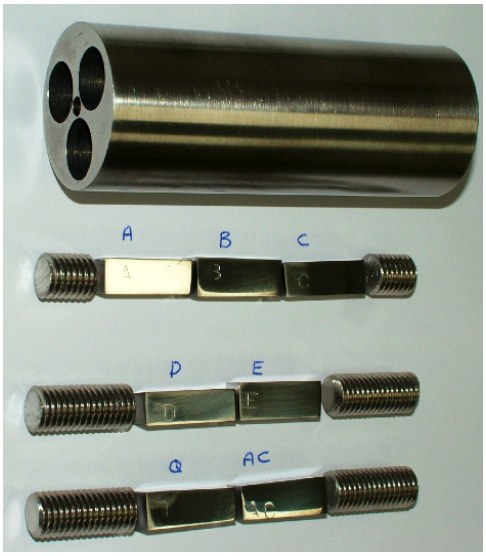

Figure 2.1: The specimens are placed in the holes of the cylinder.

2.3 Dilatometry

Dilatometry was used for the analysis of phase transformations as well as the heat treatment of the interphase-precipitation specimens. Phase transformations across different temperature profiles result in specific changes in the lattice parameters, which in turn lead to macroscopic volume changes in the specimen.

The dilatometer DIL805A/D was used in the quenching mode with 5 mm diameter and 10 mm long specimens. Specimens were polished with silicon carbide

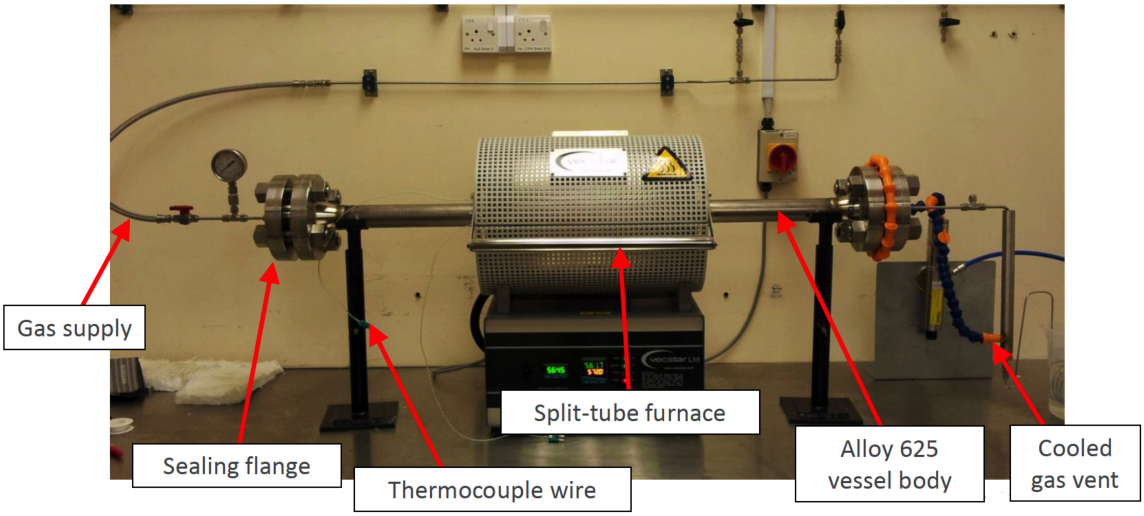

Figure 2.2: The cylinder in Figure 2.1 is placed in the middle of the furnace, where the temperature is at its peak. Hydrogen is supplied through the vessel body.

paper to remove any oxide layers. A thermocouple was then spot-welded onto the sample surface. All specimens were inductively heated in vacuum. The dimensional change in the longitudinal direction, i.e. length of the specimen, was measured using a linear variable differential transducer connected to push rods holding the specimen. The change in the diameter was measured using a laser with a precision of $\pm 1\,\mu m$. Silica push rods were used for temperatures lower than 1100°C, while aluminium oxide rods were used for any higher temperatures. Argon gas was used during cooling.

2.4 Hardness measurements

Vickers hardness was then measured using a Qness Q60 automatic indenter with a 10 kg load. The applied load produces a pyramidal indentation on the sample surface, in which its size changes depending on the material's hardness. The average of the two diagonals made by the pyramidal indentation is measured and the hardness can be estimated using the following equation [68]:

$$\mathrm{HV} = \frac{0.1891F}{d^2} \tag{2.1}$$

where F is the applied load in Newtons and d is the measured diagonal length of the indentation in mm. Work hardening occurs around any indentation, therefore, a spacing of at least $2.5\,d$ was left between adjacent indentations to eliminate any possible effects from the work-hardened regions. Microhardness was measured using 100 g load on etched specimens when analysis of hardness across different phases in the specimen was required.

2.5 Microstructural characterisation

2.5.1 Optical microscopy

Optical microscopy was performed using a Leica Microsystems DM2500M upright light microscope with a magnification ranging from 5-500×. A magnification of 20× was used for analysing the volume fraction of voids before and after hydrogen exposure. A DFC295 camera was used for capturing images that are processed using Leica application suite software.

ImageJ software was used to estimate the volume fraction of voids, by adjusting the threshold of images to light up the voids to calculate their fraction, e.g., Figure 2.3.

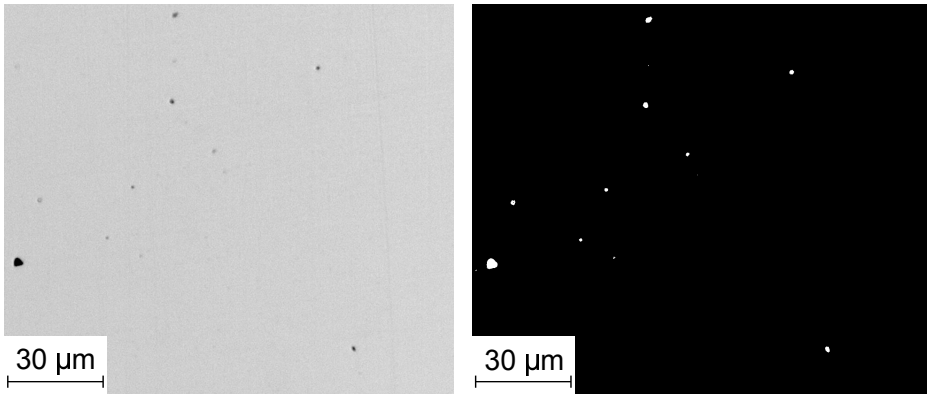

Figure 2.3: Using ImageJ, threshold is adjusted in the left image to produce a map of the voids on the right.

2.5.2 Scanning electron microscopy

Scanning electron microscopy (SEM) was performed using Nova NanoSEM 450 microscope with an Everhart-Thornley Detector operating with a voltage of 15 kV and a minimum working distance of 6 mm for microstructural analysis in secondary-electron imaging mode, since etching creates a clear topographic difference between phases in the steel, which are better captured using the secondary-electron mode.

2.5.3 Electron back-scatter diffraction

Electron back-scatter diffraction (EBSD) was conducted using a ZEISS GeminiSEM 300 field emission gun scanning electron microscope at magnifications up to 3000×. Specimens were tilted at 70° to the electron beam which was accelerated at 20 kV. The aperture size was fixed at 120 µm and the working distance was kept at a minimum of 15 mm while the step size was set at 0.03 µm. This technique was used in this project to investigate if any carbide depletion occurs around inclusions and voids.

2.5.4 Transmission electron microscopy

The FEI Tecnai Osiris FEG TEM, fitted with an energy dispersive spectroscopy detector, was used for microstructural characterisation of very fine carbides, as well as carbide identification. The microscope has an accelerating voltage of 200 kV. Carbides reflections were identified using diffraction patterns, while their morphology and orientation, especially in interphase-precipitated steels, were revealed with dark-field imaging. Scanning transmission microscopy (STEM) was used for high resolution imaging of fine carbides that could not be carried out using SEM.

2.5.5 Synchrotron X-ray analysis

The purpose of using synchrotron X-ray analysis is to measure the small volume fraction of carbides before and after hydrogen exposure to determine the carbides that have been depleted by hydrogen. Experiments for the first stage of the project were conducted on The Swedish Materials Science Beamline P21.2 at PETRA III in the Deutsches Elektronen-Synchrotron (DESY). The experiments for the second stage of the project were carried out on the I12 beamline at the Diamond Light Source in Oxfordshire. Monochromatic diffraction with high intensities was used in all experiments to allow measurement of the small volume-fractions of carbides.

The X-ray wavelength was 0.2066 Å, monochromated using diffraction. X-ray detection was done using a PILATUS3 X CdTe 2M detector with pixel size of 172 µm × 172 µm. The sample detector distance was determined to be 2800 mm to allow the largest possible diffraction at $2\theta < 15°$, where the most intense peaks of carbides are expected. The X-ray beam size was chosen to be 0.5 mm × 0.5 mm with a dwell time of 5 s per measurement point.

Hundreds of images were captured, spaced out evenly across each specimen. Analysis was performed using Python modules; pyFAI-calib2 for detector calibration and pyFAI-integrate for data reduction. The products of all the analysis are the X-ray diffraction patterns, which are fitted using Rietveld analysis by the "Quantitative Analysis" wizard in MAUD (Materials Analysis Using Diffraction) [69, 70]. The background signal, incident X-ray intensity, lattice parameters, crystallite sizes and isotropic microstrains of all expected phases were refined using Rietveld method, following the guidlines in the work of McCusker et al. [71], Lutterotti et al. [72] and Wenk et al. [73], to achieve the best possible fit.

Carbide structures: measuring the volume fractions of carbides before and after hydrogen exposure can be a clear indication of "weakest" carbides to be a carbon source for methane formation. This method, to our knowledge, has not been used previously in determining the stability of carbides for hydrogen attack applications.

$M_{23}C_6$ is rarely observed within steels in its purest form, $Cr_{23}C_6$. Instead, Cr can be substituted by many other metal atoms such as Fe, Co, Mo and Mn. This carbide mostly nucleates at the prior austenite grain boundaries, followed by less-coherent twin boundaries and other defects [74, 75]. They can also grow by attracting the chromium from the less-stable carbides leading to the dissolution of those carbides such as M_7C_3 [76]. $M_{23}C_6$ has a $Fm\bar{3}m$ space group with a face-centred cubic crystal structure where the lattice parameter $a \simeq 10.65$ Å [75, 77]. $M_{23}C_6$ in $2\frac{1}{4}$Cr-1Mo steel is known to be rich in iron with chromium and some molybdenum [78, 79]. Chromium-enrichment occurred upon longer tempering durations and higher tempering temperatures $> 500°C$ [80], which suggests that this carbide is the equilibrium Cr-rich carbide in the investigated steel, $2\frac{1}{4}$Cr-1Mo.

M_7C_3 evolution can be broken down into three stages: nucleation, increase in phase fraction/enrichment by alloying-elements at the expense of cementite, and finally dissolution in favour of $M_{23}C_6$ [76, 81]. It has been found that M_7C_3 in $2\frac{1}{4}$Cr-1Mo steel does not get the chance to reach the equilibrium composition so it can be considered a transition carbide to be replaced eventually by $M_{23}C_6$. M_7C_3 carbides in this steel are also typically enriched with Cr, Fe and some Mo. The carbide has an orthorhombic crystal structure, space group $Pmcn$ with lattice parameters $a \simeq 7.019$ Å, $b \simeq 12.142$ Å and $c \simeq 4.526$ Å [82]. Because the b/c ratio is almost $\sqrt{3}$, M_7C_3 can also be represented with a hexagonal crystal structure with space group $P6_3mc$, where $a = b \simeq 14.02$ Å and $c \simeq 4.526$ Å, Figure 2.4 [75, 83, 84]. The latter structure was the one observed in the current work on $2\frac{1}{4}$Cr-1Mo steel.

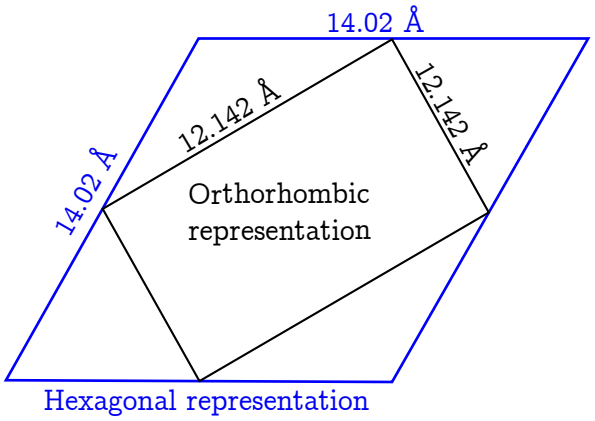

Figure 2.4: The relationship between the two possible crystal structure representations of M_7C_3. Adapted from [75].

M_6C is also a transition carbide replaced, at advanced tempering stages, by $M_{23}C_6$ in the investigated steel, $2\frac{1}{4}$Cr-1Mo. However, M_6C is the equilibrium carbide in austenitic stainless steels where it often nucleates on the expense of $M_{23}C_6$. This could be explained by the high Cr/C ratios in austenitic stainless steels, which reduces carbon activity favouring the precipitation of Mo-rich M_6C carbides, as seen by Wada [24, 75]. M_6C precipitation is believed to contain low molybdenum initially when most of present Mo is tied up in Mo_2C. Further dissolution of the metastable Mo_2C carbides grants more Mo for M_6C enrichment, Figure 2.5 [79]. M_6C has a face-centred cubic structure, $Fd\overline{3}m$ space group with a lattice parameter $a \simeq 11.0\,\text{Å}$ [75].

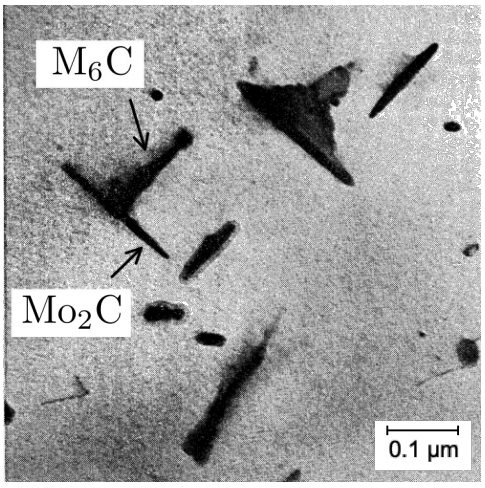

Figure 2.5: M_6C growing on the expense of the metastable Mo_2C carbide. Adapted from [85].

Mo_2C was identified initially, using X-ray diffraction, to have a hexagonal crystal structure with space group of $P6_3/mmc$. However, the positions of carbon atoms could not be verified experimentally due to the weak X-ray scattering of carbon atoms. Those positions were later verified by Parthé, using neutron diffraction, to determine the crystal structure of Mo_2C to be orthorhombic with space group $Pbcn$, where lattice parameters $a \simeq 4.72\,\text{Å}$, $b \simeq 6.00\,\text{Å}$ and $c \simeq 5.19\,\text{Å}$. The relative positions of metal atoms are identical in both crystal structures [75, 86]. Mo_2C is considered unstable as its volume fraction decreases with increasing tempering durations, which is expected to be in the favour of M_6C increasing in volume fraction [76]. Mo_2C adopts a needle-like shape when precipitated in ferrite, Figure 2.6.

Vanadium carbide in steel has been considered originally to be V_4C_3, $Fm\overline{3}m$ space group, with a lattice parameter $a \simeq 4.157\,\text{Å}$ [75, 87]. However, upon further examina-

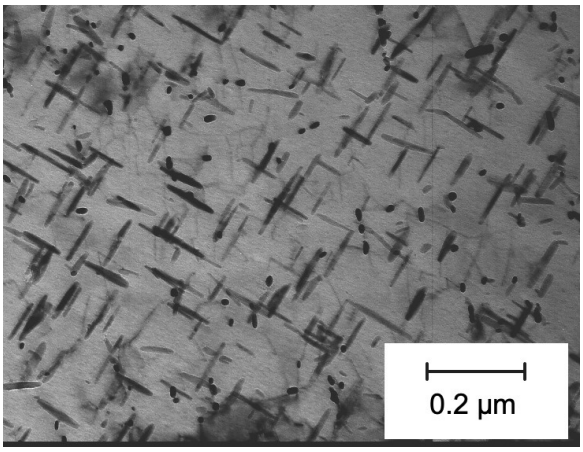

Figure 2.6: A micrograph of Mo_2C needles. Three varients can be observed in respect to $\langle 1\,0\,0 \rangle_\alpha$ when the thin foil is parallel to $\{1\,0\,0\}_\alpha$: two orthogonal needles and the third variant can be seen as the circular cross-sections as they are precipitated along the normal to the plane of the foil [75].

tion of electron diffraction patterns, it was shown that vanadium carbide precipitated in steel are V_6C_5 of a monoclinic crystal structure, which contains ordered vacancies in the carbon sublattice, Figure 2.7. The lattice parameters are $a \simeq 5.09\,\text{Å}$, $b \simeq 8.82\,\text{Å}$ $c \simeq 1.018\,\text{Å}$, $\beta = 109.47°$, and the space group is C2/m [75, 88]. Vanadium carbides in steels are associated with strain fields that trap diffusible hydrogen leading to the mitigation of embrittlement [89]. But the behaviour of those traps has not been investigated in regard to hydrogen attack, which would be interesting to analyse in this work.

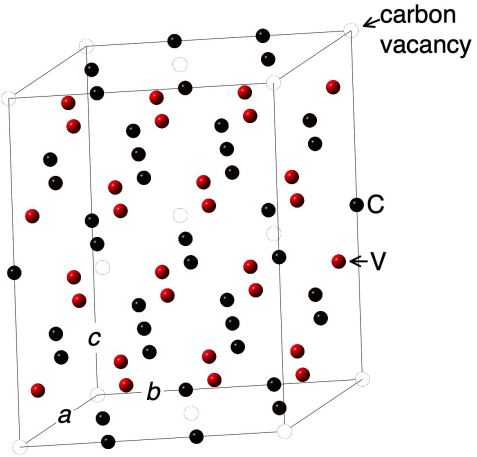

Figure 2.7: A schematic representation of V_6C_5 monoclinic crystal structure where ordered vacancies reside in the carbon sites [75].

Chapter 3

Elevated temperature attack by H_2 on commercial steels

3.1 Introduction

The work presented in this chapter deals with one of the most common steels used in environments that may induce hydrogen attack, the classical alloy referred to commonly as $2\frac{1}{4}$Cr-1Mo steel. The alloy has been used for more than half a century in the construction of fossil fuel powered electricity generating plants because it has a sufficient hardenability to achieve a bainitic microstructure in very large components, with the structure being subsequently secondary hardened to generate substitutionally-alloyed carbides that resist long-term creep deformation [80].

In the context of the petrochemical industry, Figure 1 indicates that the $2\frac{1}{4}$Cr-1Mo steel is susceptible to hydrogen attack at temperatures as low as 455°C when the hydrogen partial pressure is at a minimum of 13.7 MPa.

The specific aim of the present work was to examine what factors affect the hydrogen attack resistance of $2\frac{1}{4}$Cr-1Mo steel and to relate the observations to the types of carbides precipitated and how close those carbides are to their equilibrium state. The microstructural effect on the resistance was also investigated alongside

the influence of different tempering parameters. Finally, the susceptibility of carbides to hydrogen attack when present in the proximity of the steel surface was examined relative to those located deeper within the steel.

3.2 Experimental procedure

3.2.1 Heat treatment of $2\frac{1}{4}$Cr-1Mo steel

As mentioned before, the hydrogen reacts with the carbon in the steel to form methane, which leads eventually to cracking and failure. Carbon is usually present in the form of carbides. Therefore, studying the depletion of carbides is useful in understanding hydrogen-attack resistance. Because of the alloying elements present in $2\frac{1}{4}$Cr-1Mo steel, a variety of carbides can precipitate depending on the heat treatment. It is the nature of the carbides and the microstructure that determined the selection of heat treatments in the present work. The composition of the steel used, "$2\frac{1}{4}$Cr-1Mo", is listed in Table 3.1.

Table 3.1: Chemical composition (wt%) of the $2\frac{1}{4}$Cr-1Mo used in the present work.

C	Si	Cr	Mo	Ni	Mn	P	S
0.14	0.1	2.24	0.97	0.37	0.42	0.007	0.001
Cu	Al	Nb	Ti	V			
0.04	0.043	0.002	0.001	0.005			

3.2.2 Carbide precipitation

Baker and Nutting in 1959 were the first to characterise precipitation reactions in $2\frac{1}{4}$Cr1Mo steel as a function of time, temperature and initial microstructure [80] with a later update provided by Nutting in 1998, Figure 3.1, [90]. Their work helped in the selection of heat treatments so that a number of combinations of carbides could

be generated to reveal their influence on hydrogen attack resistance.

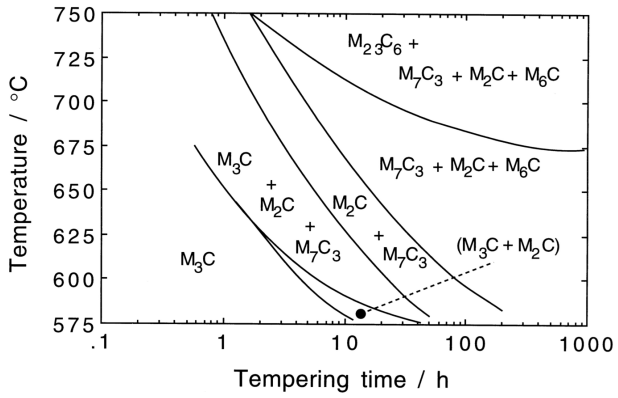

Figure 3.1: An updated version of the classic carbide stability diagram for a $2\frac{1}{4}$Cr-1Mo steel. After Nutting, [90].

There are five specimens, cubes with a side length of approximately 2.5 cm, tested in this work, all of which were austenitised for 2 h at 960 °C following Baker and Nutting [80, 90]. Two specimens are then quenched while the other three are air cooled. All specimens are tempered differently to obtain different carbides. All heat treatments with carbide types expected according to [90] are listed in Table 3.2.

Table 3.2: Heat treatments performed on different $2\frac{1}{4}$Cr-1Mo specimens. The last column represents the carbides expected according to Baker and Nutting [90].

Sample	Heat treatment	Carbides expected
A	Quench, temper @ 650°C, 50 h	$M_6C + M_2C + M_7C_3$
B	Quench, temper @ 700°C, 1 h	$M_3C + M_2C + M_7C_3$
C	Air-cool, temper @ 650°C, 50 h	$M_6C + M_2C + M_7C_3$
D	Air-cool, temper @ 700°C, 50 h	$M_{23}C_6 + M_6C + M_2C + M_7C_3$
E	Air-cool, temper @ 750°C, 5 h	$M_{23}C_6 + M_6C + M_2C + M_7C_3$

3.2.3 Characterisation prior to hydrogen exposure

- The volume fractions of voids and inclusions were measured using optical microscopy. The error bars were calculated by dividing the standard deviation by the square root of the number of measurements.

- The precipitation of carbides around any inclusions was investigated using imaging and electron-backscattered diffraction (EBSD) in ZEISS GeminiSEM 300 field emission gun scanning electron microscope at magnifications up to 3000× with a step size set at 0.03 µm. Specimens were ground gradually using silicon carbide (SiC) paper up to P2500, then polished with 6 µm and 1 µm diamond paste, with a final step of polishing with colloidal silica on a polishing cloth.

- Carbide precipitation after quenching and air cooling but before tempering was studied. This would indicate if factors other than tempering may contribute to the final carbide volume fractions. Energy dispersive X-ray analysis in a transmission electron microscope was used to identify the carbides.

- Synchrotron X-ray analysis was used, where the diffraction intensities can be sufficiently large to measure the relatively small fractions of carbide present in each of the specimens.

These results were to be compared against the equilibrium estimates described in Section 3.3.

3.2.4 Elevated temperature, pressurised hydrogen tests

According to the *Nelson curves* (Figure 1), the $2\frac{1}{4}$Cr-1Mo steel used is expected to be susceptible to attack if the temperature exceeds 450°C when the hydrogen partial pressure is higher than 13.7 MPa. As the temperature increases, the H_2 pressure needed to induce hydrogen attack decreases.

As mentioned on page 39, the equipment at TWI can achieve up to 525 °C and a hydrogen pressure of 10 MPa. Using *Nelson curves*, it can be seen that exposing the steel for a sufficient time in that environment would lead to hydrogen-attack damage.

The use of the high-temperature and pressure equipment is very expensive so it was important to design the experiments in an optimal manner. The time to

achieve hydrogen is designated as the "incubation period". The American Petroleum Standard (API 941) that contains the *Nelson curves*, also indicates incubation periods for C-0.5Mo that has a larger susceptibility to attack than the $2\frac{1}{4}$Cr-1Mo steel for which data are not available (Figure 3.2). The maximum parameters in the TWI autoclave would be needed for less than 100 h to induce the attack on C-0.5Mo steel, which was used as a minimum in order to fix the experiment duration.

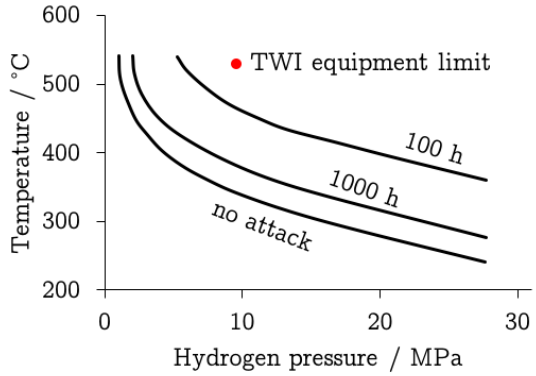

Figure 3.2: Incubation period for hydrogen attack on C-0.5Mo steel. The red circle represents the maximum parameters consistent with the TWI equipment.

Wanagel et al. [22] performed hydrogen charging experiments at high temperatures on $2\frac{1}{4}$Cr-1Mo steel. They found that after 20 days of hydrogen charging at 13.7 MPa at 600 °C, methane bubbles were detected using scanning electron microscopy. The period of 20 days was therefore used in the present work but unfortunately, the parameters of the TWI equipment are less severe than those implemented by Wanagel et al. The capability of the autoclave at TWI was used at its maximum, experiment was carried out for 500 h at 525°C with a hydrogen pressure of 10 MPa. It also is costly to use the facility so longer exposures could not be accommodated.

3.2.5 Characterisation of hydrogen-exposed specimens

After exposure, the specimens were examined to check if hydrogen attack had occurred. Comparisons to the results before hydrogen exposure would give clear evidence of damage evolution. The characterisation was carried out as follows:

- void/inclusion volume fractions by the use of optical microscopy.

- Synchrotron X-ray analysis to measure how the carbide volume fractions have changed following hydrogen exposure.

- EBSD to characterise carbide depletion in the vicinity of damage.

The results were used to investigate the effect of carbides and their equilibrium on hydrogen-attack resistance, the effect of microstructure and the effect of location on carbide depletion due to the attack.

3.3 Equilibrium calculations

Phase stability calculations using *ThermoCalc* (TCFE10 database) [91] were used to estimate equilibrium carbide volume fractions as well as the change in Gibbs free energy for the $\alpha' \rightarrow \alpha +$ carbide reactions, where α' refers to ferrite with the average composition of the alloy. It is appreciated that these represent thermodynamic equilibrium rather than kinetics but as will be seen later, they nevertheless can give useful information in interpreting complex observations.

In the first set of calculations using *ThermoCalc*, cementite, $M_{23}C_6$, M_7C_3, M_6C, M_2C were all allowed to exist alongside ferrite and austenite, in a Fe-C-Si-Cr-Mo-Ni-Mn system. Only $M_{23}C_6$ exists as the equilibrium carbide for the temperatures considered (Figure 3.3). Although the amount of $M_{23}C_6$ decreases as the temperature is increased, the differences for the variety of temperatures considered are not large given the exaggerated scale on the vertical axis of Figure 3.3. In a system constrained to two phases, in this case α+ $M_{23}C_6$, variations in phase fractions are determined entirely by changes in the chemical compositions of the phases as a function of temperature. Since the equilibrium concentration of carbon in ferrite is quite small at all temperatures, the fraction of carbide cannot change much with temperature.

It follows that during service, the steel should tend towards an equilibrium mixture of $M_{23}C_6$ and ferrite, although it is not of course known how long this might take. Figure 3.1 shows that 1000 h tempering at any of the temperatures considered

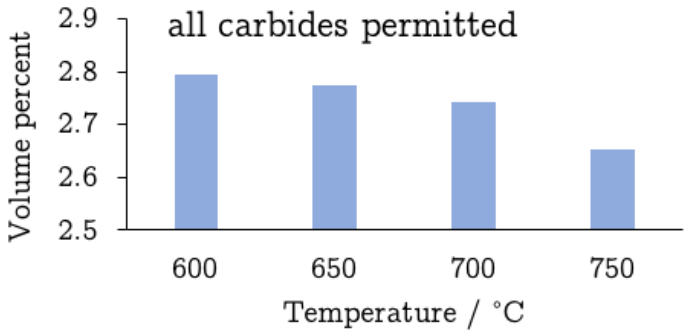

Figure 3.3: Equilibrium calculations for the alloy listed in Table 3.1. The residual phase is α.

would not lead to the equilibrium state. The actual microstructure observed during service, which usually is at temperatures of 600°C or less, should therefore consist of metastable carbides. This can in principle be studied by suppressing the equilibrium carbide in the thermodynamic calculations in order to reveal the sequence of less stable carbides.

Figure 3.4a shows the outcome when $M_{23}C_6$ is suppressed in the calculations; the most prominent carbide becomes M_7C_3 with M_6C as the minor carbide-phase, the volume fraction of which decreases dramatically as the temperature is increased. The mixture of $M_{23}C_6$+ M_7C_3 is somewhat consistent with the longest times plotted in Figure 3.1, although M_2C is absent in the thermodynamic calculations. Table 3.3 shows that M_6C is rich in molybdenum, which may explain the absence of M_2C. This is confirmed by the data in Figure 3.4b which shows that the suppression of M_6C promotes M_2C, which also indicates that the former has a greater stability. However, Figure 3.4c shows that M_6C is stable only in the presence of M_7C_3 so the molybdenum-rich phase then becomes M_2C; a part of the reason is that in the absence of the chromium-rich $M_{23}C_6$ + M_7C_3, the only carbide capable of absorbing chromium is cementite which has a low solubility for molybdenum, making the mixture of cementite and M_2C the most stable in the circumstances.

In summary, $M_{23}C_6$ is the equilibrium carbide which is most stable at all of the temperatures examined. Subsequent stability can be ranked, on the basis of the calculations presented above, as follows: $M_{23}C_6 \rightarrow$ $M_7C_3 \rightarrow$ $M_6C \rightarrow$ $M_2C \rightarrow$ cementite.

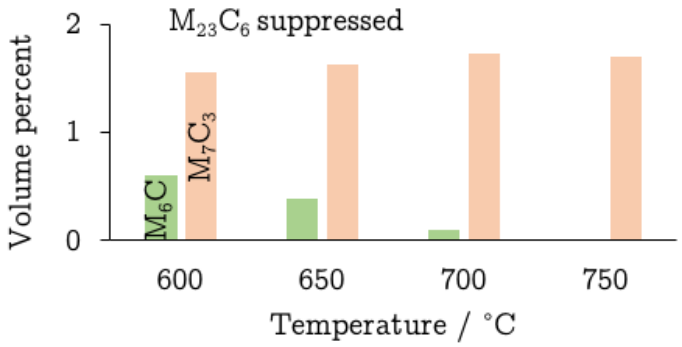

(a)

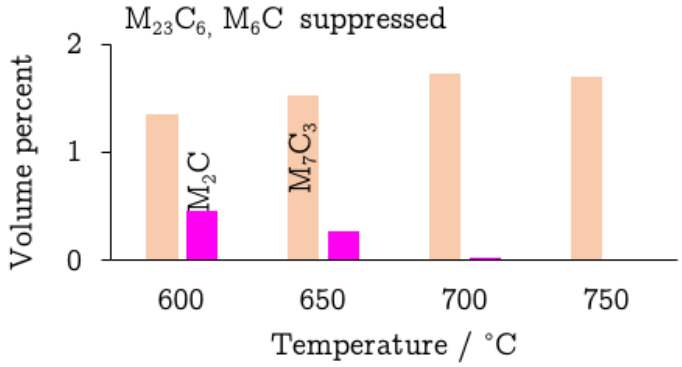

(b)

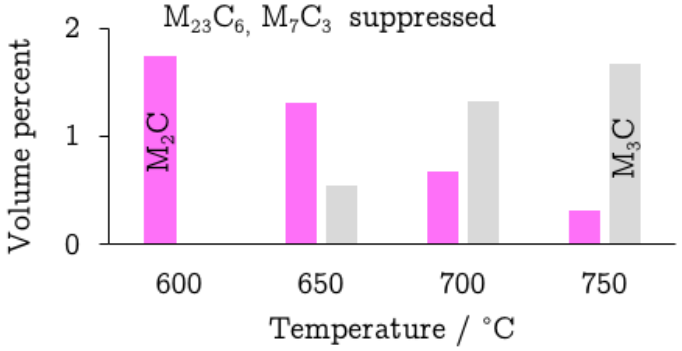

(c)

Figure 3.4: Equilibrium calculations, with a variety of constraints imposed, for the alloy listed in Table 3.1. The residual phase is α.

It is interesting, though not particularly useful from a practical point of view, to examine the relative stabilities of the carbides if they were to precipitate individually from supersaturated ferrite via the reaction $\alpha' \rightarrow \alpha + \text{carbide}$, using *ThermoCalc*. The results are illustrated in Figure 3.5. As expected from the equilibrium calculations where all carbides were allowed to exist in addition to ferrite,

Table 3.3: *ThermoCalc* prediction of equilibrium chemical composition (wt%) for carbides as a function of temperature for $2\frac{1}{4}$Cr-1Mo steel. The composition of $M_{23}C_6$ is when all carbides were permitted to exist but only $M_{23}C_6$ was predicted in association with α. Those of M_7C_3 and M_6C are for the case where $M_{23}C_6$ was suppressed. The compositions of M_2C and cementite represent the case where M_2C, cementite and M_6C were only allowed to exist.

	M_3C			M_2C			M_6C		
	650 °C	700 °C	750 °C	650 °C	700 °C	750 °C	650 °C	700 °C	750 °C
C	6.86	6.83	6.81	6.56	6.79	0.02	2.52	2.56	2.59
Cr	40.70	35.52	30.97	11.57	15.09	2.74	2.93	3.44	3.76
Mo	1.04	1.22	1.44	79.70	74.51	0.79	66.69	64.17	61.69
Fe	48.38	54.01	58.94	1.83	3.36	94.68	27.38	29.32	31.45
Mn	2.98	2.36	1.78	0.32	0.23	0.89	0.00	0.00	0.00
	M_7C_3			$M_{23}C_6$					
	650 °C	700 °C	750 °C	650 °C	700 °C	750 °C			
C	8.41	8.41	8.40	5.05	5.07	5.10			
Cr	54.32	50.90	47.17	37.87	34.31	30.69			
Mo	10.50	9.80	9.38	18.44	16.94	14.69			
Fe	24.33	28.79	33.32	38.14	43.12	48.91			
Mn	2.41	2.07	1.68	0.33	0.38	0.43			

$M_{23}C_6$ remains the most stable with the largest free energy change accompanying precipitation.

The discussion of other carbides in Figure 3.5 is fraught with difficulty since they would not in practice be expected to precipitate individually at the exclusion of all other carbides. Nevertheless, the direct precipitation of M_6C leads to the smallest reduction in free energy so it is not surprising that it always is associated with mixtures of carbides (Figure 3.1). Cementite is of course a metastable carbide when compared with the others and disappears completely on prolonged secondary hardening; nevertheless, there is a substantial free energy reduction when it precipitates

directly from supersaturated ferrite and because it has a huge kinetic advantage, it is able in practice to form during the early stages of tempering. The kinetic advantage referred to is that the initial formation of cementite during the tempering of martensite (or during the evolution of bainite) does not require the partitioning of substitutional solutes [75, 92].

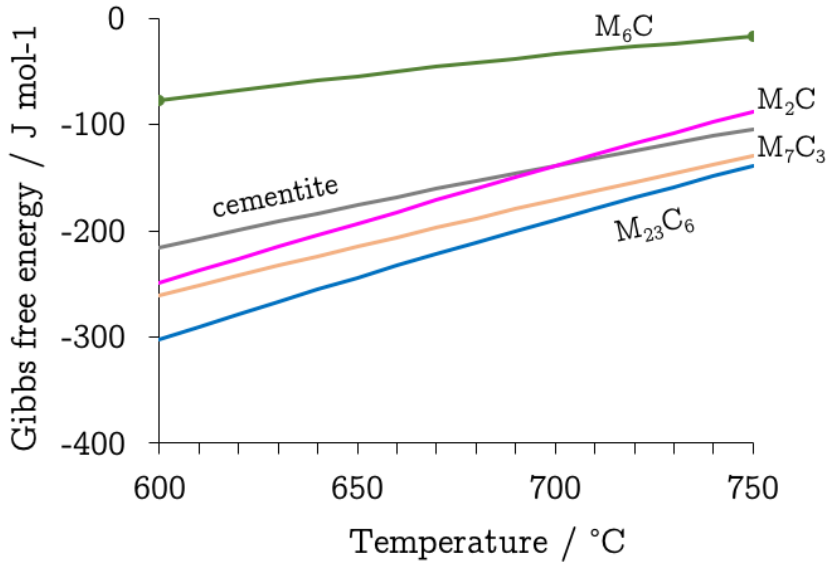

Figure 3.5: The change in Gibbs free energy from $\alpha' \rightarrow \alpha +$ carbide, as a function of temperature, for $2\frac{1}{4}$Cr-1Mo steel.

3.4 Results and discussion

3.4.1 Attack resistance relative to carbide type

As the carbide reacts with hydrogen, it leaves behind a void containing methane which can be detected and measured by the use of optical microscopy on unetched specimens. The images were then processed using *ImageJ* software to determine the volume fraction of voids.

In the initial state, the steel contains only non-metallic inclusions but no voids. The inclusion volume-fraction was measured prior to hydrogen-exposure as $V_V = 7.97 \times 10^{-5} \pm 9 \times 10^{-6}$. The reason for measuring the inclusion fraction is that it is possible sometimes for inclusions to fall out of the sample during metallographic preparation and leave an apparent void that is unrelated to the methane-containing voids generated by the reaction of hydrogen with carbides. The same method was used to characterise the *increase* in the measured volume fraction following hydrogen attack. The increase was then identified as voids introduced during hydrogen exposure. A summary of the results is listed in Table 3.4. Sample C has the highest V_V, which suggests that it underwent the highest hydrogen attack rate with an increase of two orders of magnitude after hydrogen exposure. This was followed by sample D, A+B in terms of descending V_V, with the least damage in sample E. Samples A, B, D and E had an increase in V_V by one order of magnitude in comparison to the state prior to exposure.

As described previously on page 49, the heat treatments were selected based on the work of Baker and Nutting [80, 90]. Figure 3.6 compares their findings with the data on the types of carbide observed, determined using synchrotron X-ray analysis for the steel used here. It is worth noting that there are slight differences in the nickel and chromium concentrations between the steel studied by Baker and Nutting (2.12Cr-0.17Ni wt%) and that used in the present work (2.24Cr-0.37Ni wt%).

Complete agreement between the literature and the results found by syn-

Table 3.4: Void/inclusion volume-fractions before and after hydrogen exposure. Q, AC and T refer to quenched, air-cooled and tempered respectively. The quantities for the exposed specimens include the void fraction from the unexposed state. The error bars were calculated by dividing the standard deviation by the square root of the number of measurements.

Sample	Void/inclusion volume-fraction
Unexposed	$8 \times 10^{-5} \pm 9 \times 10^{-6}$
Sample A (Q/T @ 650 °C for 50 h)	$47 \times 10^{-5} \pm 2 \times 10^{-5}$
Sample B (Q/T @ 700 °C for 1 h)	$46 \times 10^{-5} \pm 2 \times 10^{-5}$
Sample C (AC/T @ 650 °C for 50 h)	$120 \times 10^{-5} \pm 3 \times 10^{-5}$
Sample D (AC/T @ 700 °C for 50 h)	$52 \times 10^{-5} \pm 2 \times 10^{-5}$
Sample E (AC/T @ 750 °C for 5 h)	$33 \times 10^{-5} \pm 3 \times 10^{-5}$

chrotron X-rays analysis can only be seen for Sample A. It is speculated that discrepancies for other specimens might be because of the detailed difference in the heat treatment, for example the cooling rate during quenching or air cooling, which is affected by the size of the specimen. Also, the work of Baker and Nutting [80, 90] utilised transmission electron microscopy, which makes it possible to detect much smaller fractions of non-equilibrium carbides than using synchrotron X-rays. It can be argued that the work of Baker and Nutting, not intentionally, is a little misleading as it does not provide volume fractions of phases detected. Nevertheless, the purpose of using different heat treatments was to precipitate a variety of combinations of carbides in order to find their influence on hydrogen-attack resistance and that was achieved.

The carbide volume fractions before hydrogen-exposure can be found in Table 3.5 along with those expected from *ThermoCalc*. As explained previously (Figures 3.3, 3.4), calculated $M_{23}C_6$ values were obtained while allowing all carbides to exist, whereas M_7C_3 and M_6C values could only be estimated after suppressing $M_{23}C_6$. M_2C and cementite values were obtained similarly after suppressing $M_{23}C_6$

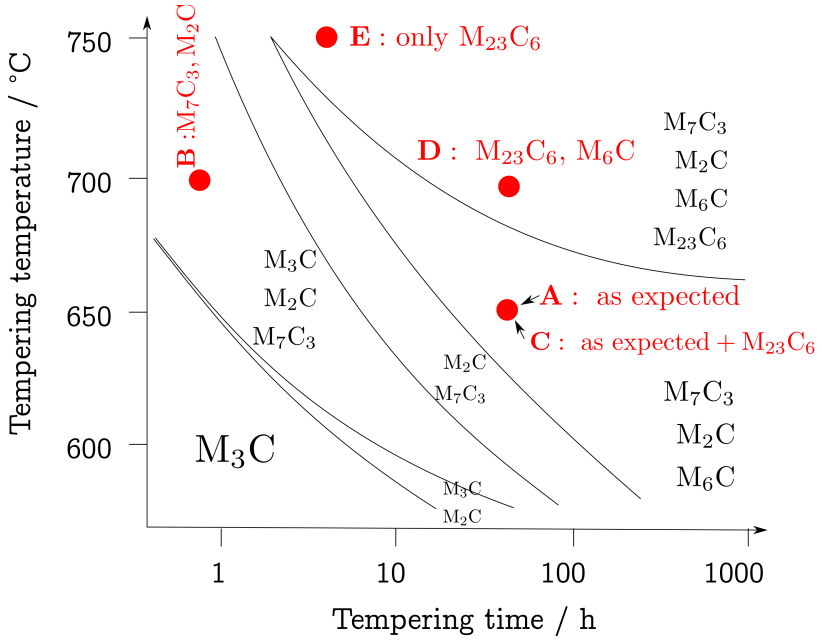

Figure 3.6: Carbides as expected from Baker and Nutting and as found here. In red are the current findings with samples represented by their designated letters (Table 3.4).

and M_7C_3.[1] Therefore, the comparison between the thermodynamic estimates and measured data are strictly only valid for Sample E which contained just $M_{23}C_6$; the agreement there is excellent. The same applies to the data for Sample D, where the volume fraction of M_6C is very small and the agreement between the thermodynamically calculated and actual fraction of $M_{23}C_6$ is consequently good. In contrast, Samples A-C show metastable microstructures so closure is not expected with the equilibrium calculation.

To reiterate, Table 3.5 shows that most of the carbides did not reach the expected equilibrium or constrained equilibrium volume fractions. The exceptions being $M_{23}C_6$ in samples D and E both of which at approximately the equilibrium volume fraction and the equilibrium composition. This is because those samples were tempered at the highest temperatures for the longest tempering periods. The volume fraction of M_6C in sample C is close to equilibrium, but in fact its chemical composition is not, therefore it cannot be regarded as having reached equilibrium.

[1]When some phases are suppressed in order to discover metastable carbides, the results are described henceforth using the term *constrained equilibrium*.

Table 3.5: Volume fraction of carbides as expected under equilibrium or constrained equilibrium conditions using *ThermoCalc* (T.C.) and as determined using synchrotron X-ray diffraction for the heat-treated specimens.

	Sample A		Sample B		Sample C	
	Q/T @ 650 °C for 50 h		Q/T @ 700 °C for 1 h		AC/T @ 650 °C for 50 h	
	T.C.	Rietveld	T.C.	Rietveld	T.C.	Rietveld
M_3C	–	–	–	–	–	–
M_6C	0.0037	0.0022 ± 0.0003	–	–	0.0037	0.0031 ± 0.0005
M_2C	0.0131	0.0026 ± 0.0001	0.0067	0.0039 ± 0.0001	0.0131	0.0010 ± 0.0001
M_7C_3	0.0154	0.0087 ± 0.0006	0.0172	0.0071 ± 0.0006	0.0152	0.0048 ± 0.0007
$M_{23}C_6$	–	–	–	–	0.0276	0.0113 ± 0.0008
	Sample D		Sample E			
	AC/T @ 700 °C for 50 h		AC/T @ 750 °C for 5 h			
	T.C.	Rietveld	T.C.	Rietveld		
M_3C	–	–	–	–		
M_6C	0.0008	0.0055 ± 0.0006	–	–		
M_2C	–	–	–	–		
M_7C_3	–	–	–	–		
$M_{23}C_6$	0.02718	0.0271 ± 0.0008	0.02636	0.0263 ± 0.0008		

The increase in void volume-fraction following hydrogen exposure (Table 3.4) might correlate with the reduction of carbide volume fractions. To investigate how the carbides resisted hydrogen attack, synchrotron X-ray analysis was carried out on the hydrogen-exposed specimens.

3.4.2 Hydrogen-attack resistance of carbides

The hydrogen-exposed specimens were examined using synchrotron X-ray to compare the carbide volume-fractions before and after hydrogen-exposure. This would help identifying which carbides have depleted and were susceptible to the hydrogen attack. A representation of how the analysis was carried out on the specimens can be seen in Figure 3.7. Measurements were carried out horizontally from surface to surface with a distance of 0.5 mm between each measurement point in the same row. After the whole sample has been examined, all values in the same position are averaged to give one spectrum for that position. For example, all measured points in the first position are averaged to give one spectrum, which is then analysed using Reitveld analysis to calculate carbide fractions at that position. The first position is designated AE(1) in the listings of experimental data that follow. The first and last positions are also the nearest to the hydrogen-exposed surface.

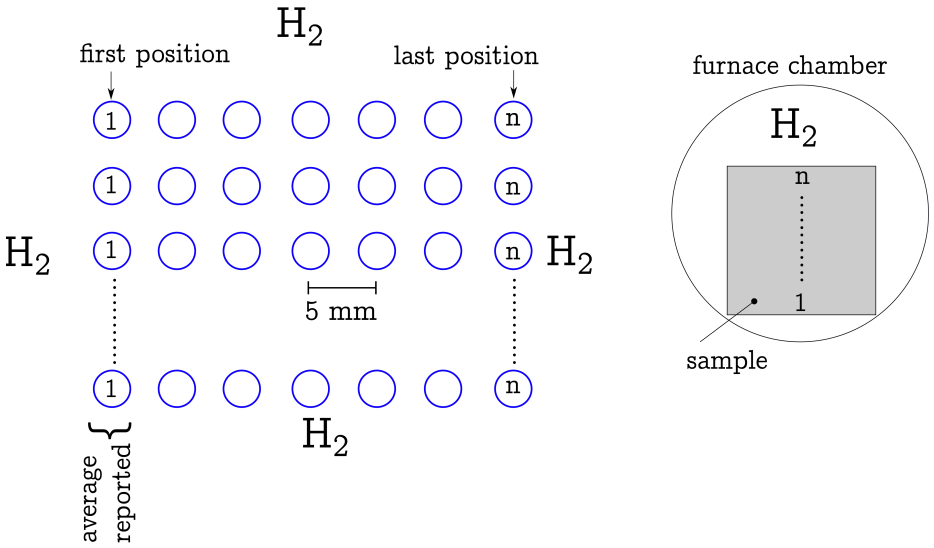

Figure 3.7: A representation of how measurements are taken with synchrotron X-ray for hydrogen-exposed specimens. The sketch on the right shows how the square-sectioned sample was placed within the furnace holder illustrated in Figure 2.1. As a result, position 1 has less access to hydrogen than position n. The positions shown correspond to those listed in, for example, Table 3.6.

According to the data in Table 3.4, Samples A and B were the 2nd least

damaged specimens in terms of the reduction in carbide volume fractions. As can be seen from Tables 3.6-3.7 and Figures 3.8-3.9, there is no noticeable reduction in carbides except for one position for M_7C_3 in sample B. M_2C and M_6C showed good resistance to reaction with hydrogen as their fractions remained stable, explaining the good resistance of those two specimens.

Table 3.6: Synchrotron-measured carbide volume-fractions for Sample A, quenched then tempered at 650 °C for 50 h.

	M_6C	M_7C_3	M_2C		M_6C	M_7C_3	M_2C
Unexposed	0.0022 ± 0.0003	0.0087 ± 0.0006	0.0026 ± 0.0001				
AE (1)	0.0025 ± 0.0006	0.0077 ± 0.0013	0.0025 ± 0.0003	AE (6)	0.0028 ± 0.0006	0.0088 ± 0.0008	0.0026 ± 0.0002
AE (2)	0.0028 ± 0.0005	0.0081 ± 0.0011	0.0025 ± 0.0002	AE (7)	0.003 ± 0.0007	0.0084 ± 0.001	0.0026 ± 0.0002
AE (3)	0.0029 ± 0.0005	0.0084 ± 0.0009	0.0026 ± 0.0002	AE (8)	0.0029 ± 0.0006	0.0076 ± 0.001	0.0025 ± 0.0002
AE (4)	0.0029 ± 0.0004	0.0084 ± 0.0009	0.0026 ± 0.0002	AE (9)	0.003 ± 0.0006	0.0081 ± 0.0011	0.0025 ± 0.0002
AE (5)	0.0028 ± 0.0005	0.0092 ± 0.0009	0.0027 ± 0.0001	AE (10)	0.0032 ± 0.0009	0.0101 ± 0.0011	0.0025 ± 0.0003

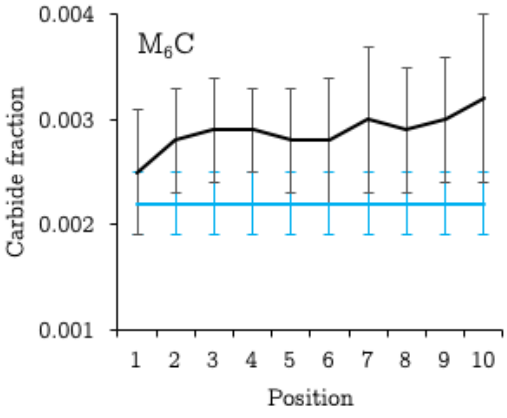

(a)

Figure 3.8: Sample A. The fractions prior to exposure are represented by the blue lines. First and last positions represent the closest proximity to the exposed surface.

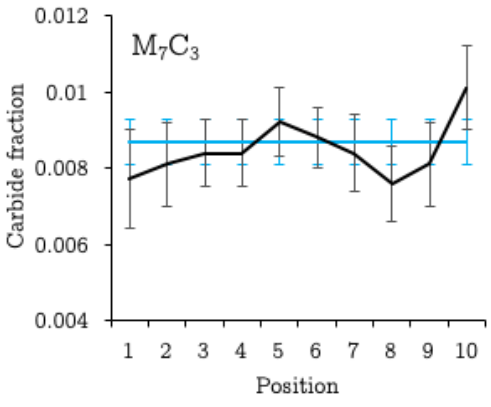

(b)

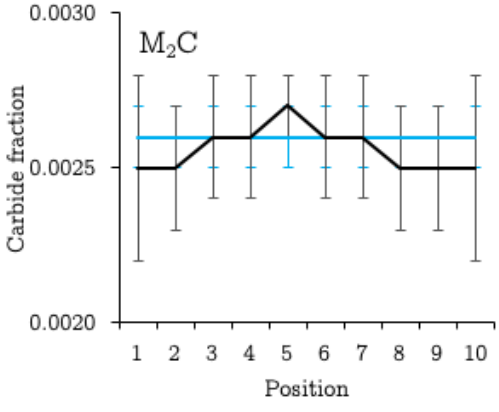

(c)

Table 3.7: Synchrotron-measured carbide volume-fractions for Sample B, quenched then tempered at 700 °C for 1 h.

	M_7C_3	M_2C		M_7C_3	M_2C
Before exposure	0.0071 ± 0.0006	0.0039 ± 0.0001			
AE (1)	0.0052 ± 0.0007	0.005 ± 0.0002	AE (7)	0.0065 ± 0.0007	0.006 ± 0.0002
AE (2)	0.0078 ± 0.0009	0.0057 ± 0.0002	AE (8)	0.0061 ± 0.0007	0.0058 ± 0.0002
AE (3)	0.0077 ± 0.0006	0.0054 ± 0.0001	AE (9)	0.0062 ± 0.0007	0.0055 ± 0.0002
AE (4)	0.0068 ± 0.0006	0.0057 ± 0.0002	AE (10)	0.006 ± 0.0007	0.0058 ± 0.0002
AE (5)	0.0065 ± 0.0006	0.0058 ± 0.0001	AE (11)	0.0063 ± 0.0007	0.0057 ± 0.0002
AE (6)	0.0065 ± 0.0006	0.0056 ± 0.0002	AE (12)	0.0071 ± 0.0007	0.0058 ± 0.0002

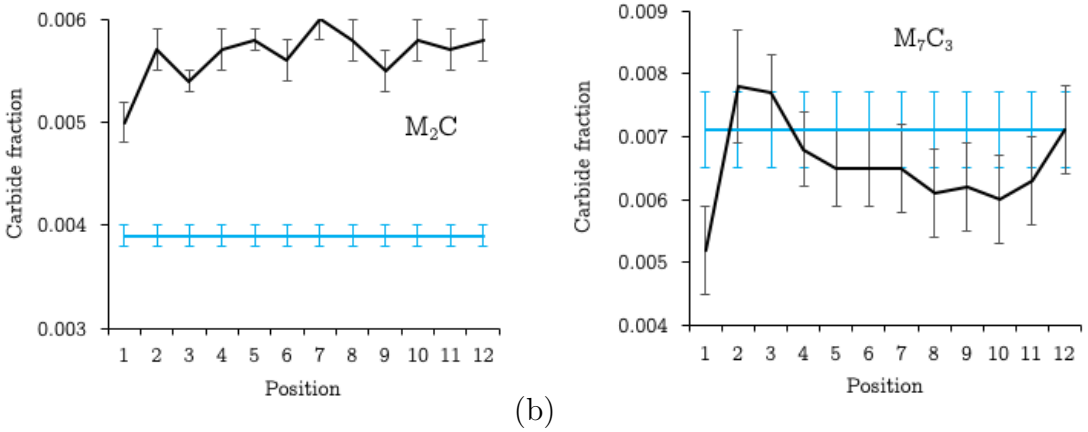

(a) (b)

Figure 3.9: Sample B. The fractions prior to exposure are represented by the blue lines. First and last positions represent the closest proximity to the exposed surface.

Sample C exhibited the least resistance to hydrogen attack. The void volume-fraction increased by two orders of magnitude relative to the unexposed specimen. Table 3.8 and Figure 3.10 show that the reduction was greatest for $M_{23}C_6$ with its volume fraction reduced from 0.0113 ± 0.0008 in the unexposed specimen to as low as 0.0051 ± 0.0005 in one of the positions in the exposed specimen, a reduction of 0.0062. Figure 3.10 shows that M_7C_3 also decreased from 0.0048 ± 0.0007 in the unexposed specimen to 0.0021 ± 0.0006 at one of the positions in the exposed specimen. M_2C and M_6C fractions remained eventually unchanged.

Table 3.8: Synchrotron-measured carbide volume-fractions for Sample C, air-cooled then tempered at 650 °C for 50 h.

	M_6C	M_7C_3	M_2C	$M_{23}C_6$
Unexposed	0.0031 ± 0.0005	0.0048 ± 0.0007	0.0010 ± 0.0001	0.0113 ± 0.0008
AE (1)	0.0031 ± 0.0006	0.0033 ± 0.0007	0.0011 ± 0.0002	0.0099 ± 0.0008
AE (2)	0.0031 ± 0.0004	0.0035 ± 0.0006	0.0011 ± 0.0001	0.0114 ± 0.0005
AE (3)	0.0031 ± 0.0008	0.0047 ± 0.0009	0.0011 ± 0.0002	0.0111 ± 0.0008
AE (4)	0.0034 ± 0.0011	0.0052 ± 0.001	0.0011 ± 0.0002	0.0118 ± 0.0009
AE (5)	0.004 ± 0.0006	0.0044 ± 0.0008	0.0011 ± 0.0002	0.0116 ± 0.0007
AE (6)	0.0032 ± 0.0006	0.0036 ± 0.001	0.0011 ± 0.0002	0.0113 ± 0.0008
AE (7)	0.0031 ± 0.0003	0.0026 ± 0.0005	0.0011 ± 0.0001	0.0108 ± 0.0004
AE (8)	0.0035 ± 0.0004	0.0029 ± 0.0006	0.0011 ± 0.0001	0.0109 ± 0.0005
AE (9)	0.0036 ± 0.0005	0.0033 ± 0.0006	0.0012 ± 0.0001	0.0107 ± 0.0005
AE (10)	0.0032 ± 0.0003	0.003 ± 0.0005	0.0012 ± 0.0001	0.0104 ± 0.0004
AE (11)	0.0032 ± 0.0003	0.0028 ± 0.0005	0.0011 ± 0.0001	0.0103 ± 0.0004
AE (12)	0.0034 ± 0.0004	0.0029 ± 0.0006	0.0012 ± 0.0001	0.0114 ± 0.0005
AE (13)	0.0038 ± 0.0006	0.0021 ± 0.0006	0.0011 ± 0.0002	0.0099 ± 0.0007
AE (14)	0.0035 ± 0.0004	0.0022 ± 0.0005	0.0012 ± 0.0001	0.0082 ± 0.0005
AE (15)	0.0035 ± 0.0005	0.0029 ± 0.0008	0.0009 ± 0.0001	0.0051 ± 0.0005

M_6C also resisted attack in Sample D as can be seen in Table 3.9 and Figure 3.11. The increase in V_V is caused by the reduction of $M_{23}C_6$, which was reduced by 0.0056, a similar reduction to that observed in sample C. This specimen was ranked 2nd in terms of susceptibility to hydrogen attack.

The smallest increase in V_V was observed in sample E, which contained only $M_{23}C_6$. As can be seen in Table 3.10 and Figure 3.12, there is no noticeable reduction in $M_{23}C_6$ content. The high tempering temperature (750 °C) influences the composition of $M_{23}C_6$ making it closer to its equilibrium composition. This explains the excellent hydrogen-attack resistance in this specimen.

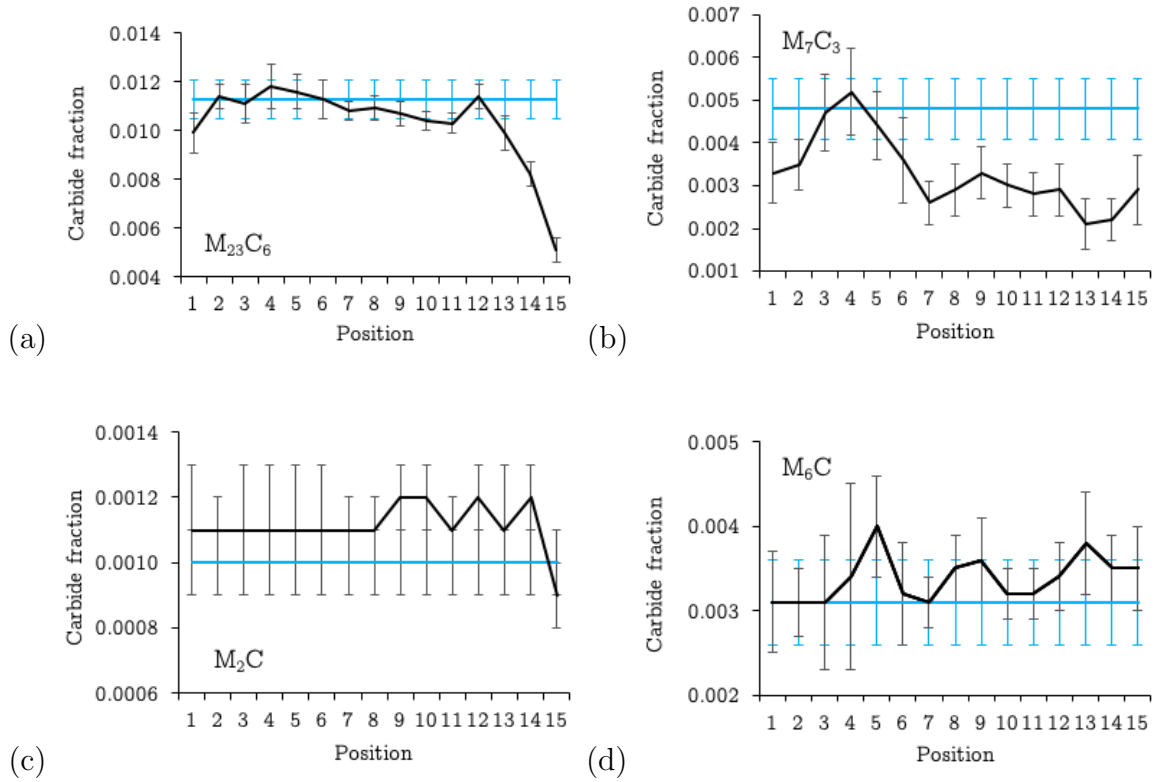

Figure 3.10: Sample C. The fractions prior to exposure are represented by the blue lines. First and last positions represent the closest proximity to the exposed surface.

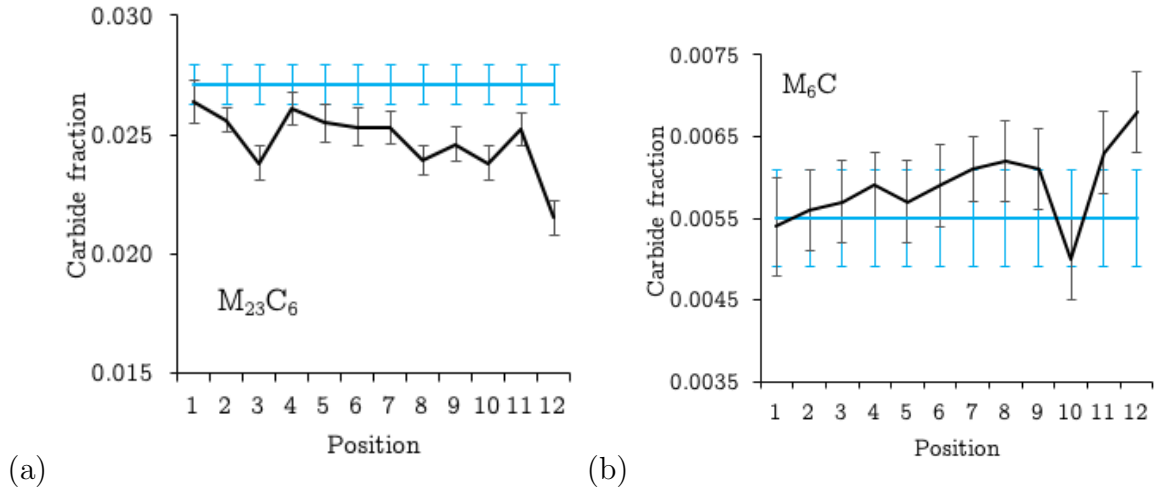

Figure 3.11: Sample D. The fractions prior to exposure are represented by the blue lines. First and last positions represent the closest proximity to the exposed surface.

Table 3.9: Synchrotron measured carbide volume-fractions for Sample D, air-cooled then tempered at 700 °C for 50 h.

	M_6C	$M_{23}C_6$		M_6C	$M_{23}C_6$
Before exposure	0.0055 ± 0.0006	0.0271 ± 0.0008			
AE (1)	0.0054 ± 0.0006	0.0264 ± 0.0009	AE (7)	0.0061 ± 0.0004	0.0253 ± 0.0007
AE (2)	0.0056 ± 0.0005	0.0256 ± 0.0005	AE (8)	0.0062 ± 0.0005	0.0239 ± 0.0006
AE (3)	0.0057 ± 0.0005	0.0238 ± 0.0007	AE (9)	0.0061 ± 0.0005	0.0246 ± 0.0007
AE (4)	0.0059 ± 0.0004	0.0261 ± 0.0007	AE (10)	0.005 ± 0.0005	0.0238 ± 0.0007
AE (5)	0.0057 ± 0.0005	0.0255 ± 0.0008	AE (11)	0.0063 ± 0.0005	0.0252 ± 0.0007
AE (6)	0.0059 ± 0.0005	0.0253 ± 0.0008	AE (12)	0.0068 ± 0.0005	0.0215 ± 0.0007

Table 3.10: Synchrotron-measured carbide volume-fractions for Sample E, air cooled then tempered at 750 °C for 5 h.

	$M_{23}C_6$		$M_{23}C_6$
Unexposed	0.0263 ± 0.0008		
AE (1)	0.0332 ± 0.0027		
AE (2)	0.0311 ± 0.0015	AE (6)	0.0318 ± 0.0024
AE (3)	0.0302 ± 0.0014	AE (7)	0.0304 ± 0.0023
AE (4)	0.0305 ± 0.0015	AE (8)	0.0312 ± 0.0021
AE (5)	0.0322 ± 0.002	AE (9)	0.0317 ± 0.0017

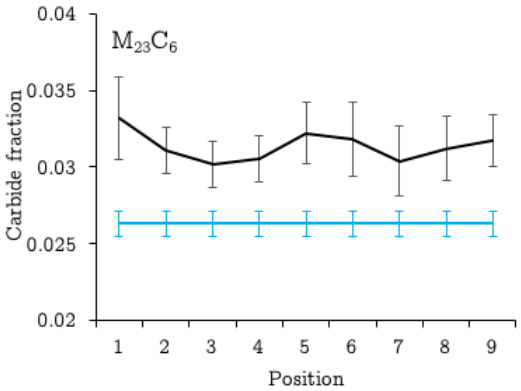

Figure 3.12: Sample E. The fraction prior to exposure is represented by the blue line. First and last positions represent the closest proximity to the exposed surface.

In summary, Mo-enriched carbides, M_2C and M_6C, seem to resist attack under all the conditions studied more than Cr-enriched carbides, where resistance was more dependent on the tempering extent. This disagreed with findings of the modelling work of Schlogl et al. on page 28, where Cr-rich carbides were concluded to have lower carbon activity than Mo-rich carbides, hence better hydrogen attack resistance.

However, M_7C_3 and $M_{23}C_6$ resistance varied between samples. Therefore, hydrogen attack resistance cannot be decided on the basis of the carbide type alone. It may depend on other factors such as heat treatment, i.e. quenched or normalised, and tempering temperature and duration. As mentioned on page 44, M_7C_3 in $2\frac{1}{4}$Cr-1Mo steel is considered a transient carbide as it does not get the chance to reach the equilibrium composition before being replaced by $M_{23}C_6$, which explains its depletion. In order to investigate Cr-carbides further, the behaviour of $M_{23}C_6$ was examined as it showed low and high hydrogen attack resistance in Specimens C and E respectively, which will be discussed in Section 3.4.3.

In one of the specimens, the carbide volume fraction increased after hydrogen exposure at 525 °C, which suggests that the precipitation process during tempering was incomplete. If a specimen is significantly heat-treated so that the microstructure is close to equilibrium, then there should not be an increase in volume fraction upon the hydrogen exposure, this was the case in samples A, C, D and E. However, if the tempering conditions are short and at low temperatures then, further precipitation during hydrogen exposure might occur, which was the case in the specimen tempered for the shortest period (1 h), sample B. The tempering parameter in Equation 1.6 can be used to quantify the extent of tempering in these specimens. Table 3.11 shows the tempering parameters for each of the specimens. As the tempering parameter increases, the precipitation is close to completion and the specimen is considered closer to its equilibrium.

The data in Table 3.11 suggest that Sample B is the furthest from equilibrium so the precipitation process in this sample can be considered to be the least complete out of the five specimens. This can be supported by the observation in

Table 3.11: Tempering parameter calculated for all specimens based on Equation 1.6.

Sample	Heat treatment	Tempering parameter / 10^3
A	Q/T @ 650 °C for 50 h	20.03
B	Q/T @ 700 °C for 1 h	19.46
C	AC/T @ 650 °C for 50 h	20.03
D	AC/T @ 700 °C for 50 h	21.11
E	AC/T @ 750 °C for 5 h	21.17

Figure 3.9a where M_2C volume fraction in sample B has increased significantly after hydrogen exposure at 525 °C because the tempering conditions for sample B were inadequate to reach equilibrium. This can be supported by recalling Table 3.5, where M_2C and M_7C_3 volume fractions in Sample B were far from equilibrium.

However, the increase in volume fraction is only observed in M_2C (Figure 3.9a) but not M_7C_3 (Figure 3.9b). This might be due to the difference in the resistance of both carbides to depletion by hydrogen. M_7C_3 decreases upon hydrogen exposure as can be seen from the first position in Figure 13b however, it can be hypothesised that M_7C_3 is also precipitated further upon hydrogen exposure as it starts off a volume fraction much less than equilibrium. Therefore, there is a balance between the increase in M_7C_3 and its depletion by hydrogen attack as it is less stable than M_2C.

3.4.3 Effect of deviation from equilibrium

$M_{23}C_6$ showed poor hydrogen attack resistance in Samples C and D as it depleted by about 0.006 of its original volume fractions, while the hydrogen-attack resistance of $M_{23}C_6$ was very good in sample E. Samples C and D were tempered for 50 h at 650 °C and 700 °C respectively, while sample E was tempered at 750 °C for 5 h. Therefore, the hydrogen attack resistance of $M_{23}C_6$ increased as the tempering temperature increased. In terms of equilibrium, looking at *ThermoCalc* calculations for the expected volume fractions in Figures 3.3,3.4, it was clear that $M_{23}C_6$ should be the only carbide present at equilibrium at all tempering temperatures. This suggests that only sample E was at equilibrium as it only contained $M_{23}C_6$.

To investigate the $M_{23}C_6$ hydrogen attack resistance in this work, the chemical composition of $M_{23}C_6$ was calculated at equilibrium using *ThermoCalc* and measured experimentally using EDX in TEM. The results can be found in Table 3.12.

Let us recall the work of Parathasarathy and Shewmon [23] in Section 1.2.4, in which they concluded that a high chromium content in the matrix indicates a low iron content, hence a reduced carbon activity, which leads to a higher hydrogen attack resistance. As can be seen from Table 3.12, the Fe and Cr concentrations are not close to equilibrium when tempering at 650 °C to 700 °C, because the measured Cr concentrations should be much larger. This is consistent with a large carbon activity of $M_{23}C_6$ at 650 °C and 700 °C (than at 750 °C), making the carbides more reactive at the lower temperatures. This explains the difference in hydrogen attack behaviour of $M_{23}C_6$ at different tempering temperatures. Therefore, if equilibrium conditions for $M_{23}C_6$ are reached for low tempering temperatures (650 °C), the carbon activity would be minimised, thereby decreasing the tendency to react with hydrogen and form methane. But unfortunately, the tempering times required would be impractical as literature has shown that not even 500 h at 700 °C would ensure equilibrium conditions [23]. It is interesting to mention that equilibrium Cr concentrations decrease with increasing tempering temperature, as seen in Table 3.12, suggesting that Cr will be higher in the matrix at higher tempering temperatures, which decreases

the carbon activity as discovered by Parathasarathy and Shewmon [23].

Table 3.12: Equilibrium and measured chemical composition (wt%) of $M_{23}C_6$ at different tempering temperatures. *ThermoCalc* (T.C.) is used to calculate the equilibrium composition. EDX in TEM was used to measure the actual chemical composition (EDX values). As carbon content cannot be measured using EDX, all the carbon content values are calculated by *ThermoCalc* and EDX measurements for other elements were corrected accordingly.

	Sample C AC/T @ 650 °C for 50 h		Sample D AC/T @ 700 °C for 50 h		Sample E AC/T @ 750 °C for 5 h	
	T.C.	EDX	T.C.	EDX	T.C.	EDX
C	5.052	–	5.071	–	5.107	–
Cr	37.877	15.61 ± 0.20	34.317	16.01 ± 0.13	30.691	27.43 ± 0.05
Mo	18.448	6.62 ± 0.13	16.943	3.93 ± 0.07	14.692	4.90 ± 0.03
Fe	38.146	70.04 ± 0.42	43.129	71.79 ± 0.26	48.916	58.33 ± 0.07
Mn	0.332	2.68 ± 0.10	0.385	3.19 ± 0.05	0.435	4.23 ± 0.02

3.4.4 Relating hydrogen attack resistance to microstructure

The heat treatments shown in Table 3.2 introduce two microstructures, martensitic microstructure for quenched specimens (A and B) and bainitic microstructure for air cooled specimens (C, D and E). This section is focused on how air cooling or quenching may have influenced carbide precipitation and therefore influenced hydrogen attack resistance.

Sample A and C were both tempered at 650 °C for 50 h. Sample A was quenched before tempering while sample C was air cooled. Therefore, the difference between those two specimens is not a consequence of the tempering but due to the cooling method following austentisation.

Sample C has clearly shown less hydrogen attack resistance than sample A (Table 3.4), however, it cannot be stated that quenched specimens would have a higher hydrogen attack resistance than air-cooled specimens. This is because sample E, an air-cooled specimen, had the highest hydrogen attack resistance of all specimens. Therefore, the influence of the microstructure might be on the equilibrium phases more than a direct influence on the hydrogen attack resistance.

The carbides expected in both specimens are M_7C_3, M_6C and M_2C. However, synchrotron X-ray analysis indicated that $M_{23}C_6$ was precipitated in sample C along with the expected carbides, while sample A contained only the expected carbides. If Figures 3.3,3.4 are recalled, $M_{23}C_6$ is the expected equilibrium carbide in this steel at all tempering temperatures, therefore the precipitation of $M_{23}C_6$ is an indication that the system is closer to equilibrium. It can reasonably be concluded that sample C, air-cooled, is closer to equilibrium than sample A, quenched. This might be because of precipitation occurring during the air-cooling stage, which was investigated using EDX in TEM on air-cooled and quenched specimens. Therefore, the microstructure itself may not influence hydrogen attack resistance, but the heat treatment should. Scanning transmission electron microscopy images revealed that as-quenched specimen appears to have more precipitation than as air-cooled specimen. The precipitation in the latter, though, being coarser. Further EDX analysis

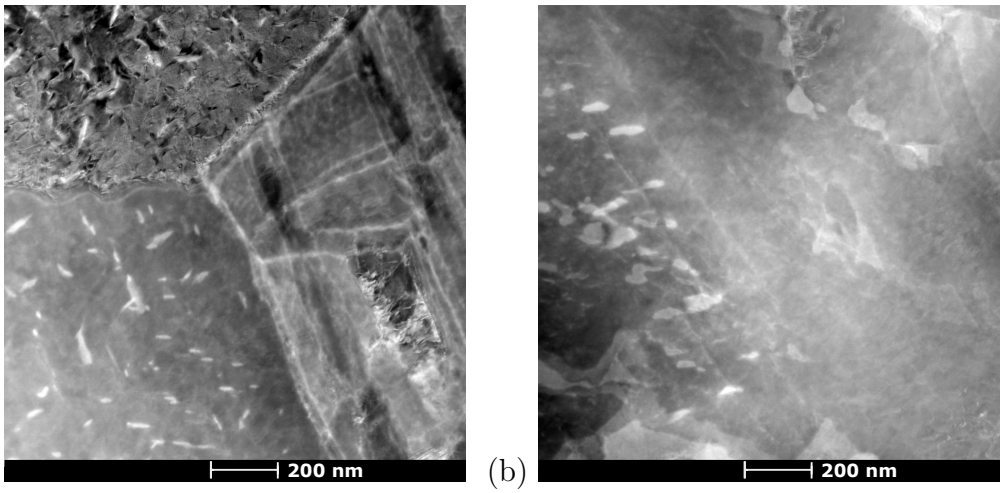

Figure 3.13: STEM micrographs for $2\frac{1}{4}$Cr-1Mo steel after a) quenching, b) air-cooling.

revealed that the carbides in the as air-cooled specimen contains chromium up to 2.48 ± 0.51 wt%, while most carbides in the as-quenched specimen hardly contained any alloying-elements, with little containing chromium of around 0.71 ± 0.15 wt%. This information indicates that precipitates after air-cooling are richer in alloying elements, which make them closer to equilibrium state than those in the as-quenched specimens. Therefore, the same tempering conditions, 650 °C for 50 h, resulted in the precipitation of the thermodynamically equilibrium carbide, $M_{23}C_6$, in the air-cooled specimen but not the quenched one.

3.4.5 Relating hydrogen attack resistance to carbide location

The purpose of work reported in this section was to investigate if the attack is favoured to occur closer to surfaces as the hydrogen diffuses in. Also, if the attack is more likely to deplete carbides around inclusions or if depletion follows a random behaviour.

Electron backscatter diffraction (EBSD) technique was used to examine the depletion locations. EBSD was carried out around inclusions on specimens before and after hydrogen exposure.

In the unexposed specimen, it was seen that carbide precipitation occurs similarly around an inclusion to the rest of the steel bulk (Figure 3.14a), therefore

if noticeable depletion occurs around inclusions, then it would be a consequence of hydrogen attack. After hydrogen-exposure, it was seen in sample C, which has the highest increase in void volume-fraction, that the depletion of carbides occurred heavily around inclusions (Figure 3.14b). The depletion in the other specimens was not as clear, though some depletion could be seen around inclusions, Figures 3.15a and 3.15b. Figure 3.15a (Sample A) shows depletion mainly at the top of the inclusion, which may suggest that this is the direction in which the hydrogen in travelling from; in fact, that was the direction in which the surface is the closest. Sample E was also examined using EBSD (Figure 3.16) and the examination did not show any noticeable depletion around inclusions, which agrees with the carbide volume-fraction findings of synchrotron X-ray analysis.

These findings suggest that inclusions may be attractive sites for hydrogen to reside and accumulate, therefore carbides around inclusions are more likely to deplete before carbides across the bulk. There is considerable research in conventional hydrogen embrittlement to show hydrogen migrating and becoming trapped at inclusions, as was seen in Figure 1.18 on page 29 [40, 93–95].

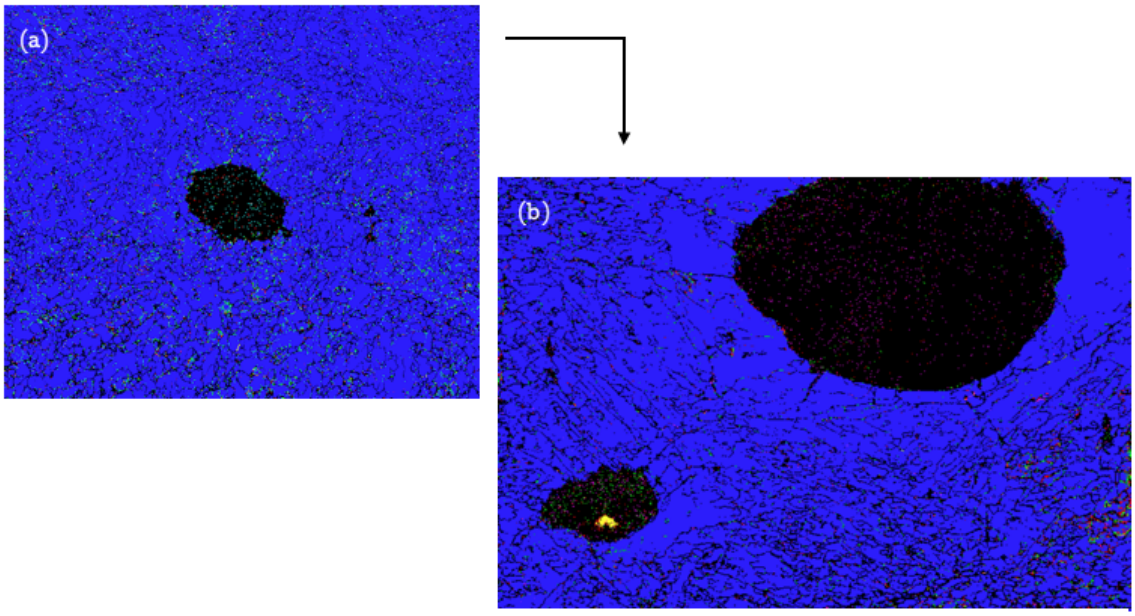

Figure 3.14: EBSD images around inclusions in (a) an unexposed specimen, uniform carbide precipitation can be seen across the image. (b) an exposed specimen (Sample C), carbide depletion can be clearly seen around the inclusions.

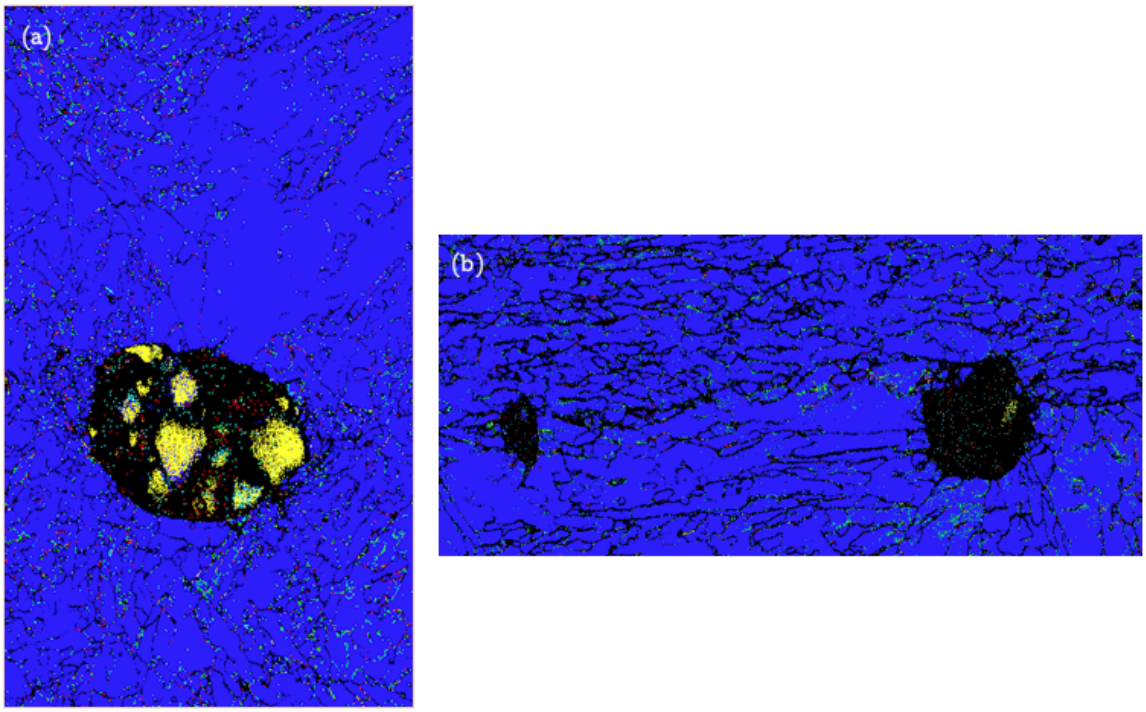

Figure 3.15: EBSD images around inclusions in an exposed specimen (a) Sample A, carbide depletion can be seen to the top of inclusion. The top direction is the closest to surface. (b) Sample B, carbide depletion can be clearly seen between the inclusions.

The use of the synchrotron X-ray analysis results may help in determining if carbides closer to surfaces are more likely to deplete before carbides further from the surface. This may suggest that there is a depletion gradient throughout the specimen. If Figure 2.1 is recalled, specimens are placed within tubes. Figure 3.7 represents how each of specimens is positioned within the tube. The specimen positioning suggests that the access to constant high hydrogen pressures is less to the bottom of the specimen than other areas, which could introduce a difference in carbide depletion amounts. From Figures 3.10a, 3.10b and 3.11a, it can be seen that when carbides were depleted, the depletion occurred heavily to one end of the specimen. Those heavily depleted regions correspond to the top end of the specimens in Figure 3.7, where access to hydrogen pressure is continuously higher. Therefore, carbides closer to surfaces are more likely to deplete faster than carbides further from the surface.

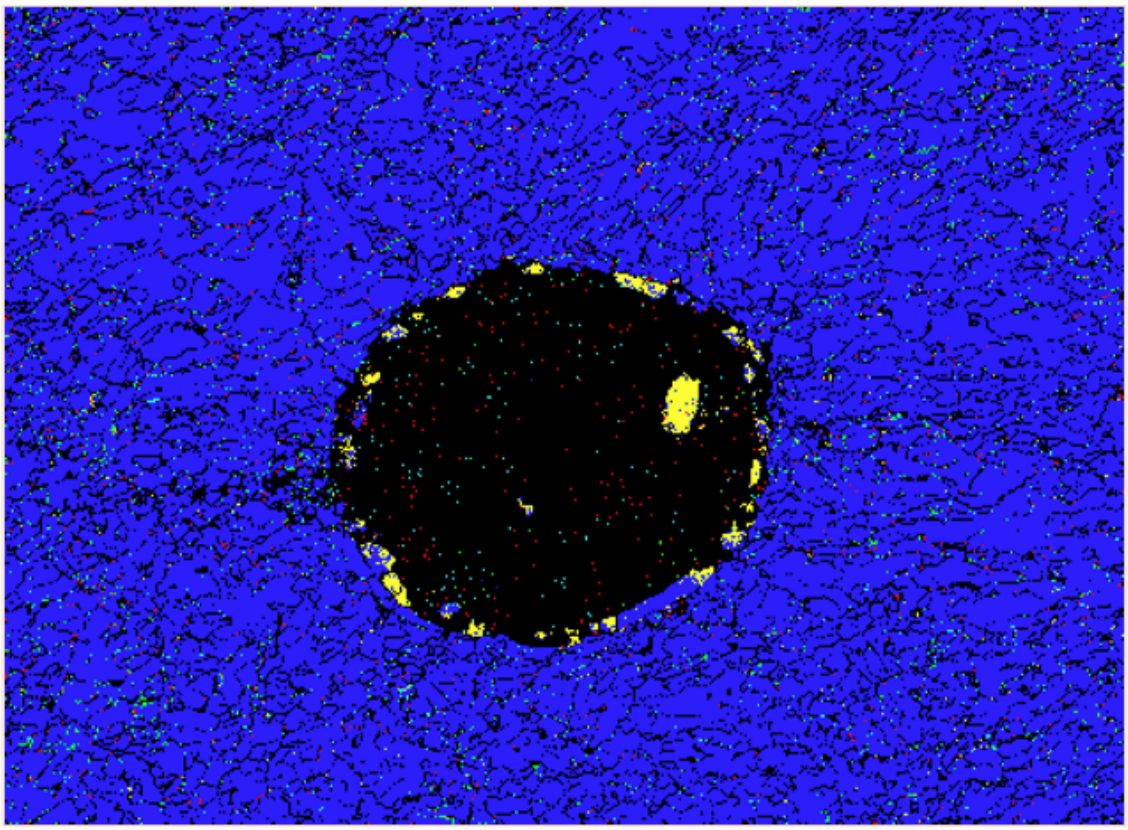

Figure 3.16: EBSD image around an inclusion in an exposed specimen (Sample E), no noticeable depletion can be seen around the inclusion. This specimen had the lowest increase in voids after hydrogen exposure.

3.5 Conclusions on hydrogen attack resistance of commercially-used steels

- Hydrogen attack resistance of carbides is dependent on the deviation of alloying-elements content of the carbide relative to equilibrium, which in turn influences the carbon activity in the matrix. Carbon activity is dependent on ratios and concentrations of alloying elements in the carbides. In $2\frac{1}{4}$Cr-1Mo steel, the alloying elements are Cr and Mo. The higher concentration of Mo and Cr in M_2C and M_6C might be responsible for the low carbon activity and therefore good hydrogen attack resistance of M_2C and M_6C was observed.

- Carbon activity in the matrix is increased if the Cr concentration is decreased. The best possible combination of high Cr and low Fe concentrations in the matrix is expected thermodynamically to be at high tempering temperature, i.e. 750°C, which was proven by the superior resistance in sample E which was tempered for 5 h at 750°C, resulting in a better Fe/Cr ratio to lower carbon activity sufficiently to resist hydrogen attack.

- If tempering is inadequate for a specimen to reach equilibrium, then carbide precipitation could occur upon hydrogen exposure at high temperatures, as observed in M_2C in sample B. In that case, precipitation and depletion could also occur simultaneously depending on the carbide resistance to hydrogen attack, as was observed in M_7C_3 in the same specimen.

- When quenched and air-cooled specimens where tempered at the same temperature for the same duration, it was seen that air-cooled specimens were closer to equilibrium than quenched specimens as they precipitated the equilibrium carbide, $M_{23}C_6$. But that did not guarantee hydrogen attack resistance as equilibrium states were still far.

- Carbides close to inclusions have been depleted more than carbides scattered across the steel. Also, carbides closer to the surface have depleted ahead of carbides further from the surface.

Chapter 4

Mitigation solutions

4.1 Introduction

Having identified the carbon activity in the carbides as a main drive for their reaction with hydrogen, the aim of the work presented in this chapter was to investigate hydrogen attack mitigation methods that are expected to minimise the carbon activity and hence, offer better hydrogen-attack resistance.

Different precipitation mechanisms can offer new solutions where carbon activity is minimised, such as during interphase precipitation, which can result in regular arrays of stable alloy-carbides that strengthen the steel. The alloying element used for this work was vanadium, which is expected to form thermodynamically more stable carbides when embedded in ferrite, than the other solutes present in $2\frac{1}{4}$Cr-1Mo steel. While interphase-precipitated steels offer more stable carbides, they have never been exploited in petrochemical applications.

Another possible solution investigated is HT10 steel, where the only precipitated carbides are enriched with chromium, molybdenum and vanadium. This steel also has shown excellent resistance to electrolytically charged hydrogen damage at low temperatures with the additional quality of excellent hydrogen trapping in comparison with $2\frac{1}{4}$Cr-1Mo steel [67, 96].

The characterisation work described in this Chapter follows similar procedures to the procedures described in Section 3.2. However, the focus here was to utilise heat treatments that only precipitate carbides expected to be thermodynamically stable. The characterisation is therefore focused on how the carbides behave in hydrogen attack-inducing environments and how they deviate from the equilibrium state in terms of their volume fractions and chemical compositions.

This is achieved by comparing metallurgical aspects before and after hydrogen exposure. The work consisted of four stages:

- the first was to carry out a variety of heat treatments to precipitate carbides with different volume fractions and varying alloying-element contents. Another factor was considered in vanadium steel, which involved varying the expected carbide size and sheet spacing in order to examine the effect on hydrogen attack resistance. Phase diagram calculations were used to estimate the equilibrium volume fractions at each tempering temperature for comparison against experimental data.

- The second stage involved the characterisation of the steels after the variety of heat treatments, including measurement of void/inclusion volume-fractions using optical microscopy and synchrotron X-ray analysis to measure carbide volume fractions after each heat treatment.

- The samples were then exposed to the same environment that induced hydrogen attack in $2\frac{1}{4}$Cr-1Mo steel. This is to discover whether the suggested solutions mitigate hydrogen attack.

- The final stage involved the characterisation of the steels after hydrogen exposure and comparison of results with unexposed samples, as well as comparisons with $2\frac{1}{4}$Cr-1Mo steel. This included optical microscopy for void volume-fraction changes and synchrotron X-ray diffraction for measuring carbide volume fractions.

4.1.1 Interphase precipitation

The work that has been done on $2\frac{1}{4}$Cr-1Mo steel is an example of how alloying elements influence the carbide precipitation sequence and stability upon the tempering of martensite, which means that alloy carbides replace cementite and less-stable carbides, as the tempering temperature and duration increase. In contrast, interphase precipitation means that the alloy carbides are precipitated upon the decomposition of γ to α in an overlapping temperature range when compared with conventional tempering. Alloy-carbide precipitation during conventional tempering is reported to occur at temperatures as low as 500°C [16] and can reach up to 750°C as seen in Section 3.2.2, while interphase precipitation has been reported to occur as low as 600°C in Ti-V-Mo steel [97]. The advantage of interphase precipitation is that alloy carbides are formed from the very beginnings rather than cementite, which is then replaced by alloy carbides [16, 52]. Therefore, the use of interphase precipitation mechanism in order to precipitate only stable carbides, without the need of lengthy heat treatment durations, may offer a suitable solution to mitigate high temperature hydrogen attack.

According to Figure 1, vanadium additions increase the hydrogen attack resistance of $2\frac{1}{4}$Cr-1Mo steel. Vanadium is known also to introduce interphase precipitation, if the appropriate heat treatments are followed [53, 98]. Therefore, the hydrogen attack resistance of interphase-precipitation in steels containing only vanadium as an alloying element has been investigated. Honeycombe and Batte studied interphase precipitation in vanadium steels with varying carbon and vanadium concentrations. They found that the highest vanadium carbide volume fraction, 0.0123, was detected in a 0.2C-1.04V steel (wt%). The latter composition is also stoichiometric, meaning that the equilibrium products would be only ferrite and vanadium carbide, which is favourable for this project's case, as mentioned on page 34, as it should eliminate unnecessary carbon activity by tying up all carbon in stable vanadium carbides. Thus, 0.2C-1.04V steel was manufactured and examined in this project. It should be noted that the steel composition in Honeycombe and Batte work included a small fraction of niobium to control the austenite grain size. However, this is unnecessary at this

stage of the work, so niobium was not added to the tested steel [53].

4.1.2 Alloying-elements enriched carbides

One of the findings described in Chapter 3 was that the carbon activity in carbides decreases as the concentration of alloying elements increases. M_6C and M_2C carbides showed better resistance to hydrogen attack than M_7C_3 and $M_{23}C_6$ due to their high Cr and Mo contents.

HT10 steel has been designed to be used in the oil and gas industry. It has been utilised mainly for its hydrogen embrittlement resistance at low temperatures due to its excellent hydrogen trapping capacity, which is caused by the precipitation of Cr-Mo-V enriched carbides. As HT10 steel contains only alloy-enriched carbides after tempering at 600°C for at least 1 h, then it should be expected to offer better hydrogen attack resistance than previously tested $2\frac{1}{4}$Cr-1Mo steel as it eliminates the precipitation of non alloy-enriched carbides.

It is emphasised also that the hydrogen trapping ability has not been exploited before in the field of high-temperature high-pressure hydrogen attack mitigation. HT10 steel has shown excellent hydrogen trapping capacity at low temperatures [67]. However, the role, if any, of hydrogen trapping capacity is unknown for high temperature environments. Therefore, the influence of hydrogen trapping on hydrogen attack resistance was investigated in this work.

Precipitating alloy-enriched carbides using conventional heat treatment is expected to show better hydrogen attack resistance than $2\frac{1}{4}$Cr-1Mo steel. However, there is still a possibility that not all the carbides reach the equilibrium state, leading to increased carbon activity and hydrogen attack susceptibility. Therefore, the experiments included isothermal transformation of HT10 steel in order to precipitate carbides directly after austenitisation similar to interphase precipitation in vanadium steel. It should be noted that due to the high hardenability of HT10, long durations are needed for the complete transformation from austenite to ferrite at the isothermal

temperature, which may influence the equilibrium state of the precipitated carbides. Nonetheless, it was believed that the precipitated carbides will be alloy-enriched offering better resistance to hydrogen attack due to the introduction of vanadium in this steel.

4.2 Experimental procedure

4.2.1 Heat treatments

Vanadium steel The factor that most influences the carbide dispersion in 0.2C-1.04V steel is the isothermal transformation temperature. Figure 1.20 shows the relationship between steel composition, transformation temperature and the carbide dispersion. As the carbon and vanadium contents increase, the carbide dispersion becomes finer, and for the same composition, lower transformation temperatures introduce finer dispersions [53].

With the use of the dilatometer, the steel specimens were austenitised at 1200°C for 15 min to ensure that all vanadium carbides are dissolved. Then, the temperature was dropped to the desired transformation temperature and kept there for 5 min to allow carbide precipitation, before quenching to room temperature. The transformation temperatures were 725°C, 775°C and 825°C. The carbide dispersion is expected to vary between the specimens, which would allow the investigation of the possible influence of carbide dispersion on hydrogen attack resistance.

HT10 steel M_2C and MC are the alloy carbides formed in HT10 steel, where M represents Mo, V and Cr. The chemical composition of HT10 can be found in Table 4.1. As reported in literature and in Chapter 3, the factors that influence carbide precipitation in conventional tempering are the tempering temperature and duration.

Ramjaun et al. have studied hydrogen trapping behaviour in HT10 steel

Table 4.1: Chemical composition (wt%) of HT10 steel.

C	Mn	Cr	V	Mo	Ni	Ti	N
0.10	0.21	2.4	0.4	1.5	2.8	0.003	0.0029

tempered in the range of 575-650°C. They found that the hydrogen trapping capacity decreases as the tempering temperature increases. This is because hydrogen trapping is enhanced by the coherency strain fields around the alloy carbides. However, as the tempering temperature and duration increase, the coherency is lost due to the coarsening of carbides. They concluded that tempering at 575°C for 11 h results in the highest trapping capacity [67]. Ooi et al. studied the carbide precipitation sequence in HT10 steel, they found that MC carbide precipitates upon austenisation while M_2C precipitates on the expense of MC carbides at around 600°C [99].

One of the findings described in Chapter 3 on $2\frac{1}{4}$Cr-1Mo was that increasing the tempering temperature results in precipitating carbides that are closer to their equilibrium state, which ultimately increases the resistance to hydrogen attack.

By combining the above observations from the literature and the ones from the work reported in previous chapters, HT10 was austenitised at 850°C then quenched and tempered for 11 h at temperatures ranging from 575-650°C. The duration of 11 h tempering is expected to produce a maximum trapping capacity at 575°C decreasing to a minimum at 650°C. Simultaneously, the carbides are expected to be closer to their equilibrium as the tempering temperature increases. Therefore, it should be possible to study the influence of hydrogen trapping capacity as well as carbide deviation from equilibrium on hydrogen attack resistance of HT10 steel. Figure 4.1 illustrates how hydrogen trapping capacity and the carbide precipitation vary depending on the tempering temperature for the suggested heat treatments. Expected carbide volume fractions will be presented in the following section.

HT10 steel was also transformed isothermally to investigate the possibility of inducing interphase precipitation. HT10's microstructure commonly consists of tempered martensite that is strengthened by carbide precipitation. The transforma-

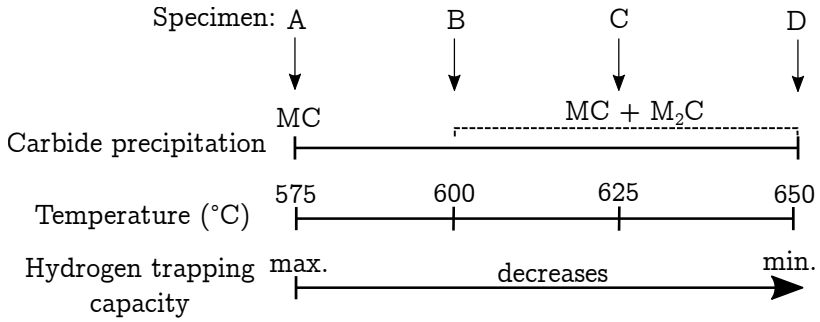

Figure 4.1: The influence of the tempering temperature on the hydrogen trapping capacity and carbide precipitation sequence in HT10 steel. Tempering duration is 11 h. Data from [67, 99].

tion from austenite to martensite occurs in HT10 even at slow cooling rates due to its high hardenability. However, if the steel is austenitised and then transformed isothermally in the ferrite formation temperature range for enough time, then ferrite is formed along with the precipitation of stable carbides. Isothermal transformation of HT10 has not been exploited in the literature. However, isothermal transformation of other high-hardenability steels has been studied, such as the work by Moon et al. on 9Cr-1Mo-0.1C steel. They concluded that ferrite can be formed in high-hardenability steels using isothermal transformation for prolonged durations. The ferrite transformation was completed after 48 h when the austenite grain size was around 49 µm. However, if it is as large as 1083 µm, the ferrite transformation is completed after 120 h. This is because the number-density of grain boundary nucleation sites increases with decreasing austenite grain size. Thus, a finer grain size would increase the rate at which ferrite nucleates, but it will not influence the growth rate of ferrite, which is generally controlled by volume diffusion [29].

With the help of a dilatometer, HT10 steel was austenitised at 850°C, the temperature was then dropped to 650°C, where ferrite is expected to form, and held there for 48 h and 72 h in two separate experiments. The duration of 48 h did not complete the ferrite transformation, which terminated at around 70 h. Therefore, different HT10 specimens were transformed isothermally at 625°C, 650°C and 675°C for 72 h to investigate the possibility of interphase precipitation in HT10 steel and its effect on hydrogen attack resistance.

4.2.2 Elevated-temperature high hydrogen-pressure testing

In order to compare the results described in this section to the $2\frac{1}{4}$Cr-1Mo steel results, identical hydrogen exposure conditions were maintained. Therefore, the vanadium steel and HT10 specimens were exposed to hydrogen at 525°C for 500 h at the TWI facility. The specimens were placed within three large cylinders of 316L stainless steel (Figure 2.1), which was then placed at the centre of a tube furnace (Figure 2.2). A total of 16 specimens were exposed to hydrogen as follows:

- Four HT10 specimens that were quenched and tempered for 11 h at 575°C, 600°C, 625°C, 650°C.
- Six HT10 dilatometry specimens that were transformed isothermally at 625°C, 650°C, 675°C for 72 h, i.e. two specimens at each temperature to offer more material for later characterisation. The specimens heat-treated at the same temperature were placed next to each other.
- Six vanadium steel dilatometry specimens that were transformed isothermally at 725°C, 775°C, 825°C for 5 min, i.e. two specimens at each temperature. The specimens heat-treated at the same temperature were placed next to each other.

4.2.3 Characterisation techniques

Vanadium steel and HT10 steel were both characterised before and after hydrogen exposure. The characterisation was similar to $2\frac{1}{4}$Cr-1Mo steel characterisation in the previous section. It included the analysis of the following parameters:

- volume fraction of voids and inclusions, measured using *ImageJ* on micrographs taken by optical microscopy to show if any increase in void content occurred after hydrogen exposure, which would be an initial indication of the resistance to hydrogen attack.

- Synchrotron X-ray analysis was used to quantify the carbide volume-fractions before and after the exposure, which helps identifying if any specific carbide depletion has occurred due to hydrogen attack.

- Scanning electron microscopy and transmission electron microscopy were both used for microstructural analysis; the latter was used specifically to confirm the fine interphase precipitation in vanadium steel. Energy dispersive X-ray analysis was used to measure the chemical composition of the carbides.

These results were then compared to the findings from Chapter 3 on $2\frac{1}{4}$Cr-1Mo steel to determine whether the suggested solutions have improved the resistance to hydrogen attack.

4.3 Equilibrium calculations

ThermoCalc (TCFE10 database) was used to estimate equilibrium carbide volume-fractions as well as their equilibrium compositions at different transformation temperatures. It should be mentioned again that these represent thermodynamic equilibrium rather than kinetics but can nevertheless give useful information. This information was used to compare with experimental measurements to elaborate on the influence of deviation from equilibrium on hydrogen attack resistance.

Vanadium steel The only carbides expected to precipitate in this steel are vanadium carbides. In the calculations using *ThermoCalc*, in a Fe-C-V system, MC was allowed to exist alongside ferrite and austenite. The MC volume fraction decreases slightly as the transformation temperature increases, Figure 4.2. However, the differences for the temperatures considered are not large given the exaggerated scale on the vertical axis. In a system constrained to two phases existing simultaneously, in this case α + MC, variations in phase fractions are determined entirely by changes in the chemical composition of the phases as a function of temperature. Since

the equilibrium concentration of carbon in ferrite is quite small at all temperatures, the fraction of carbide cannot change much with temperature.

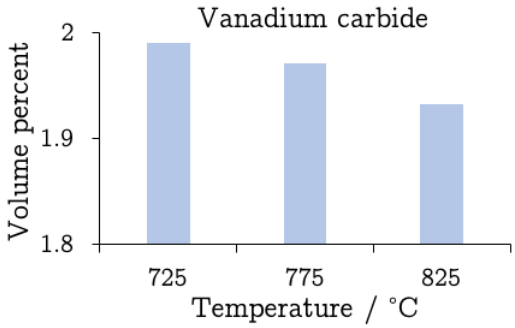

Figure 4.2: Equilibrium calculations of the volume fraction of vanadium carbide at different transformation temperatures. The residual phase is α.

The composition of vanadium carbide at the transformation temperatures is listed in Table 4.2. It can be seen that the change in composition is slight at the different transformation temperatures. The small change in volume fractions and compositions between the transformation temperatures could suggest that the transformation temperature will mainly influence the interphase-precipitation sheet spacing and carbide size, as mentioned on page 31.

Table 4.2: *ThermoCalc* prediction of equilibrium chemical compositions (wt%) for vanadium carbides at different transformation temperatures in vanadium steel.

Element	725°C	775°C	825°C
C	16.68	16.72	16.75
Fe	6.38	6.48	6.47
V	76.93	76.79	76.78

HT10 steel *ThermoCalc* estimations were carried out in a Fe-C-Mn-Cr-V-Mo-Ni-Ti system, where MC, M_6C, M_2C were all allowed to exist alongside ferrite and austenite. As mentioned on page 84, M_2C carbides are expected to precipitate on the expense of MC carbides as the tempering temperature increases, which suggests that the steel is closer to equilibrium when M_2C is detected. This has been supported by *ThermoCalc* as M_2C is the only expected carbide at equilibrium, Figure 4.3a. Previous research on HT10 [67, 99] did not report the precipitation of M_6C, however,

if M_2C precipitation is suppressed, M_6C is the only prominent carbide expected. The composition of M_6C is similar to that of M_2C apart from the vanadium and iron weight percentages, Table 4.3.

In the last set of *ThermoCalc* calculations, M_6C and M_2C are both suppressed, allowing MC carbide to precipitate with its carbide volume fraction increasing up to 600 °C and then decrease as the tempering temperature increases, , Figure 4.3c, which agrees with the findings of Ooi et al. [99].

In summary, M_2C is the equilibrium carbide which is most stable at all of the temperatures examined. Subsequent stability can be ranked, on the basis of the calculations presented above, as follows: $M_2C \rightarrow M_6C \rightarrow MC$.

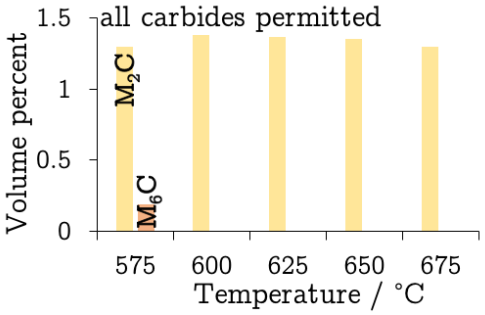

(a)

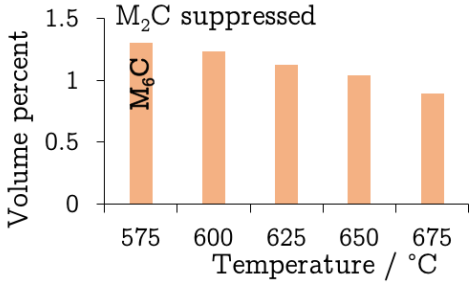

(b)

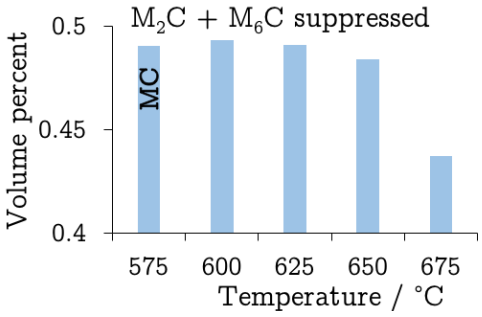

(c)

Figure 4.3: Equilibrium calculations, with a variety of constraints imposed, for the HT10 steel with the composition listed in Table 4.1. The residual phase is α.

Table 4.3: *ThermoCalc* prediction of equilibrium chemical compositions (wt%) for M_2C, M_6C and MC carbides at different tempering temperatures in HT10 steel. M_6C composition was obtained by suppressing the formation of M_2C, while MC composition was obtained by suppressing the formation of the former two carbides.

	M_2C					M_6C				
Element	575°C	600°C	625°C	650°C	675°C	575°C	600°C	625°C	650°C	675°C
C	7.16	7.18	7.21	7.24	7.27	2.51	2.52	2.52	2.53	2.54
V	20.31	20.31	20.29	20.24	20.03	2.38	2.22	1.98	1.82	1.65
Mo	68.27	67.77	66.97	66.45	65.91	66.68	66.33	65.74	65.32	64.64
Fe	0.10	0.15	0.26	0.36	0.57	24.69	25.06	25.71	26.20	27.00
Cr	4.10	4.48	5.15	5.59	6.12	3.72	3.85	4.01	4.09	4.14
	MC									
Element	575°C	600°C	625°C	650°C	675°C					
C	14.17	14.18	14.19	14.19	14.19					
V	35.21	35.19	35.11	35.04	34.89					
Mo	50.60	50.62	50.69	50.75	50.91					

4.4 Results and discussion

4.4.1 Improved hydrogen-attack resistance

Before embarking onto the analysis of hydrogen-attack resistance for the different suggested mitigation methods, transmission electron microscopy was used to prove that interphase precipitation has occurred in vanadium steel. Figure 4.4a shows very fine interphase precipitation in the ferritic region of the specimen, while unexpected martensitic regions were observed, probably due to unfinished transformation and will be discussed later in detail. It should be noted that prior austenite grain boundaries contain heavy precipitation in this condition. Grain boundaries are regions of high internal energy, which make them preferred sites for precipitation, which explains why grain boundaries are associated with exaggerated precipitation, as seen in Figure 4.4a. The same behaviour is observed at lower transformation temperatures, Figure 4.5, though to a lesser extent presumably because of the slower precipitation kinetics. Interphase precipitation occurs at the moving γ/α interface, and the scale of the microstructure decreases with decreasing transformation temperature because of the accompanying reduction in diffusion distances. This can be supported by the observations in Figures 4.4a, Figure 4.5, where grain boundaries had heavier precipitation at 825 °C, which reduced at 775 °C and even further at 725 °C. This precipitation depletes the solute in the adjacent vicinity introducing precipitate-free zones around them, as can be seen clearly in Figure 4.5a in the vicinity of the grain boundaries.

Interphase precipitation was not seen at lower transformation temperatures than at 825 °C, i.e. rows of precipitates. Considering that γ to α transformation was completed at 725 °C and 775 °C but not at 825 °C, Figure 4.6, therefore the precipitation observed at the lower transformation temperatures can be assumed to be interphase precipitation, but it was not possible to observe it in rows due to a faulty TEM specimen holder which hindered tilting the specimen enough to find the zone axis and observe interphase precipitation. Time limitations prevented further work.

(a) 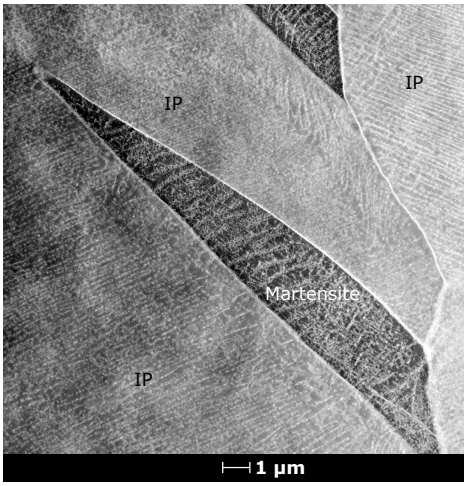

(b) 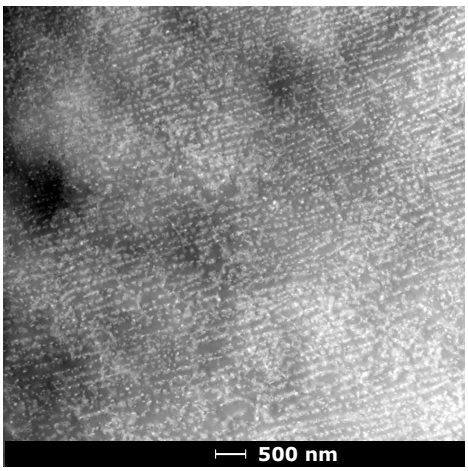

Figure 4.4: a) TEM dark field image for vanadium steel transformed isothermally at 825°C for 5 min showing ferritic regions with interphase precipitates in rows. b) A magnified dark field image of interphase precipitation in the same specimen.

(a) 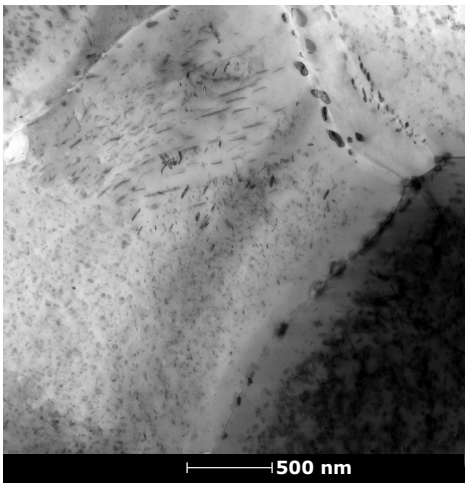

(b) 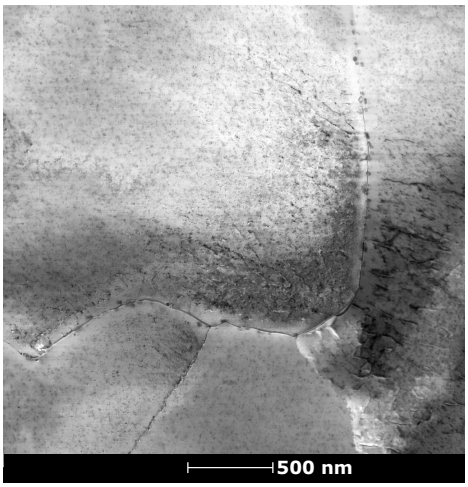

Figure 4.5: TEM bright field images for vanadium steel transformed isothermally at a) 775°C for 5 min, b) 725°C for 5 min. Precipitates at grain boundaries are larger at higher transformation temperatures. Precipitate-free zones can be seen around grain boundaries.

Now that interphase precipitation has occurred in the tested specimens, investigations on their hydrogen attack resistance can be carried out. As can be seen in Table 3.4, the void volume-fractions (V_V) have increased after hydrogen exposure of $2\frac{1}{4}$Cr-1Mo specimens by at least 25×10^{-5}. V_V was measured for vanadium and HT10 steels before and after hydrogen exposure using optical microscopy and *ImageJ*. As can be seen from Table 4.4, the void volume-fraction has increased across vanadium steel specimens by 5×10^{-5} to 21×10^{-5}, and in HT10 steel by 1×10^{-5} to 16×10^{-5}, while in $2\frac{1}{4}$Cr-1Mo, the void volume-fraction has increased by 25×10^{-5} to 112×10^{-5}. These results clearly show the superior hydrogen attack resistance in both suggested mitigation methods to the commercially-used steel for hydrogen attack application, $2\frac{1}{4}$Cr-1Mo.

Table 4.4: Void/inclusion volume-fractions before and after hydrogen exposure for vanadium steel and HT10. The quantities for the exposed specimens include the voids fraction from the unexposed state. IT refers to isothermal transformation, which was for 5 min and 72 h for vanadium steel and HT10 respectively. While QT refers to quenched and tempered, where all tempering durations were 11 h. The error bars were calculated by dividing the standard deviation by the square root of the number of measurements.

Sample	V_V	Sample	V_V
Vanadium steel		HT10	
Unexposed	$11 \times 10^{-6} \pm 2 \times 10^{-6}$	Unexposed	$14 \times 10^{-5} \pm 1 \times 10^{-5}$
ITa (725°C)	$19 \times 10^{-6} \pm 3 \times 10^{-6}$	ITa (625°C)	$21 \times 10^{-5} \pm 2 \times 10^{-5}$
ITb (775°C)	$16 \times 10^{-6} \pm 5 \times 10^{-6}$	ITb (650°C)	$28 \times 10^{-5} \pm 3 \times 10^{-5}$
ITc (825°C)	$32 \times 10^{-6} \pm 8 \times 10^{-6}$	ITc (675°C)	$17 \times 10^{-5} \pm 2 \times 10^{-5}$
		QTa (575°C)	$30 \times 10^{-5} \pm 2 \times 10^{-5}$
		QTb (600°C)	$15 \times 10^{-5} \pm 4 \times 10^{-5}$
		QTc (625°C)	$16 \times 10^{-5} \pm 1 \times 10^{-5}$
		QTd (650°C)	$17 \times 10^{-5} \pm 1 \times 10^{-5}$

The results for interphase-precipitated vanadium steel show that specimens transformed isothermally at lower temperatures exhibited better resistance than the specimen transformed at 825°C. This could be explained by analysing the heat treat-

ment curves in Figure 4.6. Transformation from one phase to another is accompanied by a change in the specimen's macroscopic volume as explained before in Section 2.3, therefore, the change in length labelled in the figures indicate when transformations occur. Figures 4.6a,b show that the transformation from austenite to ferrite is completed as the curve flattens at the transformation temperature. However, in Figure 4.6c, which corresponds to the specimen transformed isothermally at 825°C, the curve does not completely flatten and further change in length occurs upon cooling, indicating martensitic transformation. The incompleted transformation from austenite to ferrite is undesirable in this application as it suggests that not all available carbon has been tied up in carbides, therefore, carbon activity will be higher, hence methane formation is more likely to occur. Nonetheless, this isothermally-transformed specimen has shown a lower increase in void volume-fraction than the best performing specimen in $2\frac{1}{4}$Cr-1Mo, which could indicate the better resistance of vanadium carbides to carbides present in $2\frac{1}{4}$Cr-1Mo such as M_6C, M_2C, M_7C_3 and $M_{23}C_6$.

Further investigations using optical microscopy revealed two clearly distinguished phases, martensite and ferrite in vanadium steel transformed isothermally at 825°C as can be seen in Figure 4.7a, while only one phase, ferrite, can be identified in Figure 4.7b, corresponding to vanadium steel transformed isothermally at 725°C.

Measuring hardness of the different phases can add to the evidence for the presence of martensite. Micro-hardness testing was carried out on all vanadium steel specimens, Table 4.5. The hardness of ferrite is the highest at the lowest transformation temperature, due to the finer dispersion of carbides at lower transformation temperatures, as was discussed in Section 1.3.1 and witnessed by [27, 28, 61]. The micro-hardness measurements were uniform across the specimens transformed at 725°C and 775°C, however, a large difference was detected between the two distinguished phases in the specimen transformed at 825°C. The relative fractions of the phases can be estimated using the following equation [92]:

$$V_V{}^{\alpha} \approx \frac{\mathrm{HV}_{\alpha'} - \mathrm{HV}}{\mathrm{HV}_{\alpha'} - \mathrm{HV}_{\alpha}} \tag{4.1}$$

where $\mathrm{HV}_{\alpha'}$ is the hardness of freshly quenched martensite, HV_{α} is that of a fully fer-

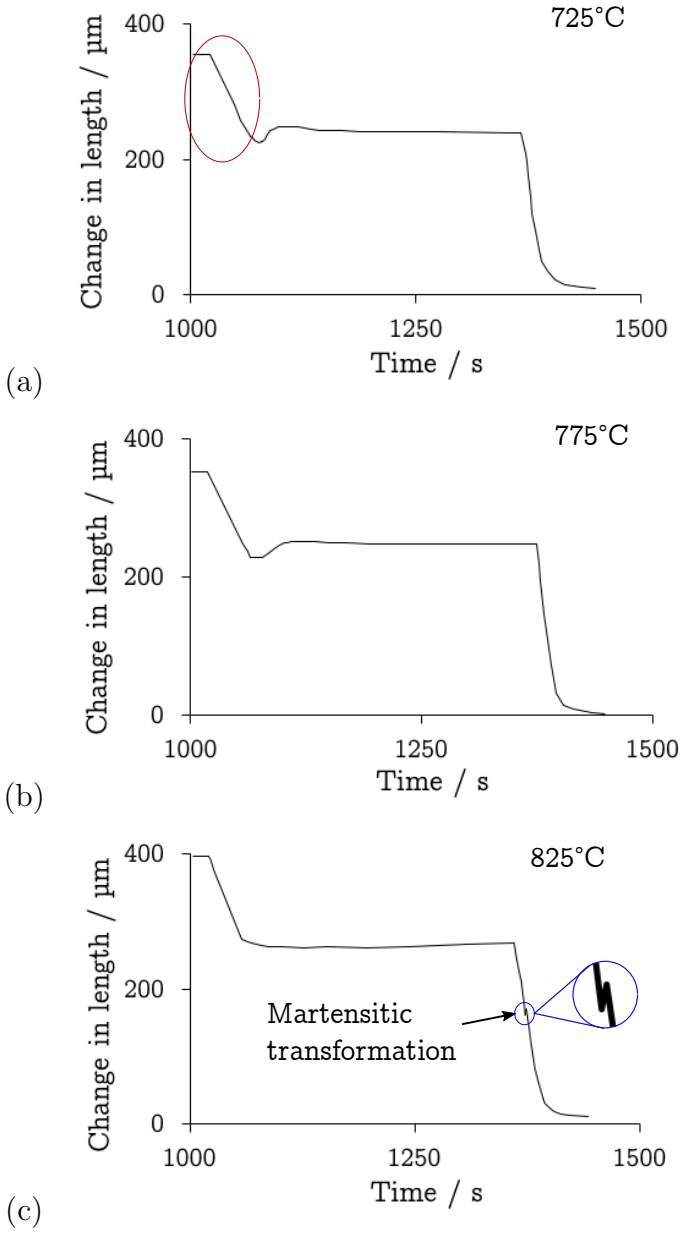

Figure 4.6: Change in length during the heat treatment of vanadium steel showing that the transformation at 825°C was not completed as the curve does not flatten at the transformation temperature. The figures only show austenite to ferrite transformation regions for clarification purposes. The area circled in red represents cooling down from the austenisation region to the ferrite transformation region. The same area applies for the other figures.

ritic specimen. By using Equation 4.1, the relative fraction of ferrite can be estimated for the specimen containing ferrite and martensite. $HV_{\alpha'}$ was calculated by quenching a specimen to be 386 $HV_{0.1}$, HV_{α} was taken to be the ferrite hardness in specimen C,

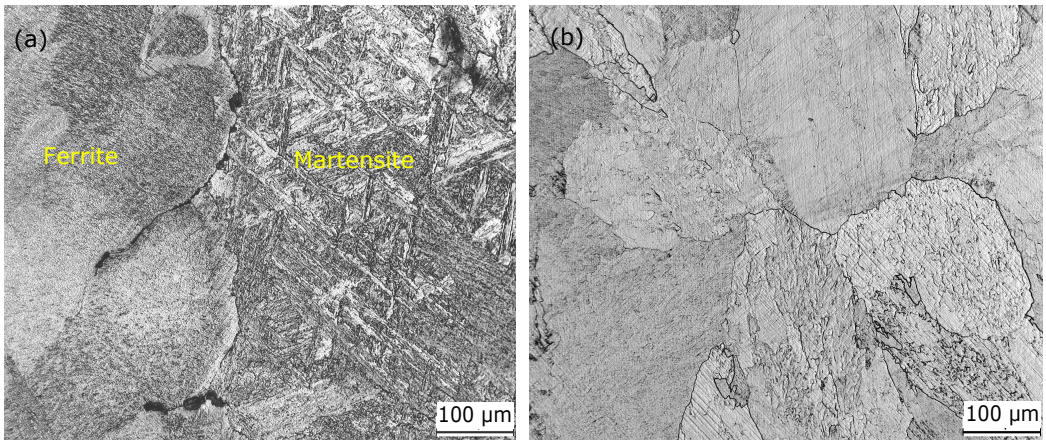

Figure 4.7: Micrographs of vanadium steel microstructure transformed isothermally at a) 825°C, showing two different phases, martensite and ferrite. b) 725°C, showing one phase, i.e. ferrite.

while HV is the average hardness in specimen C, equalling 243 $HV_{0.1}$. This gave an estimated ferrite volume fraction of 0.63, leaving 0.37 as martensite in specimen C, explaining the larger increase in void volume-fraction as seen in Table 4.4. Cracks and bubbles were seen using SEM at the interface grain boundaries and across the martensitic region as shown in Figure 4.8. Therefore the increase in void volume-fraction is a consequence of the combined effect of the difference in the hardness across the specimen as well as the presence of available carbon in martensite for the methane formation. Further analysis by synchrotron X-rays will follow in the next section. The slight increase in void volume-fraction in some of HT10 specimens could not be explained by microscopy, therefore, it was analysed further using synchrotron X-ray as well.

Table 4.5: Micro-hardnesss measurements of isothermally-transformed vanadium steel at different temperatures.

Sample	Hardness ($HV_{0.1}$)	Phase
A (725°C)	354 ± 3	Ferrite
B (775°C)	271 ± 3	Ferrite
C (825°C)	161 ± 3	Ferrite
	325 ± 4	Martensite

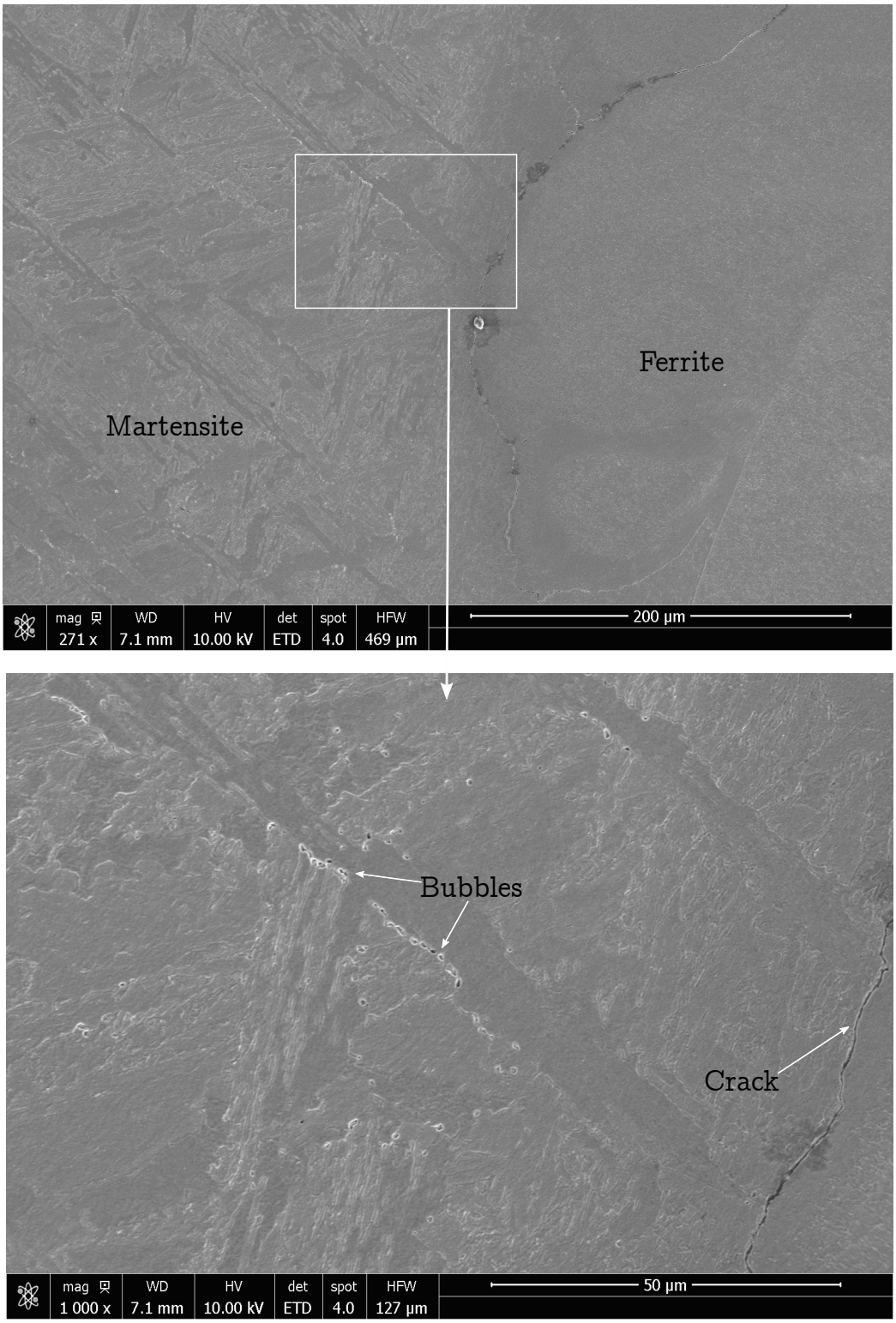

Figure 4.8: SEM micrographs of vanadium steel microstructure transformed isothermally at 825°C, showing two different phases, martensite and ferrite. Cracks are observed at the interface, while bubbles are seen across the martensitic phase.

The void volume-fraction analysis of interphase-precipitation in vanadium and HT10 steels along the quenched and tempered HT10 steel show that hydrogen attack was mitigated in many cases, e.g. vanadium steel ITa and ITb, HT10 steel ITc, QTb, QTc and QTd. While void volume-fraction has increased in the other specimens, vanadium steel ITc, HT10 steel ITa, ITb, QTa, it exhibited lower levels of increase when compared with previous work on $2\frac{1}{4}$Cr-1Mo. The unfinished austenite to ferrite transformation is liable for the voids increase in vanadium steel ITc, but the increase in HT10 specimens could not be explained by simple microstructural analysis. The following section includes an examination of the volume fraction of carbides before and after hydrogen-exposure.

4.4.2 Hydrogen-attack resistance of carbides

Both unexposed and hydrogen-exposed specimens were examined using synchrotron X-ray to compare the carbide volume fractions before and after hydrogen-exposure. The specimens were analysed horizontally from surface to surface with a distance of 0.5 mm between each measurement point in the same row, following the representation in Figure 3.7. All values in the same position are averaged to give one spectrum for that position, which is then analysed using Reitveld analysis to calculate carbide fractions at that position. The work in this section aims to discuss the hydrogen attack resistance in three conditions; interphase-precipitated vanadium steel, conventionally heat-treated HT10 steel, isothermally-transformed HT10 steel.

Interphase-precipitated vanadium steel: Table 4.6 contains the MC carbide volume fractions in all vanadium steel specimens before and after hydrogen exposure, while Figure 4.9 is a representation of those fractions. When the transformation was completed, at 725°C and 775°C, MC carbide did not undergo any depletion after hydrogen exposure, which agrees with the void volume-fraction measurements in Table 4.4, but a noticeable increase in void volume-fraction was measured in the specimen transformed isothermally at 825°C. The depletion seen in Figure 4.9c is expected to have occurred in the martensitic region of the specimen, Figure 4.8. To reiterate, the martensitic region only formed in this specimen due to uncompleted isothermal transformation from austenite to ferrite, leading to undesirable carbon activity in the martensitic region.

The chemical compositions of vanadium carbide were investigated using EDX in TEM, then compared with the equilibrium compositions and volume fractions estimated by *ThermoCalc*. As can been from Tables 4.7 and 4.8, neither the MC volume fraction nor its composition across different specimen are close to equilibrium, yet no depletion can be detected for MC carbide, where isothermal transformation to ferrite was completed. However, in $2\frac{1}{4}$Cr-1Mo, carbides have depleted noticeably when they were not at equilibrium as seen in the example of $M_{23}C_6$ in Figure 4.9d. This

shows that the effect of precipitating stable vanadium carbides is far more superior than chromium carbides in terms of their resistance to be dissociated by hydrogen, which could correlate with the fact that vanadium enhances creep-rupture strength and tensile strength at elevated temperatures [45], thus limiting the power-law creep attack mechanism.

As mentioned on page 31, precipitates are expected to be finer in size and spacing as the transformation temperature is reduced, but that does not seem to influence the hydrogen attack resistance. Unfortunately, due to faulty TEM sample holder, it was not possible to tilt all the specimens to observe interphase precipitation and calculate the sheet spacing, however, the peaks in the synchrotron X-ray diffraction patterns were broader as the transformation temperature was reduced. This effect is known to be caused by the larger coherency strain field associated with the smaller particle size [100, 101]. Therefore, it can be safe to say that the particles in the specimen transformed isothermally at 725°C were finer than the ones precipitated at 825°C, nonetheless, that did not prove to influence the hydrogen attack resistance.

Table 4.6: Synchrotron-measured carbide volume-fractions of MC carbide in vanadium steel specimens before and after hydrogen-exposure. Underlined are the positions where carbide depletion has occurred.

	725°C	775°C	825°C
Unexposed	0.0098 ± 0.0012	0.0095 ± 0.0003	0.0062 ± 0.0007
AE (1)	0.0086 ± 0.0015	0.0108 ± 0.0017	<u>0.0036 ± 0.0009</u>
AE (2)	0.0082 ± 0.001	0.0109 ± 0.0018	<u>0.0036 ± 0.0012</u>
AE (3)	0.0084 ± 0.0014	0.0101 ± 0.0015	<u>0.004 ± 0.0014</u>
AE (4)	0.0096 ± 0.0018	0.0108 ± 0.0009	<u>0.0036 ± 0.0015</u>
AE (5)	0.0106 ± 0.0017	0.0099 ± 0.0014	0.0059 ± 0.0018
AE (6)	0.0107 ± 0.0025	0.0104 ± 0.0018	0.0063 ± 0.0018
AE (7)	0.0093 ± 0.0017	0.0094 ± 0.0017	0.0079 ± 0.0019
AE (8)	0.0106 ± 0.0015	0.0092 ± 0.0013	0.0077 ± 0.002
AE (9)	0.0091 ± 0.0019	0.0104 ± 0.0012	0.0055 ± 0.002

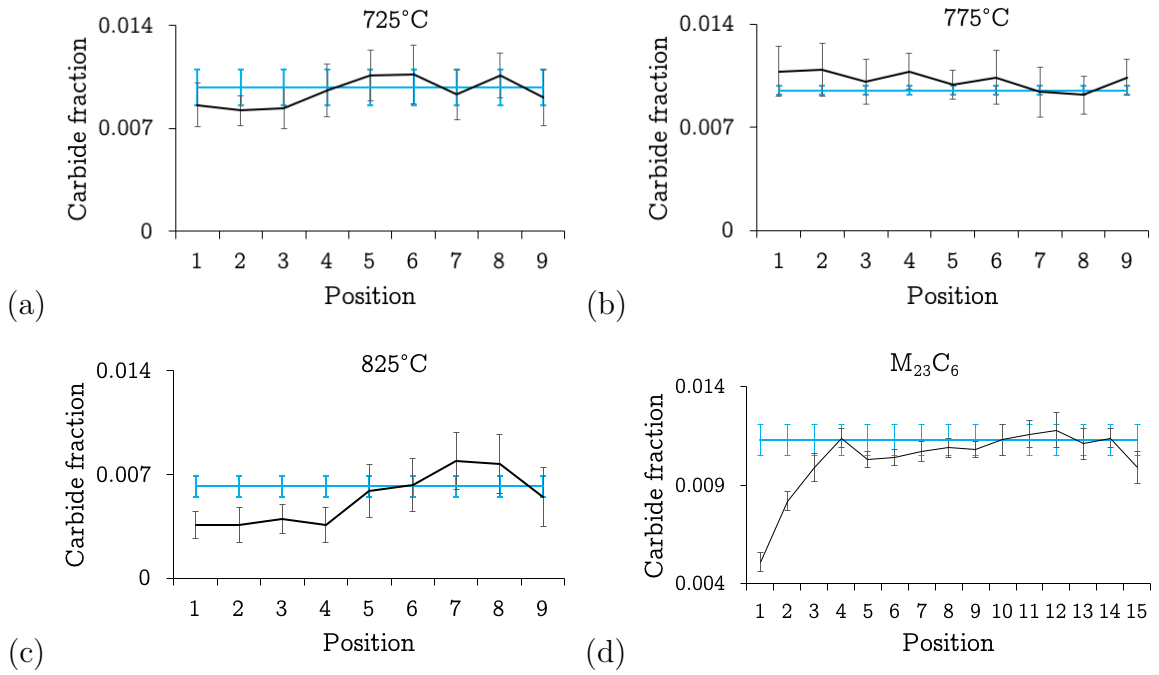

Figure 4.9: a,b and c) Volume fraction of MC carbide in vanadium steel transformed isothermally at different temperatures for 5 minutes. d) For comparison purposes, volume fraction of $M_{23}C_6$ in previously tested $2\frac{1}{4}$Cr-1Mo steel, where the carbide was not at equilibrium composition or volume fraction and underwent depletion upon hydrogen-exposure. The fractions prior to exposure are represented by the blue lines.

Table 4.7: Volume fractions of MC carbide as expected under equilibrium using *Thermo-Calc* (T.C.) and as determined using synchrotron X-ray diffraction for isothermally transformed vanadium steel.

		MC
Temperature	T.C.	Rietveld
725°C	0.0199	0.0098 ± 0.0012
775°C	0.0197	0.0095 ± 0.0003
825°C	0.0193	0.0062 ± 0.0007

Table 4.8: Equilibrium and measured chemical compositions (wt%) of MC carbide in vanadium steel at different isothermal transformation (IT) temperatures. *ThermoCalc* is used to calculate the equilibrium composition. EDX in TEM was used to measure the actual chemical composition. As carbon content cannot be measured using EDX, all the carbon content values are calculated by *ThermoCalc* and EDX measurements for other elements were corrected accordingly.

	Sample B IT @ 775 °C for 5 min		Sample C IT @ 825 °C for 5 min	
	T.C.	EDX	T.C.	EDX
C	16.72	–	16.75	–
Fe	6.48	64.44 ± 2.01	6.47	78.81 ± 0.18
V	76.79	18.83 ± 0.92	76.78	4.34 ± 0.04

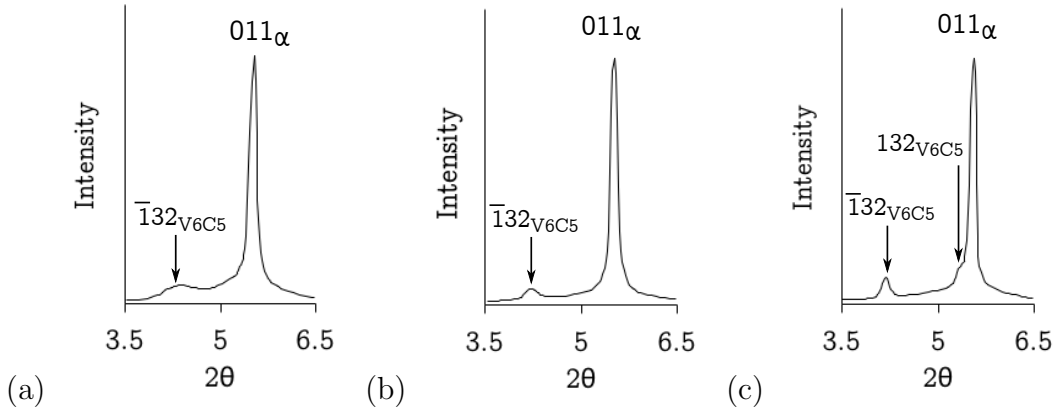

Figure 4.10: Synchrotron X-ray diffractograms of vanadium steel specimens transformed isothermally at a) 725°C, b) 775°C and c) 825°C. The broad peaks for the V_6C_5 carbides indicate finer precipitation.

Conventionally heat-treated HT10 steel: Moving on to the analysis of HT10 specimens, the volume fractions of carbides before and after hydrogen-exposure can be found in Table 4.9, with profile representations in Figure 4.11. Regardless of the tempering temperature, no depletion was detected for any of the carbides. HT10 is an improved version of the previously tested $2\frac{1}{4}$Cr-1Mo. While HT10 has not been examined for its resistance to hydrogen attack, however, with the vanadium addition, it is expected that HT10 steel would have a better hydrogen-attack resistance than $2\frac{1}{4}$Cr-1Mo steel. The interesting result is that more carbides have precipitated during the exposure to hydrogen at 525°C, which proves the hypothesis suggested in Section 3.4.2, when M_2C and $M_{23}C_6$ carbides were seen to increase in volume fraction upon the exposure to hydrogen at 525°C. No M_2C carbide was detected after tempering at 575°C for 11 h, however, after the hydrogen exposure at 525°C for 20 days, high volume fractions of that carbide were found, Figure 4.11b. This suggests that tempering HT10 steel for 11 h at temperature less than 650°C is not adequate enough to reach equilibrium, nonetheless, the hydrogen-attack resistance was also seen here to be better than that of $2\frac{1}{4}$Cr-1Mo at different tempering conditions. Again, this can be explained by the vanadium addition that stabilises the carbides against the dissociation by hydrogen. Therefore, it can be suggested that if the steel has good hydrogen attack resistance, then hydrogen exposure at high temperatures would not cause hydrogen attack but will be considered as tempering the steel due to the high exposure temperature.

Comparisons between equilibrium and measured volume fractions and chemical compositions of carbides for quenched and tempered HT10 steel can be found in Tables 4.10 and 4.11 respectively. It should be noted that MC carbide is considered to be a metastable phase, in this case, because the equilibrium results given were only obtained after the suppression of M_2C and M_6C carbides. The results shows that MC carbide volume fractions were very similar to those expected by *ThermoCalc*, while its composition lacked molybdenum and significant percentages of vanadium. Nevertheless, the carbide has shown excellent hydrogen attack resistance, Figure 4.11. M_2C was not detected at 575°C but its volume fraction increased as the tempering temperature increased. It did not reach equilibrium but it was the closest at the

highest tempering temperature, Table 4.10. This correlates well with the chemical compositions measured for M_2C, Table 4.11, where the carbide was richer in alloying elements and closer to its equilibrium composition as the tempering temperature increased.

As mentioned in Section 4.2.1, The ability of HT10 steel to trap hydrogen is excellent and it is at maximum when the steel is tempered at 575°C, but it decreases as the tempering temperature increases. Unfortunately, there is no clear evidence of the influence of hydrogen trapping capacity on the hydrogen attack resistance. If anything, measurements of void volume-fraction, Table 4.4, revealed a slight increase at 575°C but not at other tempering temperatures. But that does not prove any relation between hydrogen trapping capacity and high-temperature high-pressure hydrogen attack resistance.

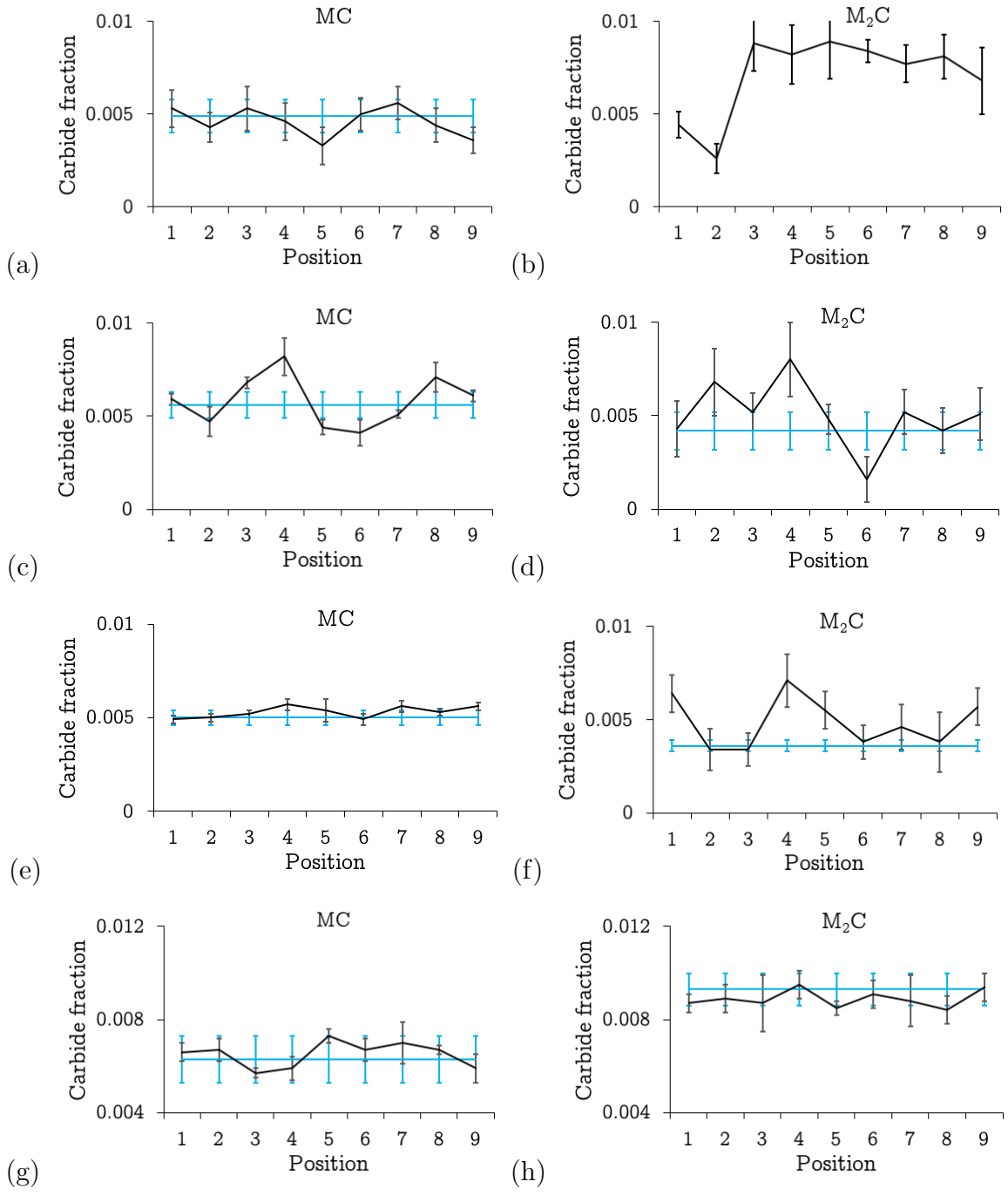

Figure 4.11: Quenched and tempered HT10 specimens; (a) and (b) @ 575°C, (c) and (d) 600°C, (e) and (f) @ 625°C, (g) and (h) @ 675°C. The fractions prior to exposure are represented by the blue lines.

Table 4.9: Synchrotron-measured carbide volume-fractions for quenched and tempered HT10 specimens, All tempering durations were 11 h. Underlined are the positions where carbide depletion was detected.

	QT @ 575°C		QT @ 600°C	
	MC	M_2C	MC	M_2C
Unexposed	0.0049 ± 0.0009	Not detected	0.0056 ± 0.0007	0.0042 ± 0.001
AE (1)	0.0053 ± 0.001	0.0044 ± 0.0007	0.0059 ± 0.0003	0.0043 ± 0.0015
AE (2)	0.0043 ± 0.0008	0.0026 ± 0.0008	0.0047 ± 0.0008	0.0068 ± 0.0018
AE (3)	0.0053 ± 0.0012	0.0088 ± 0.0015	0.0068 ± 0.0003	0.0052 ± 0.001
AE (4)	0.0046 ± 0.001	0.0082 ± 0.0016	0.0082 ± 0.0016	0.008 ± 0.0012
AE (5)	0.0033 ± 0.001	0.0089 ± 0.002	0.0044 ± 0.0004	0.0048 ± 0.0008
AE (6)	0.005 ± 0.0009	0.0084 ± 0.0006	0.0041 ± 0.0007	<u>0.0016 ± 0.0012</u>
AE (7)	0.0056 ± 0.0009	0.0077 ± 0.001	0.0051 ± 0.0002	0.0052 ± 0.0012
AE (8)	0.0044 ± 0.0009	0.0081 ± 0.0012	0.0071 ± 0.0008	0.0042 ± 0.0012
AE (9)	0.0036 ± 0.0007	0.0068 ± 0.0018	0.0061 ± 0.0003	0.0051 ± 0.0014
	QT @ 625°C		QT @ 650°C	
	MC	M_2C	MC	M_2C
Unexposed	0.005 ± 0.0004	0.0036 ± 0.0003	0.0063 ± 0.001	0.0093 ± 0.0007
AE (1)	0.0049 ± 0.0002	0.0064 ± 0.001	0.0066 ± 0.0004	0.0087 ± 0.0004
AE (2)	0.005 ± 0.0002	0.0034 ± 0.0011	0.0067 ± 0.0005	0.0089 ± 0.0006
AE (3)	0.0052 ± 0.0002	0.0034 ± 0.0009	0.0057 ± 0.0002	0.0087 ± 0.0012
AE (4)	0.0057 ± 0.0003	0.0071 ± 0.0014	0.0059 ± 0.0005	0.0095 ± 0.0006
AE (5)	0.0054 ± 0.0006	0.0055 ± 0.001	0.0073 ± 0.0003	0.0085 ± 0.0003
AE (6)	0.0049 ± 0.0003	0.0038 ± 0.0009	0.0067 ± 0.0005	0.0091 ± 0.0006
AE (7)	0.0056 ± 0.0003	0.0046 ± 0.0012	0.007 ± 0.0009	0.0088 ± 0.0011
AE (8)	0.0053 ± 0.0002	0.0038 ± 0.0016	0.0067 ± 0.0002	0.0084 ± 0.0006
AE (9)	0.0056 ± 0.0002	0.0057 ± 0.001	0.0059 ± 0.0006	0.0094 ± 0.0006

Table 4.10: Volume fractions of carbides as expected under equilibrium or constrained equilibrium conditions using *ThermoCalc* and as determined using synchrotron X-ray diffraction for the quenched/tempered HT10 specimens.

	Sample A QT @ 575°C		Sample B QT @ 600°C	
	T.C.	Rietveld	T.C.	Rietveld
MC	0.0049	0.0049 ± 0.0009	0.0049	0.0056 ± 0.0007
M_2C	0.0129	Not detected	0.0137	0.0042 ± 0.0010
	Sample C QT @ 625°C		Sample D QT @ 650°C	
	T.C.	Rietveld	T.C.	Rietveld
MC	0.0049	0.0050 ± 0.0004	0.0048	0.0063 ± 0.0010
M_2C	0.0136	0.0036 ± 0.0003	0.0135	0.0093 ± 0.0007

Table 4.11: Equilibrium and measured chemical compositions (wt%), as expected under equilibrium or constrained equilibrium conditions, of MC and M_2C carbide in vanadium steel at different tempering temperatures. All tempering duration are 11 h. *ThermoCalc* is used to calculate the equilibrium composition. EDX in TEM was used to measure the actual chemical composition. As carbon content cannot be measured using EDX, all the carbon content values are calculated by *ThermoCalc* and EDX measurements for other elements were corrected accordingly.

	Sample A QT @ 575°C		Sample B QT @ 600°C		Sample C QT @ 625°C		Sample D QT @ 650°C	
				MC				
	T.C.	EDX	T.C.	EDX	T.C.	EDX	T.C.	EDX
C	14.17	–	14.18	–	14.19	–	14.19	–
V	35.21	19.93 ± 3.41	35.19	3.88 ± 0.77	35.11	17.12 ± 1.36	35.04	13.07 ± 1.30
Mo	50.60	–	50.62	–	50.69	–	50.75	–
Fe	–	65.85 ± 5.03	–	81.92 ± 2.95	–	68.58 ± 1.59	–	72.73 ± 3.00
				M_2C				
	T.C.	EDX	T.C.	EDX	T.C.	EDX	T.C.	EDX
C	7.16	–	7.18	–	7.21	–	7.24	–
V	20.31	–	20.31	7.22 ± 0.96	20.29	23.44 ± 1.76	20.24	10.43 ± 1.69
Mo	68.27	–	67.77	5.56 ± 1.86	66.97	28.88 ± 3.90	66.45	48.48 ± 5.15
Fe	0.10	–	0.15	77.81 ± 2.84	0.26	30.44 ± 2.00	0.36	13.81 ± 2.12
Cr	4.10	–	4.48	2.18 ± 0.75	5.15	9.96 ± 1.35	5.59	19.96 ± 1.48

Isothermally-transformed HT10 steel: The isothermal transformation of HT10 steel is an area that has not been explored at all in the literature. Current literature suggests that only MC and M_2C carbides are precipitated in this steel [99]. However, as predicted by *ThermoCalc*, M_6C precipitation proves a closer to equilibrium state than the precipitation of MC carbide precipitation, Figure 4.3. As seen from the synchrotron X-ray analysis, Figures 4.12, 4.13 and 4.14, M_6C precipitation occurs in HT10 steel. At first glance, this suggests that the isothermal transformation of HT10 steel for a prolonged duration of 72 h brings the steel closer to equilibrium than conventional quench and temper heat treatment, increasing the hydrogen attack resistance. However, in this case, that does not indicate better hydrogen attack resistance, because it can be clearly seen from Figures 4.12c and 4.13c that M_6C undergoes a very clear depletion upon hydrogen-exposure when the steel is transformed isothermally at 625°C and 650°C and a slight depletion at 675°C, Figure 4.14c. This further agrees with the void volume-fraction measurements in Table 4.4. This may seem odd at first sight, however, if Table 4.3 is recalled, M_6C equilibrium composition contains a minute amount of vanadium, which was also confirmed using EDX, where some carbides in the specimen transformed isothermally at 650°C, contained approximately 45 wt% of alloying elements but no vanadium with the remaining 55 wt% being iron and carbon. Both MC and M_2C contain vanadium and no depletion was detected there, which could further support the fact that the lack of vanadium in M_6C in HT10 steel makes it prone to being dissociated by hydrogen in order to form methane gas.

Further precipitation of M_2C upon hydrogen exposure at 525°C also occurred in some specimens, Figures 4.13c and 4.14c.

Table 4.12: Synchrotron-measured carbide volume-fractions for HT10 steel transformed isothermally at 625°C for 72 h. Underlined are the positions where carbide depletion has occurred.

	MC	M_2C	M_6C
Unexposed	0.0074 ± 0.0003	0.006 ± 0.001	0.0057 ± 0.0004
AE (1)	0.0083 ± 0.001	0.0057 ± 0.0004	0.0022 ± 0.0005
AE (2)	0.0064 ± 0.0004	0.0061 ± 0.0016	0.0036 ± 0.0016
AE (3)	0.0065 ± 0.001	0.006 ± 0.0012	0.0037 ± 0.0015
AE (4)	0.0074 ± 0.0005	0.0055 ± 0.0011	0.0024 ± 0.0012
AE (5)	0.0062 ± 0.001	0.0054 ± 0.0004	0.0013 ± 0.001
AE (6)	0.0066 ± 0.0008	0.0052 ± 0.0007	0.0029 ± 0.0013
AE (7)	0.0062 ± 0.001	0.0052 ± 0.0004	0.0027 ± 0.0004
AE (8)	0.0073 ± 0.0006	0.0071 ± 0.0016	0.0024 ± 0.0006
AE (9)	0.0074 ± 0.0004	0.0051 ± 0.0016	0.0021 ± 0.0013

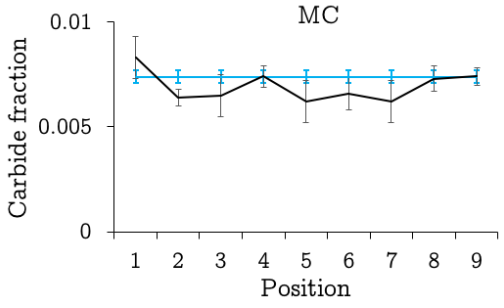

(a)

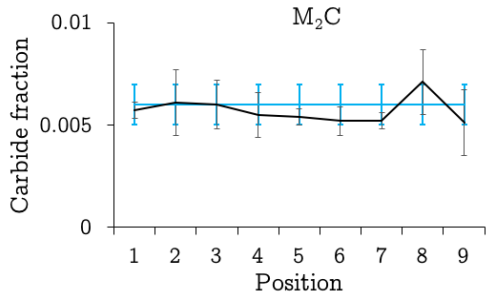

(b)

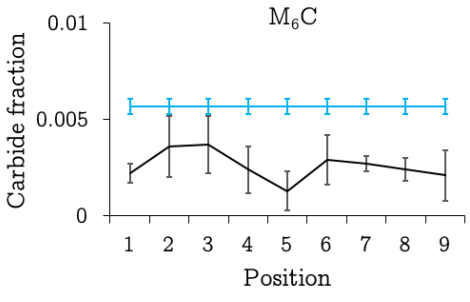

(c)

Figure 4.12: Volume fraction of carbides precipitated in HT10 steel transformed isothermally at 625° for 72 h. The fractions prior to exposure are represented by the blue lines.

Table 4.13: Synchrotron-measured carbide volume-fractions for HT10 steel transformed isothermally at 650°C for 72 h. Underlined are the positions where carbide depletion has occurred.

	MC	M_2C	M_6C
Unexposed	0.0095 ± 0.0007	0.0032 ± 0.0007	0.0107 ± 0.0014
AE (1)	0.0087 ± 0.001	0.0055 ± 0.001	0.0077 ± 0.0011
AE (2)	0.0089 ± 0.0005	0.0056 ± 0.0009	0.0083 ± 0.0009
AE (3)	0.0098 ± 0.0006	0.0051 ± 0.0012	0.0082 ± 0.001
AE (4)	0.0087 ± 0.0005	0.0045 ± 0.0006	0.0078 ± 0.0012
AE (5)	0.0085 ± 0.0005	0.0063 ± 0.0009	0.0064 ± 0.0012
AE (6)	0.0089 ± 0.0003	0.0062 ± 0.0012	0.0072 ± 0.0009
AE (7)	0.0064 ± 0.0015	0.0083 ± 0.0019	0.0054 ± 0.001
AE (8)	0.0085 ± 0.0005	0.0069 ± 0.0014	0.0071 ± 0.0015
AE (9)	0.0081 ± 0.0009	0.0069 ± 0.0014	0.0048 ± 0.0009

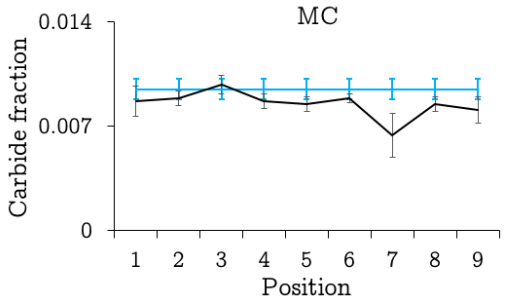

(a)

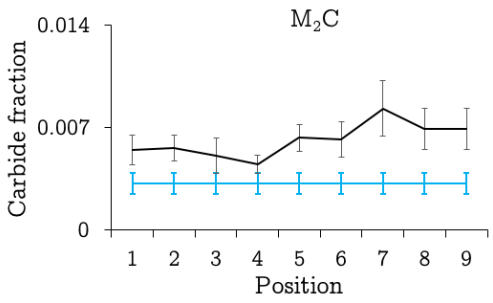

(b)

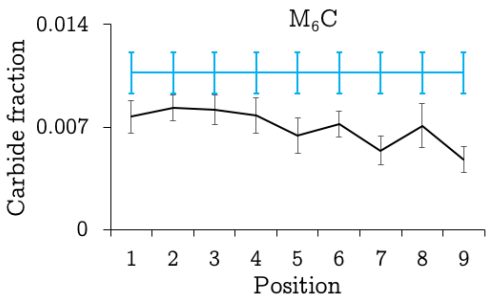

(c)

Figure 4.13: Volume fraction of carbides precipitated in HT10 steel transformed isothermally at 650°C for 72 h. The fractions prior to exposure are represented by the blue lines.

Table 4.14: Synchrotron-measured carbide volume-fractions for HT10 steel transformed isothermally at 675°C for 72 h. Underlined are the positions where carbide depletion has occurred.

	MC	M_2C	M_6C
Unexposed	0.0061 ± 0.0009	0.0049 ± 0.0005	0.0044 ± 0.0004
AE (1)	0.0053 ± 0.0009	0.0068 ± 0.0012	<u>0.0023 ± 0.0008</u>
AE (2)	0.0061 ± 0.001	0.0099 ± 0.0019	0.0045 ± 0.0005
AE (3)	0.007 ± 0.0011	0.0066 ± 0.001	0.0048 ± 0.0004
AE (4)	0.0054 ± 0.001	0.0049 ± 0.0007	0.0042 ± 0.0004
AE (5)	0.0056 ± 0.0009	0.0068 ± 0.0015	0.0043 ± 0.0003
AE (6)	0.0068 ± 0.0008	0.0082 ± 0.002	0.0048 ± 0.0005
AE (7)	0.0052 ± 0.001	0.0056 ± 0.0007	0.0046 ± 0.0003
AE (8)	0.0052 ± 0.0009	0.0072 ± 0.001	0.0041 ± 0.0002
AE (9)	0.0057 ± 0.0009	0.0092 ± 0.002	0.0041 ± 0.0001

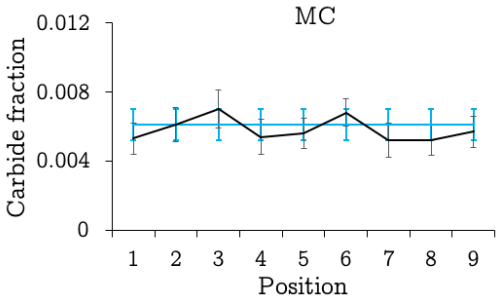

(a)

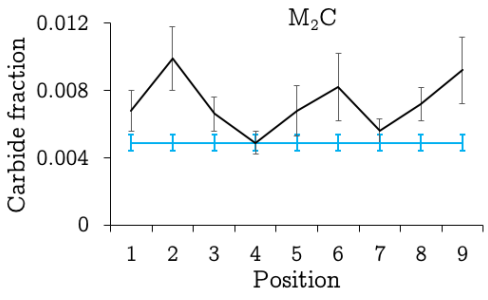

(b)

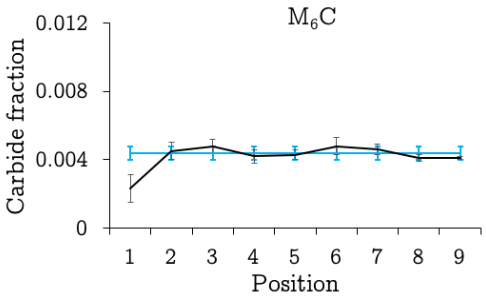

(c)

Figure 4.14: Volume fraction of carbides precipitated in HT10 steel transformed isothermally at 675° for 72 h. The fractions prior to exposure are represented by the blue lines.

4.5 Conclusions on mitigation methods

The principal conclusions are as follows:

- previous research [30, 47] has shown that the addition of vanadium to commercially-used steels, such as $2\frac{1}{4}$Cr-1Mo, decreases the carbon activity of the carbides present. This was also the case in this research when vanadium was added to HT10 steel, which is known for its resistance to low-temperature hydrogen embrittlement due to excellent hydrogen-trapping capacity. However, it was found that the improved high-temperature hydrogen attack resistance in HT10 is due to the precipitation of alloying-element enriched carbides, especially vanadium. The hydrogen trapping capacity did not influence hydrogen attack resistance.

- Carbides that do not contain vanadium, M_6C, underwent noticeable depletion by hydrogen when its composition was not close to equilibrium, suggesting that lack of vanadium requires lengthy tempering durations at high temperatures to stabilise the carbides, reducing carbon activity, which was the case in the $2\frac{1}{4}$Cr-1Mo steel.

- Previous research has focused only on how vanadium addition to heavily-alloyed steels influences their hydrogen attack resistance, but hydrogen attack resistance has never been examined on steels that only contain vanadium as a substitutional solute. In this project, the vanadium steel exhibited excellent hydrogen attack resistance when isothermally transformed. The resistance was also not affected when carbides were far from their equilibrium state, which was not the case in $2\frac{1}{4}$Cr-1Mo steel, where equilibrium conditions had to be ensured to avoid any noticeable depletion in carbides.

  Only undesirable conditions deteriorated the resistance of vanadium steel, such as unfinished austenite to ferrite transformation, which led to untempered martensite with its high carbon activity, hence methane bubble formation. This is a significant result as it challenges the current paradigm that classi-

fies chromium as a necessary element in the steel to resist hydrogen attack.

- Interphase precipitation of vanadium steel has been shown to be a better alternative to conventional heat treatments in $2\frac{1}{4}$Cr-1Mo steel as it requires less tempering durations and precipitates carbides that are not affected by hydrogen exposure, even if their volume fraction or composition were far from equilibrium. The complete transformation from γ to α, in interphase precipitation, must be ensured, otherwise residual austenite containing carbon will lead to martensite formation with its high carbon activity.

- The mitigation of hydrogen attack observed in interphase-precipitation vanadium steel is mainly due to the minimisation of carbon activity by tying up all carbon with stable vanadium carbides directly at the γ/α interface. It is speculated that direct precipitation at the γ/α interface leaves the ferrite immediately depleted of carbon. On the other hand, tempered martensite contains many lattice defects, which may retain excess carbon that would be available for reaction with hydrogen to form methane.

- Isorthermal transformation is not an ideal treatment for high-hardenability steels, such as HT10, when hydrogen-attack resistance is the goal. This is because of the lengthy transformation durations needed for a completely ferritic microstructure, which does not guarantee elimination of unstable carbides. Conventional quench and temper heat treatments for shorter durations in HT10 steel resulted in better hydrogen attack resistance. Therefore, conventional heat treatments should be followed for high-hardenability steels, such as HT10 and $2\frac{1}{4}$Cr-1Mo steels.

- Further precipitation upon hydrogen exposure, in a temperature range where secondary hardening occurs, is possible as confirmed by the precipitation of M_2C after hydrogen exposure at 575°C in HT10 steel. Therefore, if initially only stable carbides are precipitated during heat treatment without tying all carbon, then further precipitation is possible upon exposure to high temperatures.

Chapter 5

Final conclusions and future work

The main goal of this work was to find a solution to mitigate high-temperature high-pressure hydrogen attack. As a starting point, the current design standard was studied along with previous research on the topic to identify knowledge gaps that have kept the advancement of this field at bay. The design standard only specified fundamental factors, such as steel composition and operating parameters, while recent literature, to our knowledge, has focused only on the modelling aspect in order to understand hydrogen attack.

A more detailed experimental examination of a commercially-used steel was done in this work, which led to insights, helping to propose mitigation solutions that were then examined to deliver the following conclusions:

- the carbon activity in the carbides is the driving force for hydrogen attack. Deviation of the service microstructure from thermodynamic equilibrium with respect to precipitated carbides determines how reactive they can be with hydrogen. The carbon activity is not just a function of carbide-type only but also of tempering conditions. For example, it was seen that the equilibrium carbide, $M_{23}C_6$, underwent clear depletion during hydrogen exposure when $2\frac{1}{4}$Cr-1Mo steel was tempered for 50 h at 650°C, but no such depletion occurred when the tempering was for 5 h at 750°C. Further analysis showed that the latter tem-

pering conditions resulted in better resistance due to the carbides being more enriched with alloying elements such as Cr and Mo. Furthermore, the Cr/Fe ratio in those carbides decreases as the tempering temperature increases, which reduces the carbon activity of the carbides.

This conclusion clearly emphasises on the importance of specifying parameters such tempering conditions in the design standard. It shows also that current modelling work in literature, as enlightening as it is, could be misleading, as it presumes the high resistance of $M_{23}C_6$ at all conditions, considering it being the most thermodynamically equilibrium carbide in the tested steel.

- The first industrial application of this work is to start with deploying HT10 steel in hydrogen-attack applications because it has been proven to have superior properties to $2\frac{1}{4}$Cr-1Mo steel in low-temperature applications, and given that it has the carbide constitution that should give equivalent creep and oxidation resistance as well as the superior resistance to hydrogen-attack shown in this work, then it would place it at an advanced stage in the process of replacing $2\frac{1}{4}$Cr-1Mo steel in high-temperature hydrogen-attack applications.

- Vanadium addition is considered, in the design standard and literature, as an improvement method to hydrogen-attack resistance, which was also confirmed in this project in HT10 steel examination. However, using vanadium solely as a substitutional solute was not tested prior to the present work, for hydrogen attack resistance. The work in this project has shown that vanadium steel, when tempered correctly, undergoes no depletion in precipitated carbides, even when the carbides are not near equilibrium in volume fraction or chemical composition. This is consistent with the ability of vanadium to improve creep-rupture and tensile strengths at high temperatures, which consequently limits the linking of any voids due to hydrogen attack.

- It could be argued that the superior hydrogen-attack resistance in vanadium steel is due to the high transformation temperature studied (725°C), which generated stable carbides, in spite of them being far from equilibrium in terms of volume fraction and chemical composition. However, in the $2\frac{1}{4}$Cr-1Mo steel

examination, the specimen tempered at 700°C for 50 h was still damaged by hydrogen attack, while only the steel tempered at 750°C for 5 h resisted hydrogen attack while being at equilibrium in terms of carbide volume fraction and close to it regarding the carbide chemical composition. Therefore, the superiority in resisting hydrogen attack by the far-from-equilibrium vanadium carbides must be caused by a reason other than high transformation temperatures, which could be the nature of vanadium in introducing creep resistance that limits the linking of voids during hydrogen attack.

- A major outcome from this project was the confirmation of the importance of heat treatment towards mitigating hydrogen attack. Conventional heat treatments were tested and concluded to be viable options to improve the resistance. However, the suggested heat treatment leading to the interphase precipitation in vanadium steel was shown to mitigate hydrogen attack at the same exposure conditions, where other steels suffered. It could be hypothesised that interphase precipitation depletes ferrite of carbon during the transformation from austenite. In contrast, conventional quench/temper heat-treated microstructures contain many lattice defects that may retain excess carbon, which is available to react with hydrogen.

The work in this Ph.D. thesis has shown clearly that isothermally-transformed vanadium steel mitigates the phenomenon of high-temperature high-pressure hydrogen attack. But further experimental work is needed to establish the suggested alloy as a viable alternative in hydrogen-attack applications, because a whole basket of other properties would need to be satisfied:

- the mechanical properties of vanadium steel should be characterised and compared with steel requirements for the components operating in high-temperature high-pressure hydrogen environments. This could be done after alloy design that maintains interphase precipitation but ensures, for example, creep properties. This really is a major work requiring industrial involvement in the definition of the project as this alloy was chosen because it was shown that it undergoes interphase precipitation, but it is not necessarily optimum for creep and

oxidation-resistant applications, therefore much work would be needed to modify the alloy while maintaining interphase-precipitation. However, in spite of the formidable, the method of characterisation of hydrogen-induced damage has been established with clarity, using both comparisons of actual precipitation against equilibrium calculations so that deviation from equilibrium can be established over the service life, and synchrotron X-ray analysis to give clear data on small volume fractions of carbides.

- Creep testing should be carried out to provide concrete evidence that the presence of vanadium carbides limits the hydrogen attack mechanism of power-law creep.

- Limitations in equipment and time did not allow the detailed study of interphase-precipitation characteristics. The influence of carbide size and sheet spacing on hydrogen-attack resistance should be examined to allow any possible improvements.

- A major source of carbon in the steel comes from the carbides as any carbon present in the matrix will be at a very small concentration, therefore, the activity of carbon in the carbide is the one that matters for the methane reaction. Therefore, looking at the reaction of hydrogen with pure carbides should be very interesting to carry out in order to find out the exact behaviour of the carbide when it comes to reacting with hydrogen. This can be done by measuring how much methane is produced from the reaction of pure carbides with hydrogen.

- The addition of boron is said to increase the stability of carbides in $2\frac{1}{4}$Cr-1Mo steel, consistent with the retardation of creep. Hence, boron should be added to $2\frac{1}{4}$Cr-1Mo or lesser steel grades such as 1Cr-0.5Mo, to examine if hydrogen-attack mitigation can be achieved by other means.

Bibliography

1. Anonymous: 'Catastrophic rupture of heat exchanger (seven fatalities)': Tech. Rep. https://www.csb.gov/tesoro-refinery-fatal-explosion-and-fire/, U. S. Chemical Safety and Hazard Investigation Board, Washington, D. C., USA, 2014.

2. P. G. Shewmon: 'Hydrogen attack of carbon steel', *Metallurgical Transactions A*, 1976, **7A**, 279–286.

3. D. Eliezer: 'High-temperature hydrogen attack of carbon steel', *Journal of Materials Science*, 1981, **16**, 2962–2966.

4. M. L. Martin, M. Dafarnia, S. Orwig, D. Moore, and P. Sofronis: 'A microstructure-based mechanism of cracking in high temperature hydrogen attack', *Acta Materialia*, 2017, **140**, 300–304.

5. S. Z. Chavoshi, L. T. Hill, K. E. Bagnoli, R. L. Holloman, and K. M. Nikbin: 'A combined fugacity and multi-axial ductility damage approach in predicting high temperature hydrogen attack in a reactor inlet nozzle', *Engineering Failure Analysis*, 2020, **117**.

6. Anonymous: 'The technical basis document for API RP 941': Tech. Rep. API TR 941-A, American Petroleum Institute, Washington, D. C., USA, 2019.

7. M. W. D. V. D. Burg, E. V. D. Giessen, and R. C. Brouwer: 'Investigation of hydrogen attack in 2.25Cr-1Mo steels with a high-triaxiality void growth model', *Acta Metallurgica*, 1996, **44**, 505–518.

8. S. S. Vagarali, and G. R. Odette: 'A model for the growth of hydrogen attack cavities in carbon steels', *Metallurgical Transactions A*, 1981, **12**, 2071–2082.

9. T. A. Parthasarathy: 'Mechanisms of hydrogen attack of carbon and 2.25Cr-1Mo steels', *Acta Metall.*, 1985, **33**, 1673–1681.

10. H. C. Furtado, and I. L. May: 'High temperature degradation in power plants and refineries', *Materials Research*, 2004, **7**, 103–110.

11. D. J. Benac, and P. McAndrew: 'Reducing the risk of high temperature hydrogen attack (HTHA) failures', *Journal of Failure Analysis and Prevention*, 2012, **12**, 624–627.

12. T. A. Parthasarathy, H. F. Lopez, and P. G. Shewmon: 'Hydrogen attack kinetics of 2.25Cr-1Mo steel weld metals', *Metallurgical Transactions A*, 1985, **16A**, 1143–1149.

13. I. M. Robertson, P. Sofronis, A. Nagao, M. L. Martin, S. Wang, D. W. Gross, and K. E. Nygren: 'Hydrogen embrittlement understood', *Metallurgical & Materials Transactions A*, 2015, **46**, 2323–2341.

14. W. H. Johnson: 'On some remarkable changes produced in iron and steel by the action of hydrogen and acids', *Proceedings of the Royal Society of London*, 1875, **23**, 168–179.

15. R. A. Oriani: 'Hydrogen embrittlement of steels', *Ann. Rev. Mater. Sci.*, 1978, **8**, 327–357.

16. H. K. D. H. Bhadeshia, and R. W. K. Honeycombe: Steels: Microstructure and Properties: 4th ed., Elsevier, 2017.

17. L. C. Weiner: 'Kinetics and mechanism of hydrogen attack of steel', *Corrosion*, 1961, **17**, 109–115.

18. J. J. R. Thygeson, and M. C. Molstad: 'High pressure hydrogen attack of steel', *Journal of Chemical and Engineering Data*, 1964, **9**, 309–315.

19. T. G. Kim: 'Failure of piping by hydrogen attack', *Engineering Failure Analysis*, 2002, **9**, 571–578.

20. P. Shewmon, and Y. H. Xue: 'Effect of high-pressure hydrogen on crack growth in carbon steel', *Metallurgical Transactions A*, 1991, **22A**, 2703–2707.

21. M. Mckimpson, and P. G. Shewmon: 'Initial hydrogen attack kinetics in a carbon steel', *Metallurgical Transactions A*, 1981, **12A**, 825–834.

22. J. Wanagel, T. Hakkarainen, and C. Y. Li: 'Hydrogen attack in thick-section $2\frac{1}{4}$Cr-1Mo steels at elevated temperatures', In: G. Sangdahl, and M. Semchyshen, eds. *Application of $2\frac{1}{4}$Cr-1 Mo Steel for Thick-Wall Pressure.* Ohio, U. S. A.: ASM International, 1982:93–108.

23. T. A. Parthasarathy, and P. G. Shewmon: 'Effects of tempering on the carbon activity and hydrogen attack kinetics of 2.25Cr-1Mo steel', *Metallurgical Transactions A*, 1984, **15**, 2021–2027.

24. H. Wada: 'Thermodynamic properties of carbides in 2.25Cr-1Mo steel at 985 K', *Metallurgical Transactions A*, 1986, **17A**, 1585–1592.

25. F. Abe: 'Effect of boron on microstructure and creep strength of advanced ferritic power plant steels', *Procedia Engineering*, 2011, **10**, 94–99.

26. G. Sundararajan, and P. G. Shewmon: 'The hydrogen attack of HSLA steels', *Metallurgical Transactions A*, 1980, **11A**, 509–516.

27. G. L. Dunlop, and R. W. K. Honeycombe: 'Ferrite morphologies and carbide precipitation in a Cr-Mo-V creep-resisting steel', *Metal Science*, 1976, **10**, 124–132.

28. H.-W. Yen, P.-Y. Chen, C.-Y. Huang, and J.-R. Yang: 'Interphase precipitation of nanometer-sized carbides in a titanium–molybdenum-bearing low-carbon steel', *Acta Materialia*, 2011, **59**, 6264–6274.

29. J. Moon, T. H. Lee, S. D. Kim, C. H. Lee, J. H. Jang, J. H. Shin, J. W. Lee, B. H. Lee, and D. W. Suh: 'Isothermal transformation of austenite to ferrite

and precipitation behavior in 9Cr-1.5Mo-1.25Co-0.1C-VNb heat-resistant steel', *Materials Characterization*, 2020, **170**, 110677.

30. S. M. Schlogl, Y. van Leeuwen, and E. van der Giessen: 'On methane generation and decarburization in low-alloy Cr-Mo steels during hydrogen attack', *Metallurgical and Materials Transactions A*, 2000, **31A**, 125–137.

31. S. M. Schlogl, J. Svoboda, and E. van der Giessen: 'Evolution of the methane pressure in a standard 2.25Cr-1Mo steel during hydrogen attack', *Acta mater.*, 2001, **49**, 2227–2238.

32. E. E. Fletcher, and A. R. Elsea: 'The effects of high-pressure, high-temperature hydrogen on steel': Tech. Rep., Battelle Memorial Institute, 1964.

33. R. Pishko, M. Mckimpson, and P. G. Shewmon: 'The effect of steelmaking on the hydrogen attack of carbon steel', *Metallurgical Transactions A*, 1979, **10A**, 887–894.

34. L. C. Chen, and P. Shewmon: 'Stress-assisted hydrogen attack cracking in 2.25Cr-1Mo steels at elevated temperatures', *Metallurgical and Materials Transactions A*, 1995, **26A**, 2317–2327.

35. K. Yokogawa, S. Fukuyama, K. Kudo, and P. G. Shewmon: 'Effect of hydrogen attack on tensile and creep properties of low carbon steel', *Int. J. of Pressure Vessels and Piping*, 1989, **37**, 365–385.

36. A. A. Sagues, B. O. Hall, and H. Wiedersich: 'On the mechanisms of hydrogen attack', *Scripta Metallurgica*, 1978, **12**, 319–326.

37. M. Natan, and H. H. Johnson: 'An experimental investigation of the internal methane pressure in hydrogen attack', *Metallurgical Transactions A*, 1983, **14A**, 963–971.

38. H.-M. Shih, and H. H. Johnson: 'A model calculation of the nelson curves for hydrogen attack': In: *Perspectives in Hydrogen in Metals*. Pergamon, 1986:163–171.

39. M. W. D. V. D. Burg, E. V. der Giessen, and V. Tvergaard: 'A continuum damage analysis of hydrogen attack in a 2.25Cr-1Mo pressure vessel', *Materials Science and Engineering*, 1998, **A241**, 1–13.

40. T. J. Hakkarainen, J. Wanagel, and C.-Y. Li: 'Direct observations of methane bubbles in a 2.25Cr-1Mo steel after hydrogen exposure', *Metallurgical Transactions A*, 1980, **11A**, 2035–2036.

41. M. Ransick, and P. Shewmon: 'Effect of cold work on hydrogen attack', *Metallurgical Transactions A*, 1981, **12A**, 17–22.

42. S. F. Clugston, J. R. Weertman, and P. G. Shewmon: 'The enhancement of hydrogen attack in steel by prior deformation', *Metallurgical Transactions A*, 1983, **14A**, 695–699.

43. M. W. D. van der Burg, and E. van der Giessen: 'Non-uniform hydrogen attack cavitiation and the role of interaction with creep', *Materials Science and Engineering*, 1996, **A220**, 200–214.

44. S. M. Schlogl, and E. V. der Giessen: 'Micromechanics of high temperature hydrogen attack', *International Journal for Numerical Methods in Engineering*, 2001, **52**, 559–567.

45. J. Hucinska: 'Advanced vanadium modified steels for high pressure hydrogen reactors', *Advances in Materials Science*, 2003, **4**, 21–27.

46. R. Sahara, T. Matsunaga, H. Hongo, and M. Tabuchi: 'Theoretical investigation of stabilizing mechanism by boron in body-centered cubic iron through $(Fe,Cr)_{23}(C,B)_6$ precipitates', *Metallurgical and Materials Transactions A*, 2016, **47A**, 2487–2497.

47. T. Imanaka, J. Shimamura, S. Nakano, and K. Yasuda: 'Hydrogen attack in Cr-Mo steels and disbonding of austenitic stainless weld overlay': Tech. Rep. 13, JFE Steel Corporation, 1985.

48. F. Abe, M. Tabuchi, and S. Tsukamoto: 'Alloy design of MARBN for boiler and turbine applications at 650°C', *Materials at High Temperatures*, 2021, **38**, 306–321.

49. S. V. S. N. Murty, A. K. Jha, and K. S. Kumar: 'Metallographic investigations of the failed superheater tubes used in liquid hydrogen plant', *Engineering Failure Analysis*, 2010, **17**, 313–319.

50. M. B. Djukic, V. S. Zeravcic, G. M. Bakic, A. Sedmak, and B. Rajicic: 'Hydrogen damage of steels: a case study and hydrogen embrittlement model', *Engineering Failure Analysis*, 2015, **58**, 485–498.

51. R. J. Rioja, M. Yacama, M. Moreno, and A. Peraza: 'Direct observation of hydrogen damage in a 304 stainless steel and a 1020 steel', *Scripta Metallurgica*, 1982, **16**, 129–134.

52. A. T. Davenport, and R. W. K. Honeycombe: 'Precipitation of carbides at γ-α boundaries in alloy steels', *Proceedings of the Royal Society of London A*, 1971, **322**, 191–205.

53. A. D. Batte, and R. W. K. Honeycombe: 'Strengthening of ferrite by vanadium carbide precipitation', *Metal Science*, 1973, **7**, 160–168.

54. S. Clark, V. Janik, Y. Lan, and S. Sridhar: 'Interphase precipitation - an interfacial segregation model', *ISIJ International*, 2017, , DOI: 10.2355/isijinternational.ISIJINT–2016–544.

55. F. A. Khalid, and D. V. Edmonds: 'Interphase precipitation in microalloyed engineering steels and model alloy', *Materials Science and Technology*, 1992, **9**, 384–396.

56. R. Lagneborg, T. Siwecki, S. Zajac, and B. Hutchinson: 'The role of vanadium in microalloyed steels': Reprinted from The Scandanavian Journal of Metallurgy, 1999.

57. R. W. K. Honeycombe: 'Carbide precipitation in ferrite', In: A. R. Marder, and J. I. Goldstein, eds. *Phase Transformations in Ferrous Alloys*. Warrendale, Pennsylvania, USA: TMS-AIME, 1984:259–280.

58. R. A. Ricks, and P. R. Howell: 'The formation of discrete precipitate dispersions on mobile interphase boundaries in iron-base alloys', *Acta Metallurgica*, 1983, **31**, 853–861.

59. K. Seto, Y. Funakawa, and S. Kaneko: 'Hot rolled high strength steels for suspension and chassis parts "Nanohiten" and BHT steel', *JFE GIHO*, 2007, (16), 28–33.

60. H. K. D. H. Bhadeshia: 'Diffusional transformations: the nucleation of superledges', *Physica Status Solidi A*, 1982, **69**, 745–750.

61. S. P. Tsai, T. C. Su, J. R. Yang, C. Y. Chen, Y. T. Wang, and C. Y. Huang: 'Effect of Cr and Al additions on the development of interphase-precipitated carbides strengthened dual-phase ti-bearing steels', *Materials and Design*, 2017, **119**, 319–325.

62. K. Campbell, and R. W. K. Honeycombe: 'The isothermal decomposition of austenite in simple chromium steels', *Metal Science*, 1974, **8**, 197–203.

63. C. Capdevila, F. G. Caballero, and C. G. de Andrés: 'Austenite grain size effects on isothermal allotriomorphic ferrite formation in 0.37C-1.45Mn-0.11V microalloyed steel', *Materials Transactions*, 2003, **6**, 1087–1095.

64. J. H. Jang, Y. U. Heo, C. H. Lee, H. K. D. H. Bhadeshia, and D. W. Suh: 'Interphase precipitation in Ti-Nb and Ti-Nb-Mo bearing stee', *Materials Science and Technology*, 2013, **29**, 309–313.

65. H. K. D. H. Bhadeshia: 'The first bulk nanostructured metal', *Science and Technology of Advanced Materials*, 2013, **14**, 014202.

66. P. R. Wilyman, and R. W. K. Honeycombe: 'Relation between $\gamma - \alpha$ transformation kinetics and mechanical properties of vanadium steels', *Metal Science*, 1982, **16**, 295–303.

67. T. I. Ramjaun, S. W. Ooi, R. Morana, and H. K. D. H. Bhadeshia: 'Designing steel to resist hydrogen embrittlement: Part 1 - trapping capacity', *Materials Science and Technology*, 2018, **34**, 1737–1746.

68. ISO 6507-1:2018: 'Metallic materials - Vickers hardness test - part 1: test method': International standard, International Standards Organisation, Geneva, Switzerland, 2018.

69. L. Lutterotti: 'Materials analysis using diffraction': 2013: URL `http://www.ing.unitn.it/ maud/index.html`.

70. L. Lutterotti, S. Matthies, and H.-R. Wenk: 'Maud: a friendly java program for material analysis using diffraction', *IUCr: Newsletter of the CPD*, 1999, **21**(14-15).

71. L. B. McCusker, R. B. V. Dreele, D. E. Cox, D. Louer, and P. Scardi: 'Rietveld refinement guidelines', *Journal of Applied Crystallography*, 1999, **32**, 36–50.

72. L. Lutterotti, R. Vasin, and H.-R. Wenk: 'Rietveld texture analysis from synchrotron diffraction images. i. calibration and basic analysis', *Powder Diffraction*, 2014, **29**, 76–84.

73. H.-R. Wenk, L. Lutterotti, P. Kaercher, W. Kanitpanyacharoen, L. Miyagi, and R. Vasin: 'Rietveld texture analysis from synchrotron diffraction images. ii. complex multiphase materials and diamond anvil cell experiments', *Powder Diffraction*, 2014, **3**, 220–232.

74. N. Gope, A. Chatterjee, T. Mukherjee, and D. S. Sarma: 'Influence of long-term aging and superimposed creep stress on the microstructure of 2.25Cr-1Mo steel', *Metallurgical Transactions A*, 1993, **24A**, 315–326.

75. H. K. D. H. Bhadeshia: Theory of Transformations in Steels: London, U.K.: CRC Press, Taylor and Francis Group, 2021.

76. S. Depinoy: 'Microstructural evolution of a 2.25Cr-1Mo steel during austenitization and temper: austenite grain growth, carbide precipitation sequence and

effects on mechanical properties': Ph.D. thesis, Ecole Nationale Supérieure des Mines de Paris, 2015.

77. 'Co-Cr-Mo alloy; M23C6 (Cr7MoCo15C6) crystal structure: Datasheet from "PAULING FILE Multinaries edition – 2012" in SpringerMaterials (https://materials.springer.com/isp/crystallographic/docs/sd_1928254)': 2016: Accessed 2019-08-28.

78. D. R. G. Mitchell, and C. J. Ball: 'Quantitative X-ray diffraction and analytical electron microscopy study of service-exposed 2.25Cr1Mo steels', *Materials Characterization*, 2001, **47**, 17–26.

79. J. Pilling, and N. Ridley: 'Tempering of 2.25Cr1Mo low carbon steels', *Metallurgical Transactions A*, 1982, **13**, 557–563.

80. R. G. Baker, and J. Nutting: 'The tempering of Cr Mo steel after quenching and normalising', *Journal of the Iron and Steel Institute*, 1959, **192**, 257–268.

81. R. C. Thomson, and H. K. D. H. Bhadeshia: 'Changes in chemical composition of carbides in 2.25Cr-1Mo power plant steel: part 1', *Materials Science and Technology*, 1994, **10**, 193–204.

82. F. Z. Kayser: 'A re-examination of Westbrooks's X-ray diffraction pattern for C_7C_3', *Materials Research Bulletin*, 1996, **31**, 635–638.

83. H. J. Chang, and J. J. Kai: 'The effects of thermal treatment on the microstrcuture and tensile properties of 2.25Cr-1Mo steel', *Scripta Metallurgica et Materialia*, 1990, **24**, 2101–2106.

84. 'Cr7c3 crystal structure: Datasheet from "pauling file multinaries edition – 2012" in springermaterials (https://materials.springer.com/isp/crystallographic/docs/sd_0313352)': 2016: Accessed 2021-07-19.

85. K. J. K. owski, and W. Zieliński: '$Mo_2C \rightarrow M_6C$ carbide transformation in low alloy Cr-Mo ferritic steels.', *Metal Science*, 1984, **18**, 223–224.

86. E. Parthé: 'The structure of dimolybdenum carbide by neutron diffraction technique', *Acta Crystallographica*, 1963, **16**, 202–205.

87. 'V4c3 (vc) crystal structure: Datasheet from "pauling file multinaries edition – 2012" in springermaterials (https://materials.springer.com/isp/crystallographic/docs/sd_1129205)': 2016: Accessed 2021-07-20.

88. T. Epicier, D. Acevedo, and M. Perez: 'Crystallographic structure of vanadium carbide precipitates in a model Fe-C-V steel', *Philosophical Magazine*, 2008, **88**, 31–45.

89. H. K. D. H. Bhadeshia: 'Prevention of hydrogen embrittlement in steels', *ISIJ International*, 2016, **56**, 24–36.

90. J. Nutting: 'The structural stability of low alloy steels for power generation applications', In: R. Viswanathan, and J. Nutting, eds. *Advanced Heat Resistant Steels for Power Generation*. London, U.K.: Institute of Materials, 1998:12–30.

91. B. Sundman, B. Jansson, and J. O. Andersson: 'The Thermo-Calc databank system', *CALPHAD*, 1985, **9**, 153–190.

92. H. K. D. H. Bhadeshia: Bainite in Steels: Theory and Practice: 3rd ed., Leeds, U.K.: Maney Publishing, 2015.

93. F. Huang, J. Liu, Z. J. Deng, J. H. Cheng, Z. H. Lu, and X. G. Li: 'Effect of microstructure and inclusions on hydrogen induced cracking susceptibility and hydrogen trapping efficiency of X120 pipeline steel', *Materials Science & Engineering A*, 2010, **527**, 6997–7001.

94. M. Garet, A. M. Brass, C. Haut, and F. Gutierrez-Solana: 'Hydrogen trapping on non metallic inclusions in Cr-Mo low alloy steels', *Corrosion Science*, 1998, **40**, 1073–1086.

95. H. B. Xue, and Y. F. Cheng: 'Characterization of inclusions of X80 pipeline steel and its correlation with hydrogen-induced cracking', *Corrosion Science*, 2011, **53**, 1201–1208.

96. C. Escrivà-Cerdàn, S. W. Ooi, G. R. Joshi, R. Morana, and H. K. D. H. Bhadeshia: 'Effect of tempering heat treatment on the CO_2 corrosion resistance of quench-hardened Cr-Mo low-alloy steels for oil and gas applications', *Corrosion Science*, 2019, **154**, 36–48.

97. J. Cong, J. Li, J. Fan, P. Liu, R. D. K. Misra, C. Shang, and X. Wang: 'The impact of interphase precipitation on the mechanical behavior of fire-resistant steels at an elevated temperature', *Materials*, 2020, **13**.

98. G. Miyamoto, R. Hori, B. Poorganji, and T. Furuhara: 'Interphase precipitation of VC and resultant hardening in V-added medium carbon steels', *ISIJ International*, 2011, **51**, 1733–1739.

99. S. W. Ooi, T. I. Ramjaun, C. Hulme-Smith, R. Morana, M. Drakopoulos, and H. K. D. H. Bhadeshia: 'Designing steel to resist hydrogen embrittlement: Part 2 - precipitate characterisation', *Materials Science and Technology*, 2018, **34**, 1747–1758.

100. S. Zhang, A. F. Gross, S. L. van Atta, M. Lopez, P. Liu, C. C. Ahn, J. J. Vajo, and C. M. Jensen: 'The synthesis and hydrogen storage properties of a mgh_2 incorporated carbon aerogel scaffold', *Nanotechnology*, 2009, **20**.

101. M. Ristic, M. Ivanda, S. Popovic, and S. Music: 'Dependence of nanocrystalline sno_2 particle size on synthesis route', *Journal of Non-crystalline Solids*, 2002, **303**, 270–280.